THE UNIVERSITY OF CHICAGO

DIRECT DARK MATTER DETECTION WITH THE DAMIC EXPERIMENT AT SNOLAB

A DISSERTATION SUBMITTED TO

THE FACULTY OF THE DIVISION OF THE PHYSICAL SCIENCES

IN CANDIDACY FOR THE DEGREE OF

DOCTOR OF PHILOSOPHY

DEPARTMENT OF PHYSICS

BY

JING ZHOU

CHICAGO, ILLINOIS

DECEMBER 2015

To Zimu

TABLE OF CONTENTS

ABSTRACT

There is strong cosmological and astrophysical evidence for the existence of non-baryonic, cold dark matter as a major constituent of the Universe. Its nature, so far elusive, constitutes one of the most fundamental questions in science. The existence of weakly-interacting massive particles (WIMPs) is a compelling explanation for dark matter, and a large experimental effort is ongoing to detect the rare interactions of WIMPs with dedicated detectors located underground to minimize backgrounds.

DAMIC (Dark Matter in CCDs) is a novel experiment with unique sensitivity to dark matter particles of masses below 10 GeV/c^2. It employs the bulk silicon of scientific-grade charge-coupled devices (CCDs) as the target for coherent WIMP-nucleus elastic scattering; the CCD is then used to detect the ionization produced by the recoiling nucleus. These devices, which are widely used for light imaging in astronomical telescopes and for X-ray detection in a variety of applications, are used in DAMIC for the first time as dark matter detectors. DAMIC CCDs are fabricated from n-type, high-resistivity silicon wafers, and are fully depleted (*i.e.* fully sensitive) over a record thickness of 675 μm. With 16 million pixels per CCD arranged over an area of 6 cm $\times$ 6 cm, these detectors provide a uniquely detailed spatial reconstruction of the energy deposited by a particle interaction. Also, the extremely low noise of the CCD readout results in an unprecedentedly low energy threshold to ionization of a few tens of eV. DAMIC was installed at SNOLAB - a laboratory located 2 km underground in a mine in Sudbury, Canada - at the end of 2012, and is now completing the R&D phase required for the construction of a 100 g detector, DAMIC100.

The work presented in this thesis covers the progress of the DAMIC experiment during its R&D phase. A significant contribution has been the development of data analysis and simulations tools, and their use in the characterization of DAMIC CCDs, including the measurement of charge diffusion and the response to electron-induced ionization.

A major contribution of this thesis is the measurement of radioactive contaminants potentially present in the apparatus. Photons, α and β particles - *e.g.* from isotopes of the uranium and thorium chains - can produce interactions in the CCD ultimately limiting the sensitivity of the experiment to dark matter searches. In addition to a careful screening of

all materials located close to the CCDs, we have performed measurements of radioactive contaminants in the CCD itself. For this purpose we have exploited the unique spatial resolution of the detector, which allows for accurate identification of α and β particles. Uranium and thorium contamination in the CCD bulk was measured through α spectroscopy, with an upper limit on the ^{238}U (^{232}Th) decay rate of 5 (15) kg^{-1} d^{-1} at 95% CL. We also searched for pairs of spatially correlated electron tracks separated in time by up to tens of days, as expected from ^{32}Si $-^{32}$P or ^{210}Pb $-$ ^{210}Bi sequences of β decays. ^{32}Si is a cosmogenic isotope which may be present in any silicon detector and constitute an irreducible background. The decay rate of ^{32}Si was found to be 80^{+110}_{-65} kg^{-1} d^{-1} (95% CI). An upper limit of ~ 35 kg^{-1} d^{-1} on the ^{210}Pb decay rate was obtained independently by α spectroscopy and the β decay sequence search. These levels of radioactive contamination are sufficiently low for the successful operation of the forthcoming DAMIC100.

Another major result presented in this thesis is the measurement of the nuclear ionization efficiency in silicon, namely the ratio of the energy released in ionization by a recoiling nucleus to the nucleus kinetic energy. Since only a fraction of the kinetic energy is released in the form of ionization, the experimental determination of the nuclear ionization efficiency is required for any consistent interpretation of a search for dark matter particles. We have performed a measurement of the nuclear ionization efficiency by detecting nuclear recoils induced in a DAMIC CCD by a fairly monochromatic beam of neutrons from a ^{124}Sb-Be source. This is the first measurement in the literature for kinetic energies of the recoiling silicon nucleus below 3 keV. A notable result is that the measured nuclear ionization efficiency is consistently lower than the prediction of the Lindhard theory in silicon, which is used as a reference in the field.

ACKNOWLEDGEMENTS

I would like to express my special appreciation and thanks to my advisor Professor Paolo Privitera who has been a tremendous mentor for me. I would like to thank him for supporting and encouraging me in the past five years. His enthusiasm in physics kept me constantly engaged in my research. He is smart and patient, showing me a lot of wonderful ideas and explaining them to me in details. He is always ready to answer my questions and give me guidances. His personal generosity made my time at University of Chicago really enjoyable.

I also like to express my heartfelt gratitudes to my committee members: Professor Grandi, Luca, Professor Nagel, Sidney and Professor Wang, Lian Tao.

My appreciation also extends to Dr. Alvaro E. Chavarria, who is the postdoc in our group. We have been colleagues for three years and it is really a wonderful experience working with him. He is always friendly and offers constant help. I am also grateful for the help provided by Dr. Javier Tiffenberg and other collaborators in DAMIC.

I would also like to thank my parents for working their best to give me the education, the opportunities and freedoms to pursue my dreams and interests. Finally, I want to thank my dearest one, Zimu (A Bao), for his love and support.

LIST OF FIGURES

LIST OF TABLES

CHAPTER 1
INTRODUCTION

1.1 Dark Matter

Dark matter is a hypothetical kind of matter that cannot be seen with telescopes but accounts for most of the matter in the universe. According to the Planck mission team and based on the standard model of cosmology, the total mass and energy of the known universe contains 4.9% ordinary matter, 26.8% dark matter and 68.3% dark energy [5]. However, dark matter has not been detected directly, making it one of the greatest mysteries in modern astrophysics.

The first robust indications that the mass to light ratio was anything other than unity came from measurements of galaxy rotation curves which is a plot of the magnitude of the orbital velocities of visible stars or gas in that galaxy versus their radial distance from that galaxy's centre, shown in Figure 1.1 [6]. The dashed line is the predicted line with only visible stars or gas while the solid line is the observed line which could be explained by dark matter. Clouds of neutral hydrogen extend far beyond the galactic disk and thus allow the measurement of the orbital velocity much further out than the stars. From a measurement of the rotational velocity of stars and gas as a function of radius r one can compute the mass M(r) of the galaxy enclosed within that radius. In Newtonian mechanics, since $v(r) = pGM(r)/r$, one would expect that at a radius beyond the extent of the stellar disk the rotational velocity should go as $v(r) \propto r^{-1/2}$. Instead, rotation curves exhibit a flat behavior that extends far beyond the stellar disk. The expected contribution to the rotational velocity from the luminous mass (disk) and the interstellar gas (gas) by themselves cannot explain the observed rotation curve but the assumption of the presence of a dark halo with $M(r) \propto r$ can account for the observed behavior.

The most precise measurements of the abundance of dark matter in our universe and stringent constraints on its baryonic content come from measurements of the cosmic microwave background (CMB). Much has happened since the accidental discovery [7] of the predicted left over radiation from the Big Bang. We now know that it follows with extreme

precision the black body spectrum at a temperature of 2.725 K, and that anisotropies are at the level of 10 μK. The angular power spectrum of the CMB depends on parameters like the physical baryon density, the physical cold dark matter density, and the dark energy density. The measurement of the temperature anisotropies thus provides constraints on the three cosmological parameters.

There are also other astronomical observations that show the existence of dark matter [8]. Determining the nature of the dark matter is one of the most important problems in modern

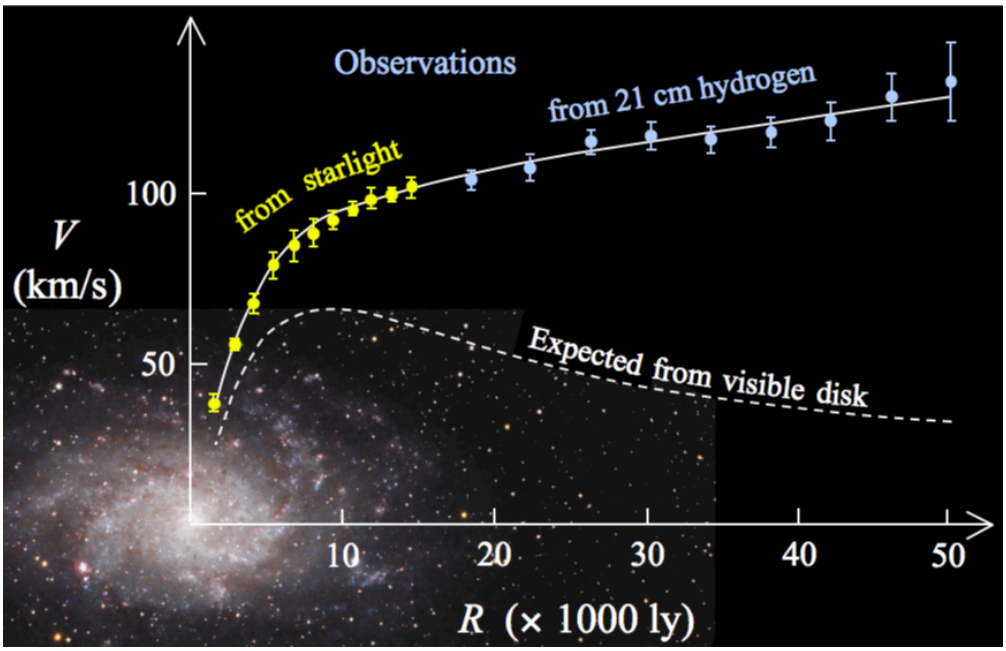

Figure 1.1: Galaxy rotation curve. The dashed line is the predicted line with only visible stars or gas while the solid line is the observed line which could be explained by dark matter.

cosmology and particle physics. From the astronomical observations, we know dark matter cannot consist of baryons or of light particles unless they are created via a phase transition in the early universe. Here are the most famous candidates:

Weakly-interacting massive particles (WIMPs):

WIMPs are among the leading hypothetical particle physics candidates for dark matter, which could resolve a number of astrophysical and cosmological problems related to dark matter. The WIMP fits the model of a relic dark matter particle from the early Universe, when all particles were in a state of thermal equilibrium. For sufficiently high temperatures, the dark matter particle and its antiparticle would have been both forming from and annihilating into lighter particles. As the Universe expanded and cooled, the average thermal

energy of these lighter particles decreased and eventually became insufficient to form a dark matter particle-antiparticle pair. The annihilation of the dark matter particle-antiparticle pairs, however, would have continued, and the number density of dark matter particles would have begun to decrease exponentially. Eventually, the number density would become so low that the dark matter particle and antiparticle interaction would cease, and the number of dark matter particles would reach a rough constant as the Universe continued to expand. Particles with a larger interaction cross section would continue to annihilate for a longer period of time, and thus would have a smaller number density when the annihilation interaction ceases. Based on the current estimated abundance of dark matter in the Universe, if the dark matter particle is such a relic particle, the interaction cross section of the particle-antiparticle annihilation can be no larger than the cross section for the weak interaction, which is so called "WIMP miracle". [9]

Axions:

The axion is a hypothetical elementary particle postulated by the Peccei Quinn theory in 1977 to resolve the strong CP problem in quantum chromodynamics (QCD). One theory of axions relevant to cosmology has predicted that they would have no electric charge, a very small mass in the range from 10^6 to 1 eV/c^2, and very low interaction cross sections for strong and weak forces. If axions have low mass, thus preventing other decay modes, theories predict that the universe would be filled with a very cold Bose Einstein condensate of primordial axions. Hence, axions could plausibly explain the dark matter problem of physical cosmology. [9], [10]

There are also other popular candidates like gravitinos, sterile neutrinos and so on.

1.2 Detection of Dark Matter

There are numerous experiments aiming to verify the existence of dark matter, which could be divided into three categories: A. direction detection; B. indirect detection; C.accelerator search. Indirect detection experiments search the dark matter annihilation or decay products. Now we only focus on the direct detection of dark matter.

1.2.1 WIMP-Nucleus Interactions

The dominant interaction mechanism between WIMPs and nuclei is the elastic scattering due to the spin-independent interaction. The differential recoil energy spectrum between a

WIMP with mass m_X and a target nucleus of mass m_T is given by :

$$\frac{dR}{dE_R} = \frac{\sigma_0 \rho_0}{\sqrt{\pi} v_0 m_X m_r^2} F^2(E) T(E) \tag{1.1}$$

where ρ_0 is the WIMP density in the local neighborhood within the galactic halo, σ_0 is the elastic scattering cross-section between the WIMPs and nuclei, m_r is the WIMP-nuclei reduced mass: $m_r = m_x m_T/(m_x + m_T)$, F(E) is the nuclear form factor, and T(E) is a dimensionless integral over the local WIMP velocity distribution $f(v_D)$:

$$f(v_D) = \frac{\pi k v_0^2 v}{v_E} = \begin{cases} exp(-\frac{(v_D - v_E)^2}{v_0^2}) - exp(-\frac{(v_D + v_E)^2}{v_0^2});\ V_D <= v_{esc} - v_E \\ exp(-\frac{(v_D - v_E)^2}{v_0^2}) - exp(-\frac{v_{esc}^2}{v_0^2});\ v_{esc} - v_E < V_D <= v_{esc} + v_E \\ 0; V_D > v_{esc} + v_E \end{cases} \tag{1.2}$$

Here, v_D is the WIMP velocity, v_{esc} is the escape velocity and v_E is the Earth velocity. Figure 1.2 shows the local WIMP velocity distribution when $v_0 = 230$ km/s, $v_E = 244$ km/s, and $v_{esc} = 600$ km/s. For spin-independent scattering, σ_0 is approximately proportional to the WIMP-proton scattering cross-section σ_{x-p} which is $\sigma_0 \sim A^2 \sigma_{x-p}$. Figure 1.3 is the

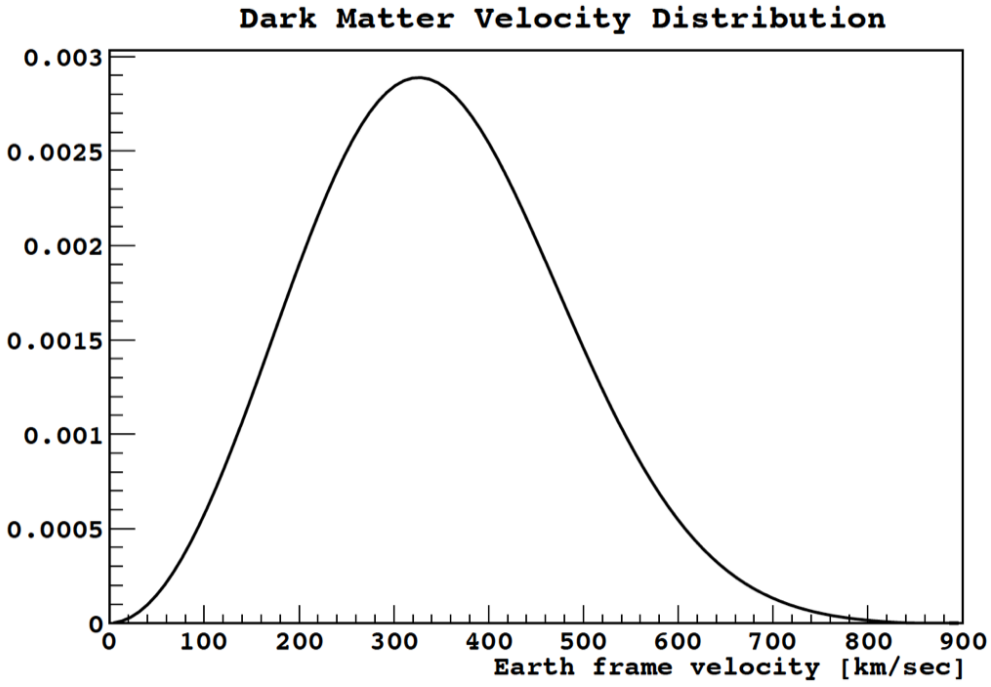

Figure 1.2: The local WIMP velocity distribution with $v_0 = 230$ km/s, $v_E = 244$ km/s, and $v_{esc} = 600$ km/s.

differential recoil spectra with a WIMP mass of 100 GeV/c^2 and spin-independent cross-section ($\sigma_{x-p} = 10^{-45} cm^2$) with various target nuclei. Many experiments use a readout channel into which only a fraction of the recoil energy is deposited. In such a scenario, the measured energy has to be converted to the true recoil energy through an energy-dependent factor called the quenching parameter (in DAMIC, it is called ionization efficiency which will be discussed in Chapter 5.) The measured energy is often labeled in units of keV$_{\rm ee}$ (keV electron equivalent) while the nuclear recoil energy is often labeled with units of keV, keVr, or keV$_{nr}$. [11]

1.2.2 Summary of direct dark matter detection experiments

From the properties of WIMPs and the expected interaction rates with the normal matter it is possible to identify the characteristics required of an instrument aiming at the detection of the scattering of WIMPs in its target volume. The detector should have a low threshold for the detection of nuclear recoils, as the expected exponential spectrum of recoil energies translates into a large sensitivity increase with reduced thresholds. Given the extremely low interaction rates, the detector should have a very low radioactive background, especially at low energies. If the detector is capable of discriminating between nuclear recoils and electronic recoils this will constitute a clear advantage since the most predominant background, electronic recoils from γ rays and β decays, will be rejected. Fast neutrons, which can produce low energy nuclear recoils, are then the ultimate background remaining. If the detector can measure an expected feature of WIMP interactions with normal matter, such as the annual modulation of the rate, the anisotropy of the nuclear recoil directions, or the rate dependence on the target material, then this will also constitute a clearer signature.

Currently, the direct dark matter detection experiments could be divided into four categories based on the detection techniques.

A. Scintillation

These detection experiments use scintillators as target materials in a low radioactivity enclosure and read out with photomultiplier tubes to detect particle interactions. The most widely used scintillators are NaI (Tl), Xe, Ar, Ne and CF_4. DAMA/LIBRA [12], DEAP [13] and CLEAN are experiments using scintillators.

B. Ionization Detectors

Those experiments use Ge or Si as target materials. When particles (WIMP) hit the

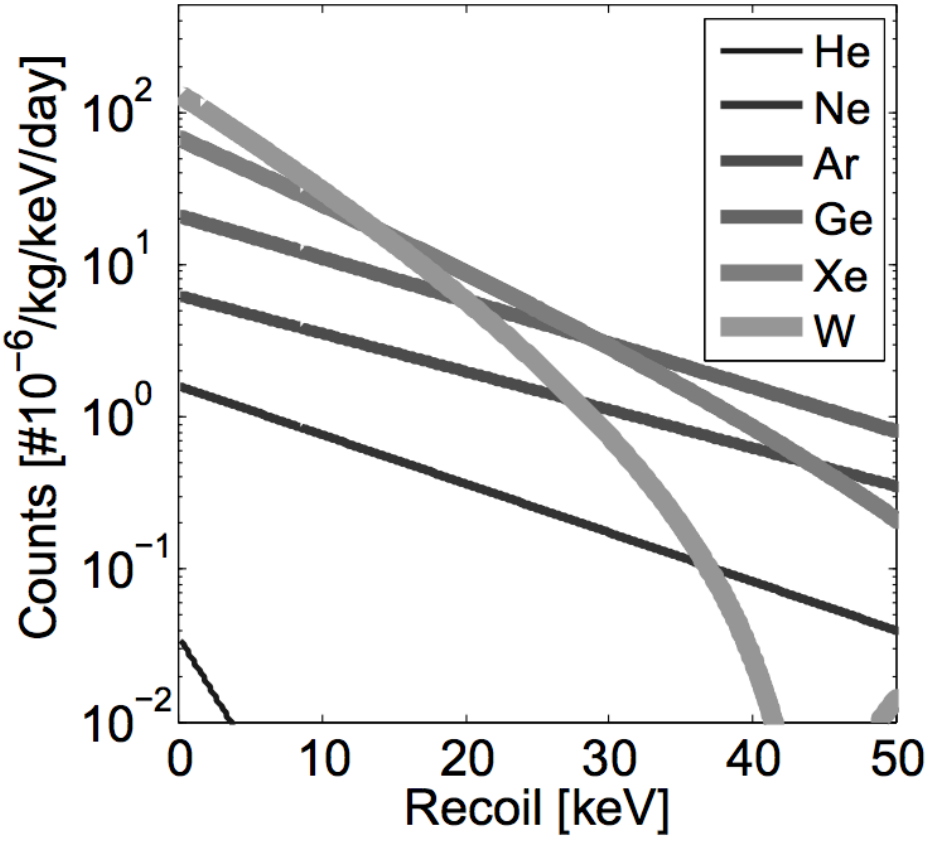

Figure 1.3: The differential recoil spectra with WIMP mass of 100 GeV/c^2 and spin-independent cross-section ($\sigma_{x-p} = 10^{-45} cm^2$) with various target nuclei.

target, it will scatter with the target nuclei. The deposited energy could ionize the electrons (holes) with some efficiency that could be readout. CoGent, CDMS [14] and DAMIC belongs to this category.

C. Time Projection Chambers (TPC)

Xenon and argon two-phase TPC have also be developed for dark matter detection. A low radioactivity vessel is partially filled with liquid xenon (argon) while the rest is filled with xenon (argon) gas. By applying a bias voltage across the liquid and gas volumes, an electric field of ∼1 keV/cm and ∼10 keV/cm are created. Photomultiplier tube arrays are installed on the top and bottom of the chamber to detect scintillation photons form the interaction. Figure 1.4 shows the schematic of a TPC used in dark matter detection. An initial signal (S1) is coming from the scintillation produced at the interaction time. Ionized electrons created by the interaction drift in the electric field and accelerate in the gas, producing a second scintillation signal (S2). LUX and Xenon are the leading experiments in this category. [15], [16]

D. Superheated Liquids

COUPP experiment makes use of a bubble chamber detector containing superheated liquid (CF_3I) as the target material. An energy deposition in the liquid from a particle interaction creates a local nucleation of a bubble. The pressure spike due to the bubble formation triggers a video camera to record the event, which allows a 3D position reconstruction of the interaction. [17]

1.2.3 Current situation of direct dark matter detection

The current status of direct dark matter searches in the low mass region is summarized in Figure 1.5. The figure shows that there is a set of experiments that have produced limits that are probing into the high mass region preferred by supersymmetric models that quickly lose sensitivity as the dark matter particle mass is reduced. At the same time there are claims of experimental results consistent with the observation of a dark matter signal. There is significant tension between these results, because the region of positive signals is rejected to high confidence level by some experiments. In particular, the XENON-100 experiment claims rejection to 90% C.L [2], of all the experimental hints for dark matter. There has been extended discussion about these results in the literature, including speculation of possible systematic effects that could influence the different experimental results [1],[2],[3],[4]. In

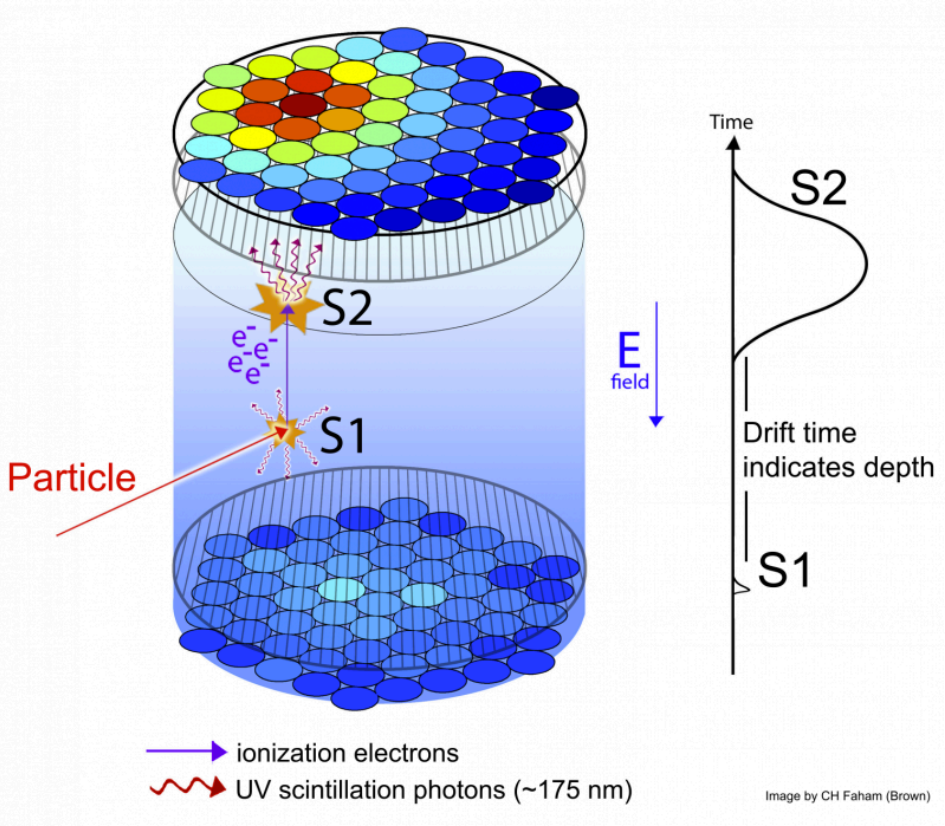

Figure 1.4: Schematic of a xenon two-phase time-projection chamber, showing the recorded signals for a gamma interaction and a WIMP. The ratio S2/S1 is used to discriminate between electron and nuclear recoils.

summary, for more than 10 years the dark meter community has been puzzled by a possible detection of a low mass dark matter particle by DAMA/NaI and DAMA/LIBRA that could not be confirmed experimentally. Since the supposed signal was detected using lower energy thresholds than was used in the the other experiments which excluded their results, their signal has not been completely ruled out as Dark Matter. In the past two years there have been three new experimental hints for the low mass dark matter signal as shown in Figure 1.5.

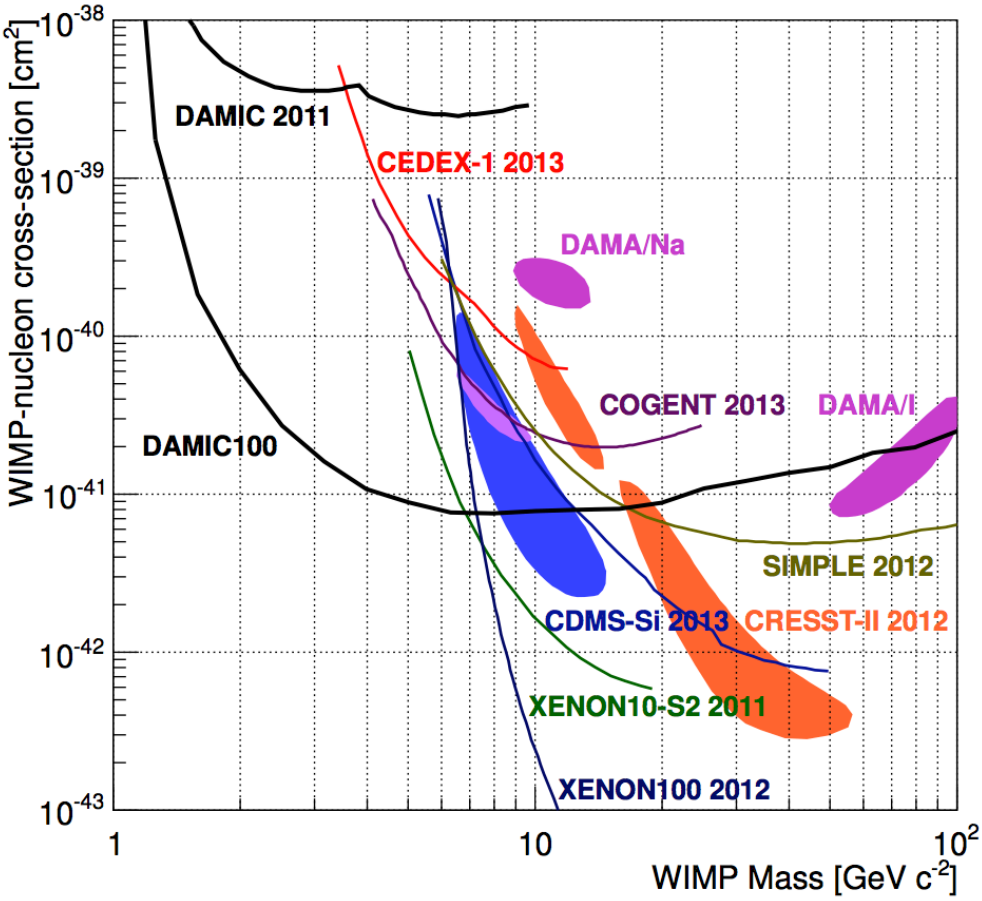

Figure 1.5: Current 90% C.L. exclusion limits and regions consistent with observed excess of events for spin independent dark matter searches by several Collaborations [1],[2],[3],[4]. Also shown is the expected sensitivity range for the proposed DAMIC100 after 1 year of data taking.

CHAPTER 2
THE DAMIC EXPERIMENT

The DAMIC (Dark Matter in CCDs) experiment uses the bulk silicon of a scientific-grade charge-coupled device (CCD) as the target for coherent WIMP-nucleus elastic scattering. The relatively low mass of the silicon nucleus, as well as the low read-out noise of the detector, make the CCD an ideal instrument for the identification of the nuclear recoils with keV-scale energies from WIMPs with masses <10 GeV/c^2. Historically, CCDs had not been considered as a viable WIMP detector due to their relatively low mass (<1 g per detector). Yet, recent advances in CCD technology, mostly due to the increase in the purity of the silicon, allow for the fabrication of fully-depleted CCDs with exceptionally low levels of radioactive contamination and several g of mass. These instruments have been successfully characterized and deployed in astronomical telescopes, where their large area and thickness allow for the efficient detection of near-infrared light. With DAMIC, they are used for the first time to search for Dark Matter particles.

2.1 Charge Coupled Devices

The charge-coupled device was invented in 1969 at AT&T Bell Labs [18], initially motivated by the development of memory storage. Very soon it was realized that CCDs could be used for light imaging purposes, which has been indeed the largest application of these devices. The cross section of a CCD pixel is shown in Figure 2.1. The bulk of the device is made of doped silicon (n-type in this case), where an incoming photon of energy E_γ greater than the band-gap energy of the semiconductor (1.1 eV) can produce electron-hole (e-h) pairs. Photons of energies up to 3.1 eV can only generate a single (e-h) pair, with a probability which increases with the photon energy. For $E_\gamma > 10$ eV, the number of (e-h) produced is E_γ/E_{e-h}, where E_{e-h}=3.65 eV is the average energy required to generate an (e-h) pair in silicon[18]. Each CCD pixel is essentially a metal-oxide-semiconductor(MOS) capacitor, where the charge produced by the incident photon is stored. A bias voltage is applied across the device, which drifts the electrons towards the backplane of the CCD and the holes towards

the gates (metal electrodes) of the CCD pixel. While drifting, the charge diffuses and may extend over several pixels in the x-y plane. The holes are then kept in the potential well at the "buried" p-channel - a p-doped silicon layer typically 1-2 μm thick just below the oxide layer; the potential well produced by this channel maintains the charges away from the oxide-semiconductor interface where they can get trapped. Charge produced by incoming light keeps accumulating at the pixels during the CCD exposure. By appropriate changes in the gates potential, the charge can be moved from pixel to pixel up to a readout stage. Figure 2.3 schematically illustrates the readout process. In the three-phase CCD, each pixel (also called register) is defined by three gates (P_1, P_2, P_3) which are appropriately set to high and low states to hold the charge in place. Vertical registers are separated by potential barriers called channel stops (grey bands in Figure 2.3) which prevent the spread of the charge between adjacent columns. The gate P_i of every vertical register in a CCD column is connected to the same clock driver, and an appropriate clock sequence of the gates results in the sequential movement of the charge in the vertical direction. For each vertical clock sequence, a line of vertical pixels is transferred into an horizontal register (serial register), where an horizontal three-phase clocking moves the charge horizontally to an output charge-to-voltage amplifier for readout. Thus, the CCD is serially readout. For scientific grade CCDs, the inefficiency of charge transfer from pixel to pixel is as low as 10^{-7}, which introduces a negligible loss of charge since the number of transfers required for readout is at most 8,000 (for a large format CCD of 4k$\times$4k pixels).

The design of the amplifier is crucial for low-noise operation of the device. An example of readout node is shown in Figure 2.2. This kind of design provides powerful noise reduction through the Correlated Double Sampling (CDS) technique. A significant component of the noise is introduced by the reset pulse required to eliminate the pixel charge after readout. In the CDS, the pixel voltage is measured a first time just after the reset pulse, and a second time after the charge has been moved into the pixel. When making the difference between these two voltage levels, the reset noise is canceled. With appropriate optimization of the integration time windows for the charge measurement, readout noise levels of a few electrons can be achieved. Another potential source of noise comes from the dark current of the device: charge from thermally generated electron-holes will be collected in the CCD during an exposure even in the absence of light, and the statistical fluctuation of this charge will result in noise. The dark current noise can be significantly reduced, usually to a negligible level with respect to the readout noise, by operating the CCD at cryogenic temperatures

($\sim$ 100 K).

CCDs are also sensitive to ionizing radiation, and they have been used as X-ray detectors in a variety of applications [19]. The energy lost by ionizing radiation in semiconductor detectors ultimately results in the creation of electron-hole pairs, and the average energy necessary to create an electron-hole pair in silicon (3.65 eV) is found to be independent of the type and the energy of the ionizing radiation. The capability of the CCD to detect very low-energy deposits (tens of eV) from ionizing particles is the main reason for its use in DAMIC.

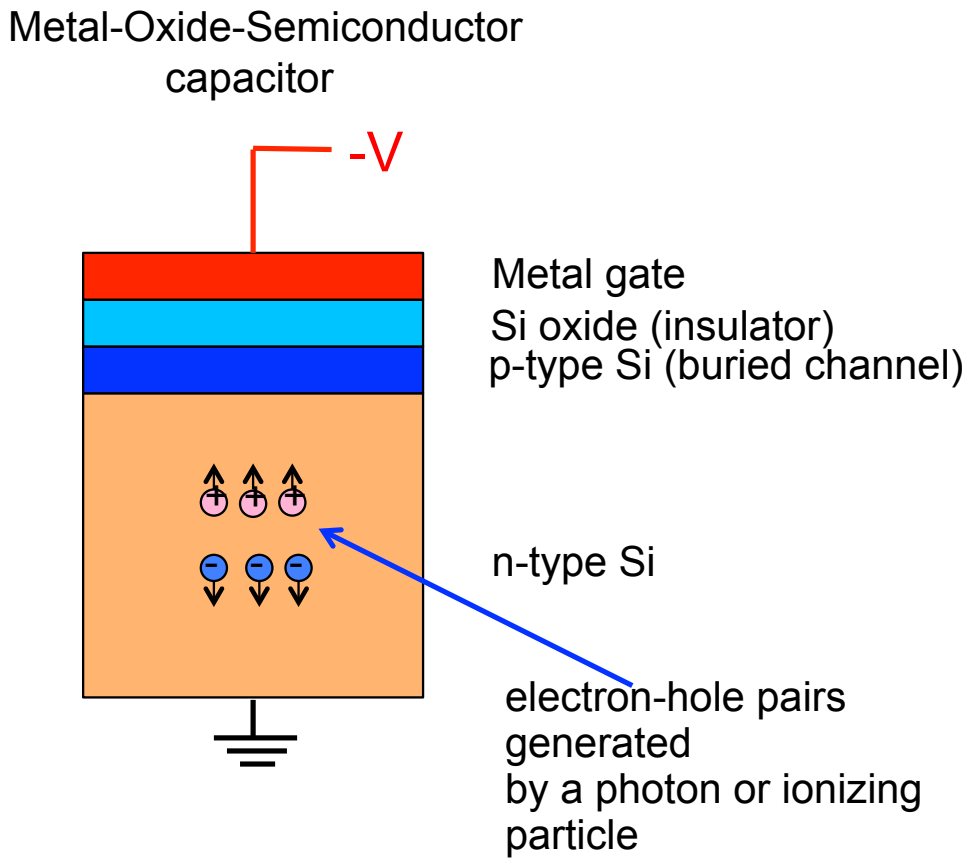

Figure 2.1: Sketch of a CCD pixel.

2.2 CCDs as Dark Matter detectors

The DAMIC experiment employs a novel type of CCD, developed originally at Lawrence Berkeley National Laboratory MicroSystems Lab [20] for detection of near-infrared light.

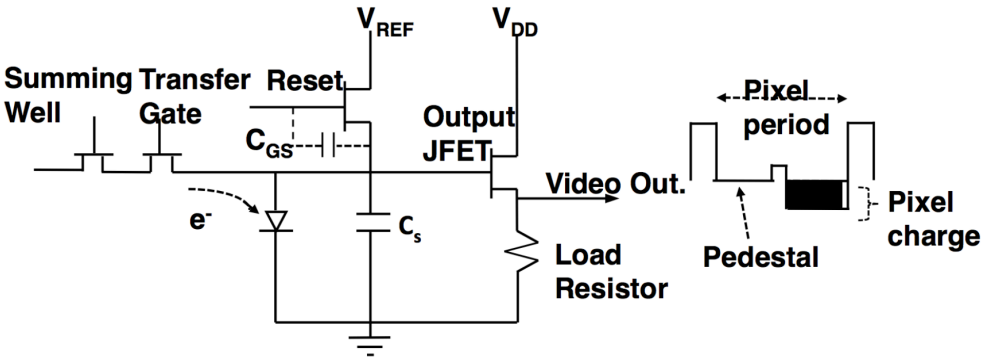

Figure 2.2: Schematic of a CCD readout node, with a sketch of the sequence of voltage levels used for the Correlated Double Sampling.

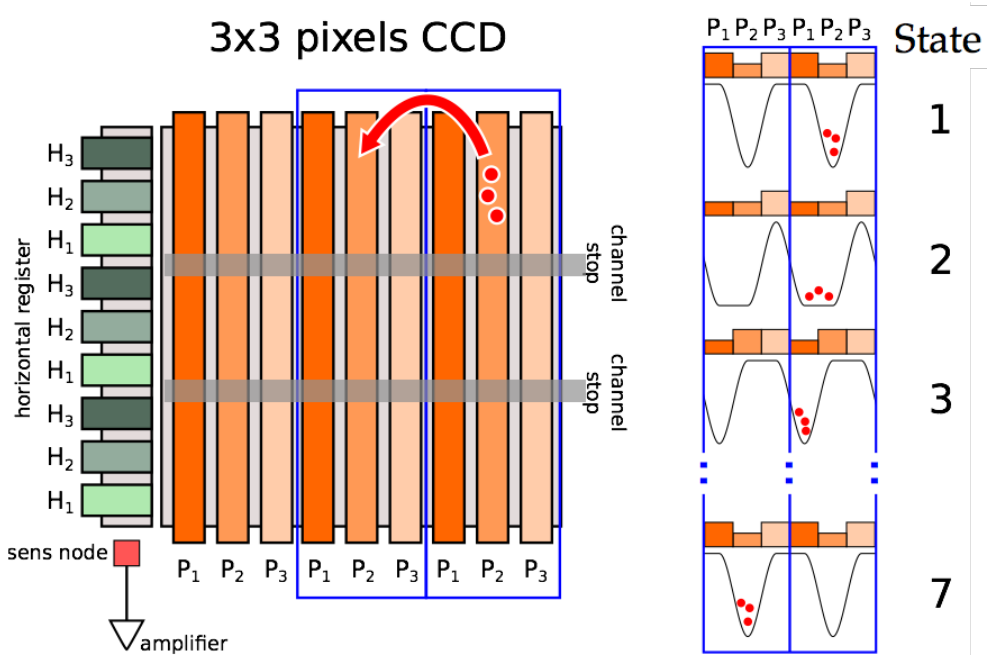

Figure 2.3: Illustration of the CCD readout process. Explanation in the text.

To achieve high quantum efficiency at these wavelengths, the detector must be significantly thicker than usual CCDs (hundreds instead of tens of μm) which requires the use of high-resistivity silicon (10$\sim$20 kΩ /cm). The high-resistivity of the silicon allows for a low donor density in the substrate ($\sim 10^{11}$ cm^3), which leads to fully depleted operation at reasonably low values of the applied bias voltage (up to 100 V). The possibility to fabricate large format CCDs of hundreds of μm thickness (with few g of mass) encouraged a dedicated R&D effort to explore their use for dark matter detection. The DAMIC R&D started with CCDs of 250 μm thickness originally developed for the Dark Energy Survey (DES) camera (DECAM)[21]. The current thickness of DAMIC CCDs is 675 μm. These CCDs are fabricated in 2k$\times$4k and 4k$\times$4k pixel format, with pixel size of 15 μm $\times$ 15 μm. One of the larger format CCDs (6 cm$\times$6 cm) with an active mass of 5.9 g is shown in Figure 2.4. DAMIC CCDs are operated at a temperature of 120-140 K, where the dark current is only ≈ 0.1 e$^-$pix^{-1}day^{-1}. The readout noise reaches a minimum value of ≈ 2 e$^-$ for a pixel readout time of ≈ 40 μs.

An image taken with a DAMIC CCD at ground level is shown in Figure 2.5, which illustrates the power of CCDs as a detectors of ionizing radiation. Low energy electrons (e.g. from X-rays) and nuclear recoils, whose physical track length in silicon is $<$15 μm, produce diffusion limited" clusters, where the spatial extension of the cluster is dominated by charge diffusion while drifting towards the gates. Higher energy electrons, from either Compton scattering of high energy gammas or beta decay, lead to extended tracks. Often clusters present a worm-like structure due to straggling of the electrons. Cosmic ray muons or high-energy (MeV) electrons pierce through the CCD, leaving a straight track. Alpha particles entering the CCD backside produce a dense column of electron-hole pairs which results in highly-diffuse round clusters of 100s of μm in diameter (4.7(a), see Section 4.4.1). These highly distinctive features allow for an accurate classification of the measured clusters, resulting in powerful particle identification. The principle of WIMP detection with a CCD is illustrated in Figure 2.6. A Si nucleus acquires keVnr of kinetic energy from the WIMP elastic scattering. The ionization charge produced by the nuclear recoil is drifted towards the pixels gates, where is held in place until the readout. Since the range of a Si ion is much smaller than the pixel dimension (e.g. 20 nm for 10 keVnr recoil), the resulting CCD signal is a diffusion-limited round cluster of pixels (Figure 2.5). The size of the cluster depends on the depth where the interaction occurred, i.e. on the distance the charge has diffused while drifting toward the pixel gate.

When compared to other WIMP detectors, DAMIC CCDs present some unique proper-

ties:

- Very low energy threshold: in DAMIC CCDs the noise is dominated by the readout, since at the operating temperature of 140 K the dark current contributes negligibly. We achieve routinely a readout noise of $\approx$ 2 e^- for the charge collected in a pixel. Since on average 3.65 eV are required to produce an electron-hole pair in silicon, the readout noise corresponds to an uncertainty of $\approx$7 eV in deposited energy. This allows for the positive identification (5 sigma) of as little as 35 eVee[1] of energy deposited in a pixel. For comparison, energy thresholds achieved so far by CoGeNT PPC and CDMSlite germanium detectors are 500 eVee [1] and 170 eVee [22], respectively. The lower energy threshold of a CCD extends the range of low mass WIMPs to be probed. Also, since the expected spectrum of WIMP-induced nuclear recoils is exponential, a lower energy threshold results in a higher WIMP rate. Thus, a CCD may be comparable in sensitivity to a larger mass detector of higher threshold.

- Exquisite spatial resolution, which makes diffusion-limited clusters readily recognizable as WIMP candidates (Figure 2.5). In addition, it enables surface backgrounds rejection based on the size of the event: a low energy background particle entering the CCD from the front surface close to the gates is detected as a one or two pixel cluster, while it presents the largest possible size when entering from the back surface. The particle identification capability of the CCD provides unique information to study and then mitigate the radioactive contamination in the detector. Finally, background events occurring in the CCD bulk - for example, from a ^{32}Si sequence of beta decays - can be rejected as spatially correlated events occurring at different times (Section 4.5).

2.3 The DAMIC setup at SNOLAB

The DAMIC experiment is installed at SNOLAB, an underground laboratory specialized in neutrino and dark matter physics. The laboratory is located 2 km below the surface in the Vale Creighton Mine - an active nickel mine - near Sudbury, Ontario, Canada. An overview of the DAMIC components is given in Figure 2.7. A packaged CCD is shown in Figure 2.7(a). The device is epoxied to a high-purity silicon support piece. The CCD clocks and readout

[1]The electron-equivalent unit eVee refers to energy deposited by an electron. In general, a recoiling nucleus will loose its kinetic energy through different mechanisms, with only part of it resulting in ionization.

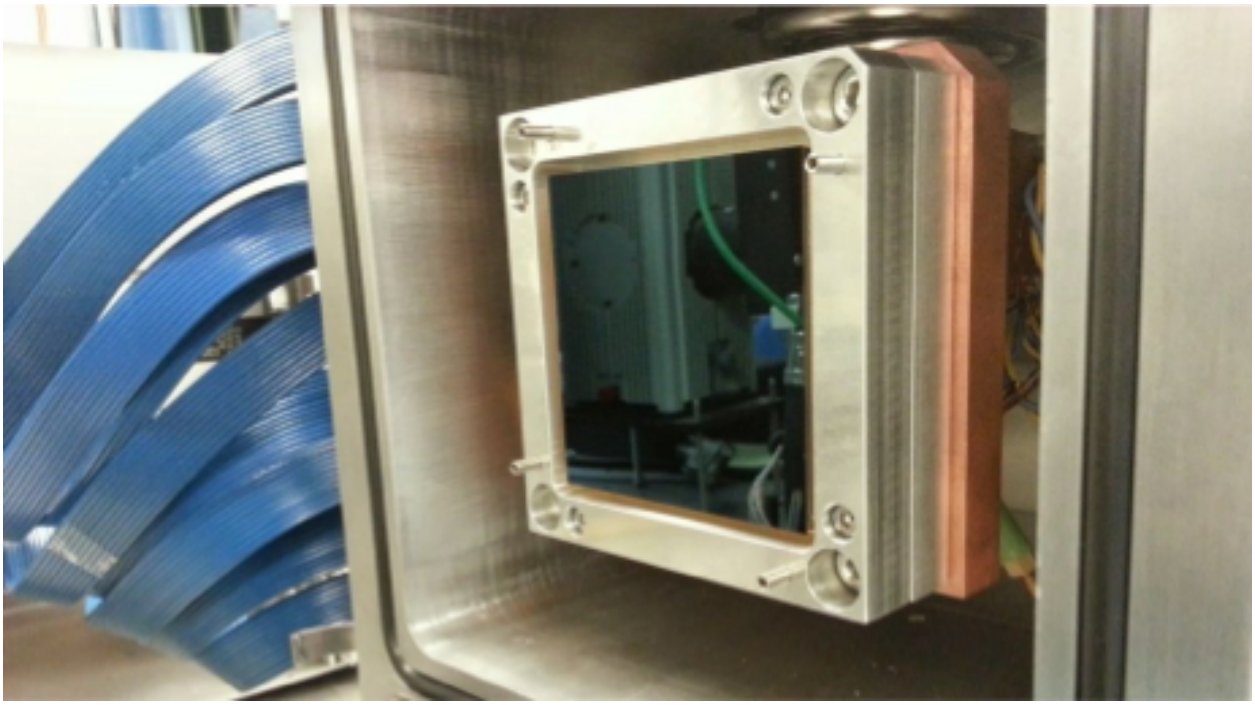

Figure 2.4: A DAMIC 4k×4k CCD of 675 μm thickness.

node signal travel on a Kapton cable, appropriately shaped for wire bonding. The cable is also glued to the silicon support. A copper bar facilitates the handling of the packaged CCD and its insertion into a slot of an electropolished copper box (Figure 2.7(b)). The box is located inside a copper vacuum vessel ($\sim 10^{-6}$ mbar) where is maintained at a temperature of $\sim$140 K by a cryogenic cold head. An 18 cm thick lead block hanging from the vessel flange shields the CCDs from radiation produced by the electronics card (Vacuum Interface Board, VIB), also located inside the vessel (Figure 2.7(c)). The CCDs are connected to the VIB through the Kapton flex cables, which run along the side of the lead block. The processed signals then proceed to the data acquisition crate. The vacuum vessel is inserted in a lead castle (Figure 2.7(d)) which shields the CCDs from ambient γ-rays through at least 21 cm of lead. The innermost inch of lead comes from an ancient Spanish galleon and has negligible ^{210}Pb content, strongly suppressing the background from bremsstrahlung γs produced by ^{210}Bi decays in the outer lead shield. A 42 cm thick polyethylene shielding is used to moderate and absorb environmental neutrons. A significant amount of radon gas is present in the SNOLAB experimental halls ($\sim$100 Bq/m^3), and photons from its decay chain can also contribute to the background. To reduce the amount of radon in proximity

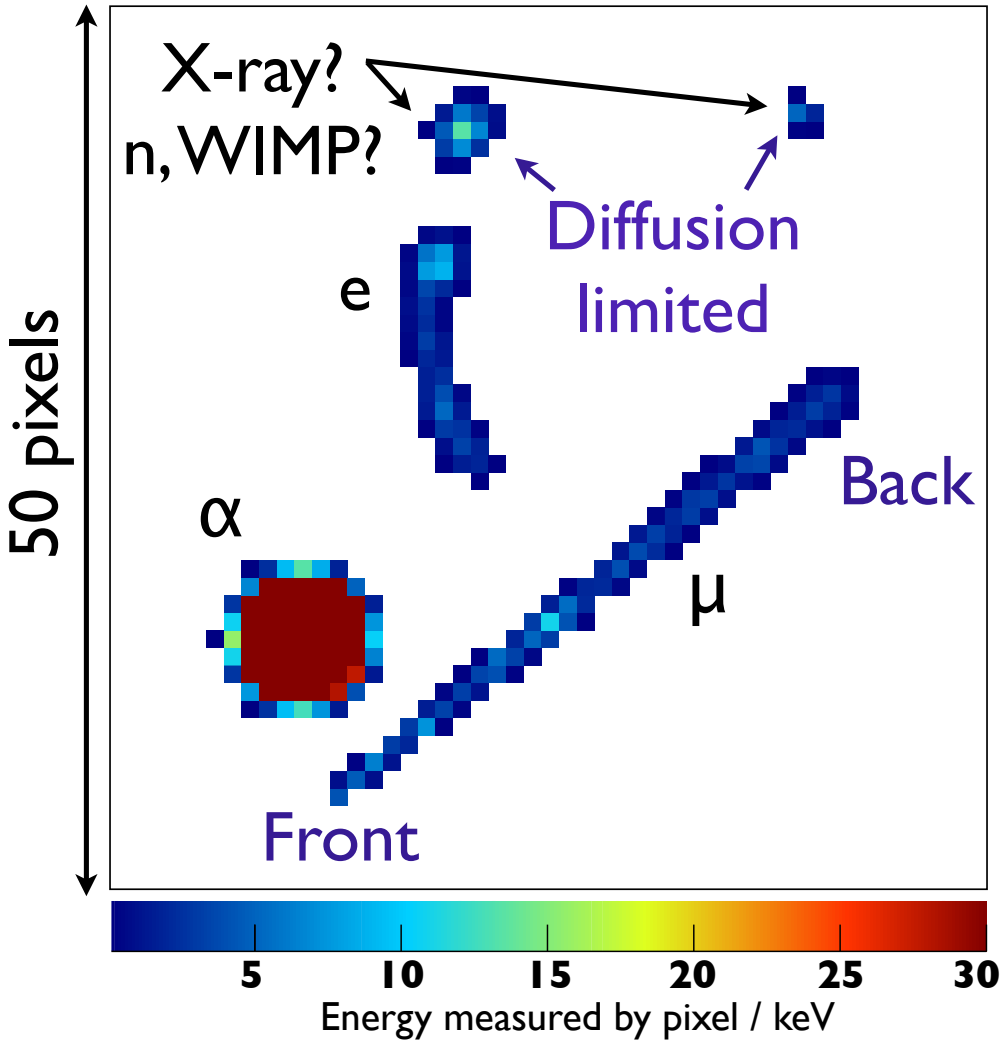

Figure 2.5: 50×50 pixel portion of a CCD image, taken when the detector was at ground level. Different kinds of particles are recognizable (see text). For better contrast, only pixels with deposited energy >0.1 keV are represented in color.

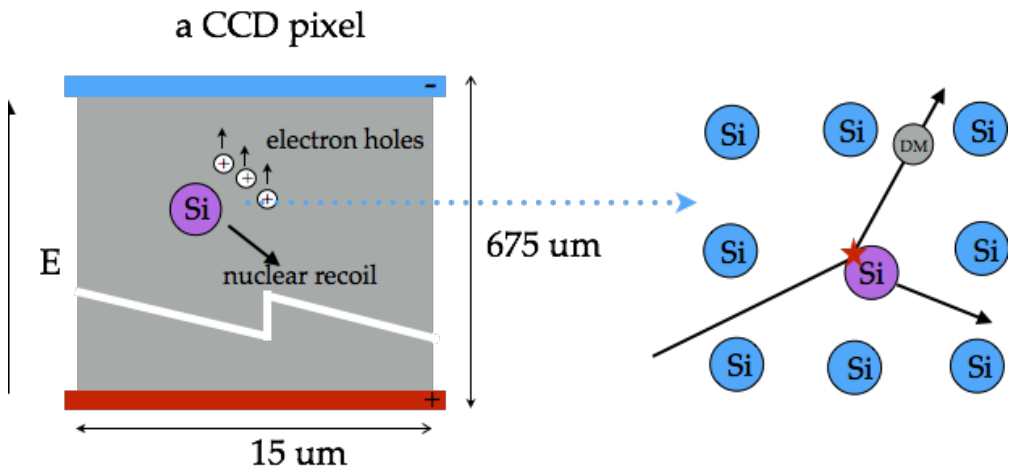

Figure 2.6: A cross-section of CCD pixel, with an illustration of the WIMP detection principle.

of the vessel, the entire shielding is enclosed in an aluminum box flushed continuously with pure nitrogen gas.

For the readout electronics, we have adopted the MONSOON [23] architecture developed for the DECam project. The MONSOON also provides the required voltage biases and clocks for the operation of the CCDs. A slow control system ensures a safe operation of the vacuum pump and cryogenic equipment. DAMIC operation and data taking is performed remotely. In stable data taking mode, DAMIC CCDs are exposed for about 8 hours before readout. The exposure time was chosen so that the dark current of the CCDs would still be negligible, while minimizing the number of images taken in a science run. The number of pixels with noise is also minimized, which reduces the chance of pixels with noise charge to pass a selection threshold (Section 3.1).

2.4 DAMIC R&D achievements

To validate the use of thick CCDs as WIMP detectors, an intense R&D program has been pursued by DAMIC. This program has focused on the improvement of the devices (thicker, low noise CCDs) as well as on the reduction of radioactive backgrounds.

The first test of CCDs in the DAMIC setup at SNOLAB occurred in November 2012 with six detectors coming from a CCD production for the DECam. These detectors were 250 μm thick and featured a package which is standard for CCDs used in astronomy: the

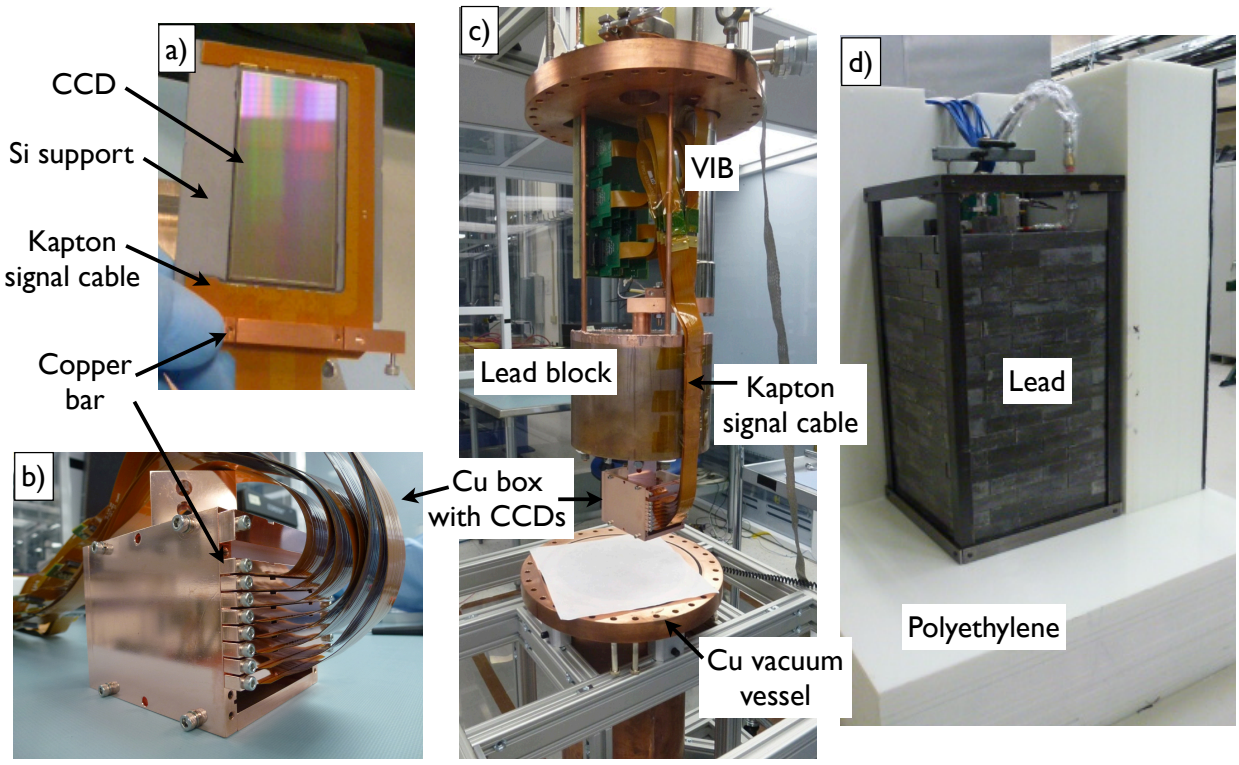

Figure 2.7: a) A packaged DAMIC CCD. b) The copper box housing the CCDs. c) Components of the DAMIC setup, ready to be inserted in the vacuum vessel. d) The vessel inside the lead castle, during installation of the polyethylene shield.

CCD is glued to an aluminum nitride (AIN) support as in Figure 2.8(a). The AIN is usually chosen because its thermal expansion coefficient is similar to that of silicon, which prevents damage of the CCD during the cooling process. This first installation demonstrated a stable performance of the detectors with low noise for several months. At the same time, it was evident that the standard packaging was producing a considerable background. The energy spectrum collected with AIN packaged CCDs is shown in Figures 2.9 and 2.10 (blue line), with prominent X-ray peaks around 10 keV. The background level at low energy was found to be around 10^4 events/(keV_{ee}·kg·d) . The energies of the X-rays were compatible with those from ^{238}U chains, with the most probable origin of the background being radioactive contamination of the AIN support. This hypothesis was verified by installing in June 2013 CCDs with a new AIN packaging where the central part of the AIN support was cut (Figure 2.8(b)), resulting in a smaller mass of AIN present close to the detector and also in a smaller solid angle for X-rays, β and gamma rays from ^{238}U and ^{232}Th to reach the CCDs. This upgrade successfully decreased the background to around 10^3 events/(keV_{ee}·kg·d) (red

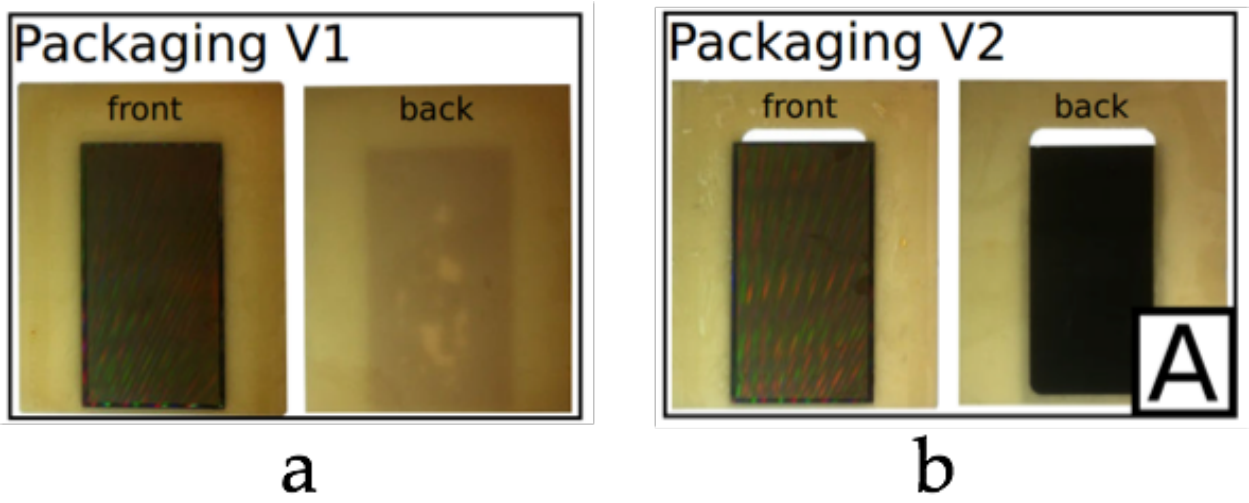

Figure 2.8: CCD with AIN packaging: a) full AlN support; b) AlN frame support.

dashed line in Figure 2.9 and 2.10).

A further improvement was achieved in January 2014, when we installed three CCDs with a new packaging where the detectors were glued on a silicon support (Figure 2.11(a)). The support was cut from the same high-resistivity silicon wafer used for the CCD fabrication, which guarantees an extremely low level of radioactive contamination. Also, these new CCDs were thicker than the DECam CCDs, two of them with 500 μm thickness and one of them with 675 μm thickness. The fabrication process for this last CCD was different from the 250 and 500 μm CCDs, where a transparent layer of indium-tin-oxide (ITO) is deposited after thinning the backside of the device to allow incoming light for applications in astronomy. The 675 μm CCD is un-thinned and lacks the ITO layer, which containa the slightly radioactive indium. Several months of operation at SNOLAB demonstrated stable and low-noise operation of these thicker CCDs. In Figure 2.12, we show the typical noise of 2 e^- (7 eV) of an image (a), and its stability (b) over a month of continuous data taking. A major achievement was the demonstration of full depletion of the 675 μm CCD, which validated the final design of the DAMIC100 experiment (Section 2.5). The energy spectrum measured with the silicon-package CCDs is shown in Figure 2.9 and 2.10 as a blue solid line. The background level of $5{\times}10^2$ events/($\mathrm{keV}_{ee}{\cdot}\mathrm{kg}{\cdot}\mathrm{d}$) was higher than expected, and stimulated further investigations on its origin. The bulk of this background was found to be compatible with the presence of ^{210}Pb in the lead shielding. This radioactive isotope with 22 years half life is usually present in modern lead with activities ranging from thousands to tens

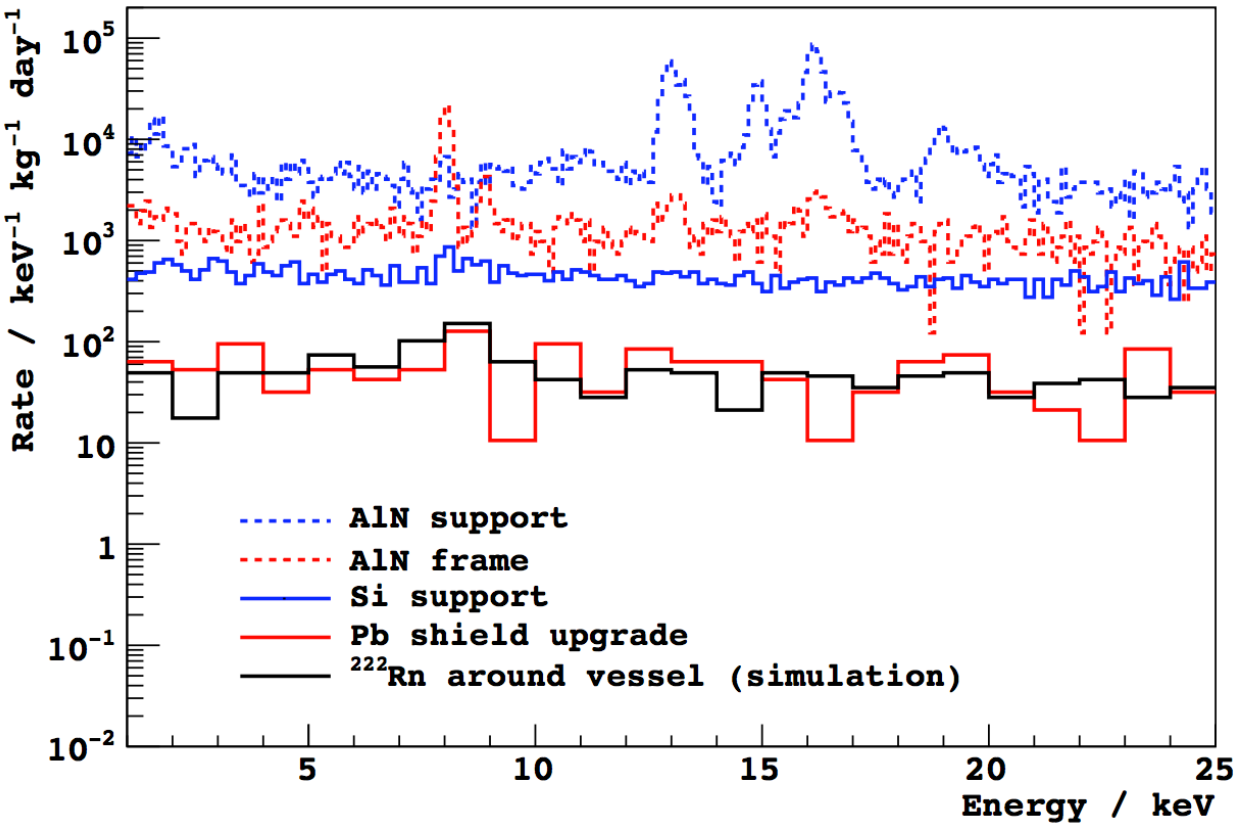

Figure 2.9: Background reduction at SNOLAB: energy spectrum between 1 and 25 keV measured by DAMIC after upgrades of the apparatus (see text for details).

of Bq/kg. High energy betas (∼1 MeV) from the ^{210}Pb decay chain produce bremsstrahlung photons which may escape the lead and generate Compton scattered electrons in the CCDs. The measured energy spectrum, which does not present X-ray peaks and is flat at low energy, is compatible with this hypothesis.

To reduce this background, the inner layer of the lead shielding was replaced in July 2014 by 1" of ancient lead (Figure 2.13), recovered from a sunken Spanish galleon, having a ^{210}Pb contamination <0.02 Bq/kg (to be compared with 50 Bq/kg of the original lead bricks). The upgrade of the lead shielding resulted in a tenfold reduction of the background to about 50 events/(keV$_{ee}$·kg·d) (solid red line in Figure 2.9 and 2.10). This residual background was compatible (black solid line in Figure 2.9 and 2.10) with the presence of radon in the air pockets between the lead shielding and the vacuum vessel. High-energy photons from the decay of ^{222}Rn can in fact produce Compton scattered electrons in the CCD.

Several other tests and upgrades have been performed during 2015. In particular, we

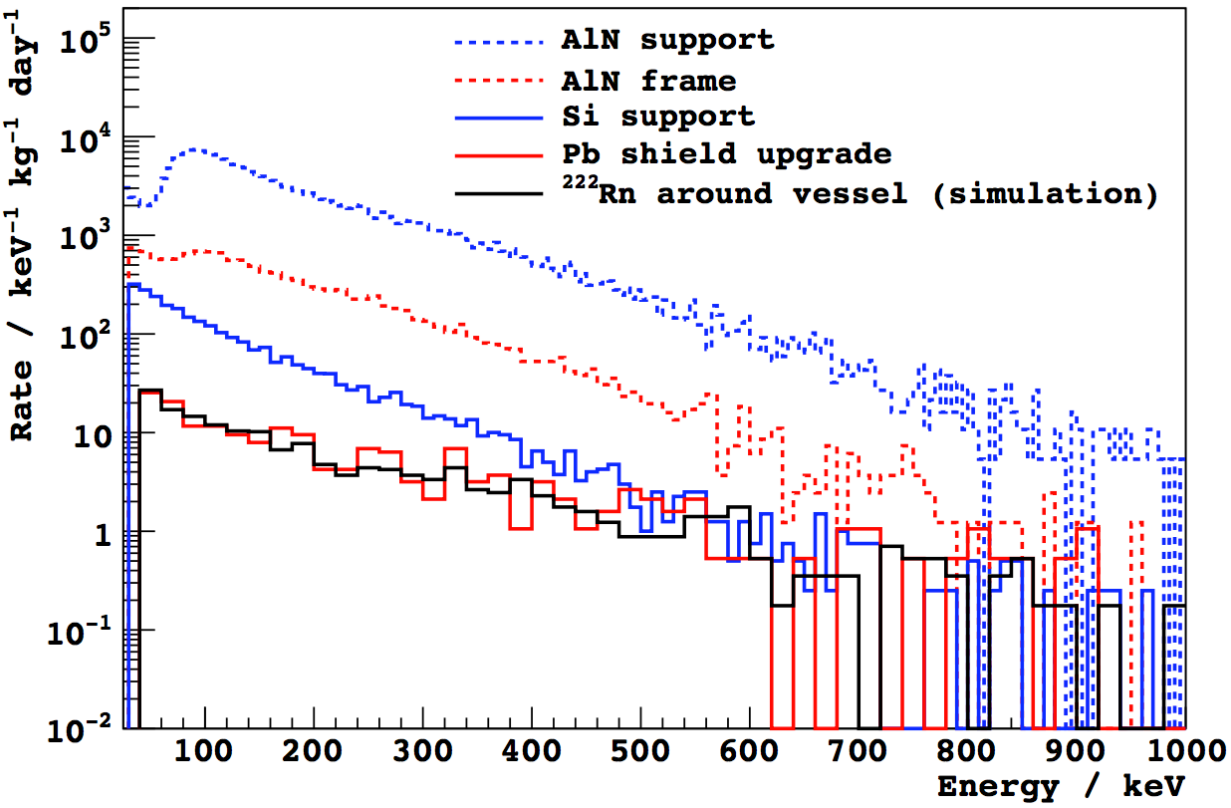

Figure 2.10: Background reduction at SNOLAB: energy spectrum between 25 and 1000 keV measured by DAMIC after upgrades of the apparatus (see text for details).

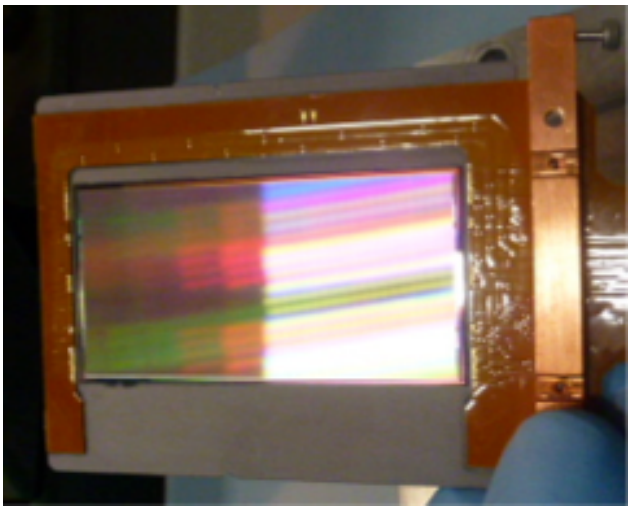

Figure 2.11: The new packaging with a CCD glued on a full silicon support, together with its kapton cable.

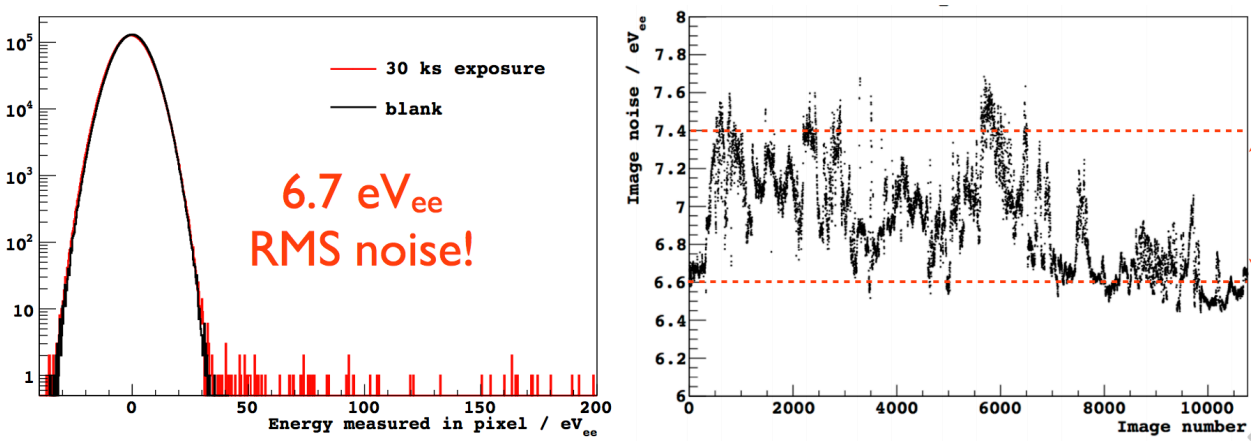

Figure 2.12: In (a), histogram of the pixel energy for a CCD image taken at SNOLAB. It demonstrates a gaussian noise with rms of ∼7 eV. In (b), the stability of the noise over a period of a month.

Figure 2.13: Upgrade of the lead shielding with the innermost layer made of ancient lead.

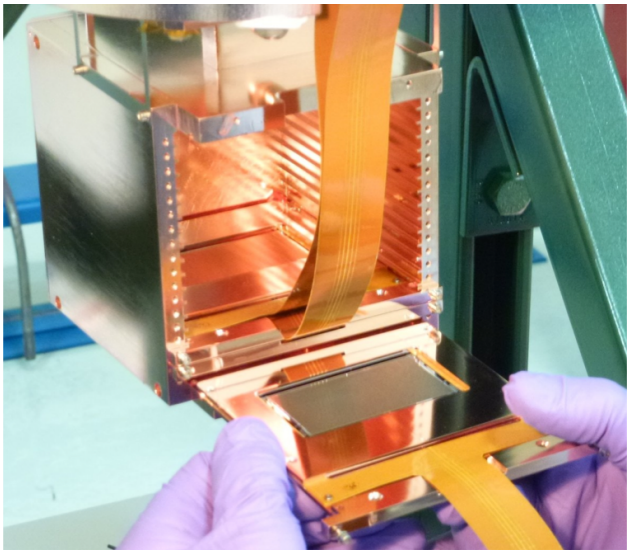

Figure 2.14: The new copper box which will house the 18 CCDs of of the DAMIC100 experiment. Also, shown is a CCD with the new DAMIC100 packaging ready to be inserted.

have successfully tested a new packaging which utilizes a silicon frame as support, further reducing the amount of material close to the CCDs. Several other 675 μm thick CCDs have been packaged and installed. We also installed an aluminum box enclosing the entire DAMIC shielding and flushed with nitrogen gas, which reduced the radon level from 130 Bq/kg to below 1 Bq/kg. Additional studies of the residual background are currently being undertaken, focusing on the radioactive contamination of the Oxigen-free copper used for the box and packaging of the CCD.

2.5 The DAMIC100 experiment

The DAMIC R&D program has successfully established the performance of large size, thick CCDs with very low readout noise. The latest version of DAMIC CCDs features 4k×4k pixels and 675 μm thickness, for a mass of ∼5.9 g each, with a low background packaging (Figure 2.4). The DAMIC100 experiment consists of 18 of these detectors, for a total mass of 100 g. It will be installed at SNOLAB, in the existing DAMIC infrastructure (Section 2.3). Minimal modifications of the present setup are required, since the shielding, vacuum vessel, electronics and data acquisition are adequate for DAMIC100. Only the copper box, CCD supports and Kapton cable have been redesigned to accommodate the larger CCD size (Figure 2.14). The copper CCD support can hold one 4k × 4k device, as well as two 2k ×

4k devices. The CCDs for DAMIC-100 have been designed at LBNL and manufactured by DALSA [24]. A total of 23 wafers have been produced, with one 4k×4k and two 2k×4k devices in each wafer. Cold probing performed at LBNL indicates a high yield ($> 90\%$) of usable devices (since the risky process of thinning is not performed in these CCDs, and a high yield is expected). Packaging of the CCDs is performed at the Fermilab SiDet facility, where extensive expertise exists from the DECam CCDs packaging. The copper box, supports and Kapton cables are already produced (Figure 2.14). At the time of the completion of this thesis, the new copper box has been installed in the vacuum vessel, and packaging of the 4k×4k DAMIC100 detectors has started.

CHAPTER 3
CCD DATA ANALYSIS AND CHARACTERIZATION

In the initial stage of the DAMIC experiment the analysis of the CCD images was performed with tools developed by the astronomy community for the goal of finding astronomical objects. These tools were soon found to be insufficient for the specific requirements of DAMIC. As part of this thesis work, we have developed a set of data analysis and simulation packages that are now the standard tools for the treatment of DAMIC data. In the following, we describe the main characteristics of the data analysis and simulation procedures, and their application to characterize the properties of DAMIC CCD, as the charge diffusion and the CCD response to electron-induced ionization.

3.1 CCD data reduction

The DAMIC CCD data are stored in a standard FITS format [25], including a header with relevant data acquisition and slow control parameters. Raw data corresponding to a portion of an image are shown in Figure 3.1, with pixels identified by their position on the x and y axis, and color representing the pixel charge in ADC counts. Several clusters of charge produced by ionizing particles (this image was taken at ground level where background is significant) are clearly visible. Clusters are identified through a data reduction procedure optimized to reduce the noise level in the image, involving several steps outlined in the following.

A. Pedestal Subtraction

A 2k×4k DAMIC image contains the digitized charge of about eight million pixels arranged in 2048 columns and 4196 rows. The charge of each pixel is given as a number between 0 and 65536 (16 bits) ADC counts. This value is proportional to the sum of the charge associated to the pixel noise and that produced by a ionizing particle (if any). In Figure 3.2 we show the distribution of the pixel charge in ADC count for one image. In general, the pixel charge has a gaussian distribution around an average value which depends on the pixel's column. Thus, the pixel charge distribution is fitted independently in each column i,

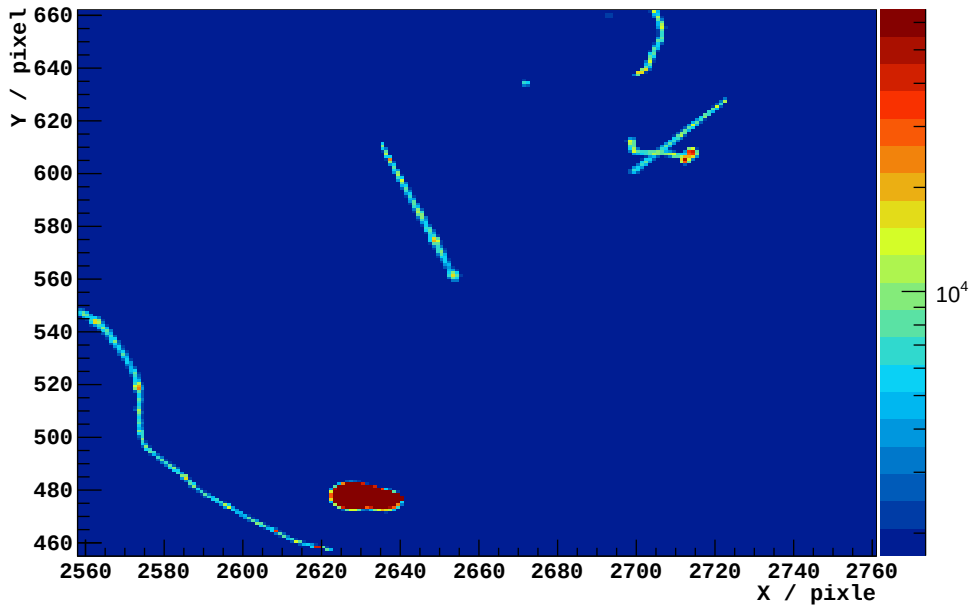

Figure 3.1: Raw data for a portion of a DAMIC CCD image, with with pixels identified by their position on the x and y axis, and color representing the pixel charge in ADC counts.

and its average μ_i (the pedestal) and standard deviation σ_i are obtained. The pedestal μ_i is then subtracted from the charge of every pixel of column i. The fitted μ_i as a function of the column number is shown in Figure 3.3: the variation of μ_i across columns is larger than the standard deviation σ_i, which makes the pedestal subtraction procedure effective.

B. Correlated Noise Subtraction

Part of the noise observed in the CCD is correlated which results in repetitive spatial patterns in the image (Figure 3.4). In DAMIC, we mitigate this kind of noise by making use of the redundancy built in the CCD readout. The charge in the serial register is readout through an amplifier located on the right side of the CCD. There is another amplifier on the left side which is also readout simultaneously. Thus, to each pixel charge R_i at the right amplifier corresponds a pixel charge L_i at the left amplifier, the latter charge only containing noise. Correlated noise produces a shift in the same direction of the pedestal value of R_i and L_i. This is apparent in Figure 3.4, where the correlated noise appears spatially symmetric in the two images corresponding to the right and left amplifier. The charge R_i in a given pixel is

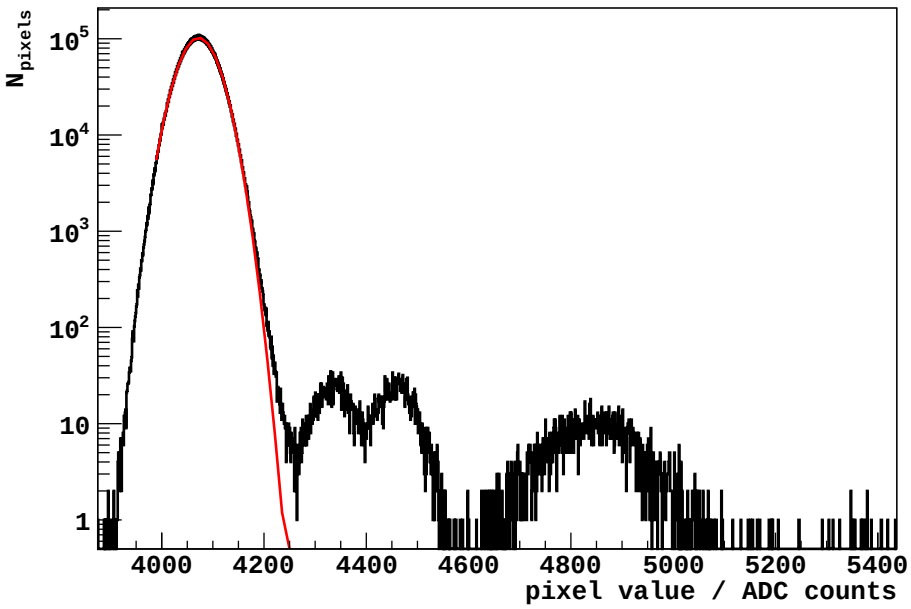

Figure 3.2: The pixel charge distribution for a single CCD image with about 8 million pixels. The red is a Gaussian fit of the pedestal. The standard variance of the fit is the RMS noise of the image.

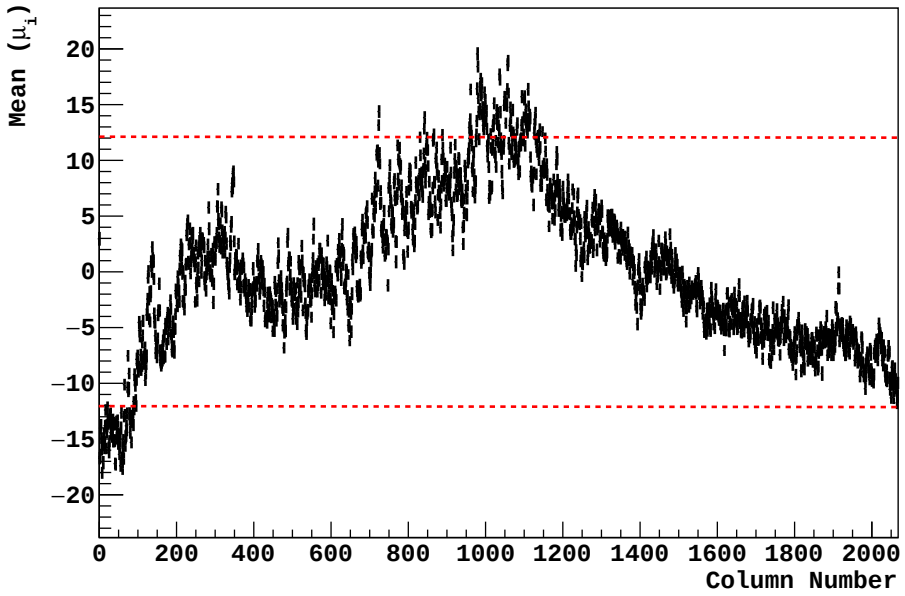

Figure 3.3: Fitted pedestal μ_i as a function of the CCD column i (only a portion of the CCD is shown for the sake of clarity).

related to the charge L_i in the symmetrical pixel by a linear relationship:

$$R_i = mL_i + c, \tag{3.1}$$

and an efficient procedure can be devised to subtract the correlated noise, illustrated in Figure 3.5. We take a row of pixels from the right amplifier image and the corresponding row from the left amplifier image. Then, we plot the two-dimensional correlation between the charge R_i of any pixel in the right image row and the charge L_i of the corresponding pixel in the left image row. The best estimate for the charge of a pixel is then obtained by subtracting from R_i the correlated noise estimated from the (R_i, L_i) correlation (Figure 3.5).

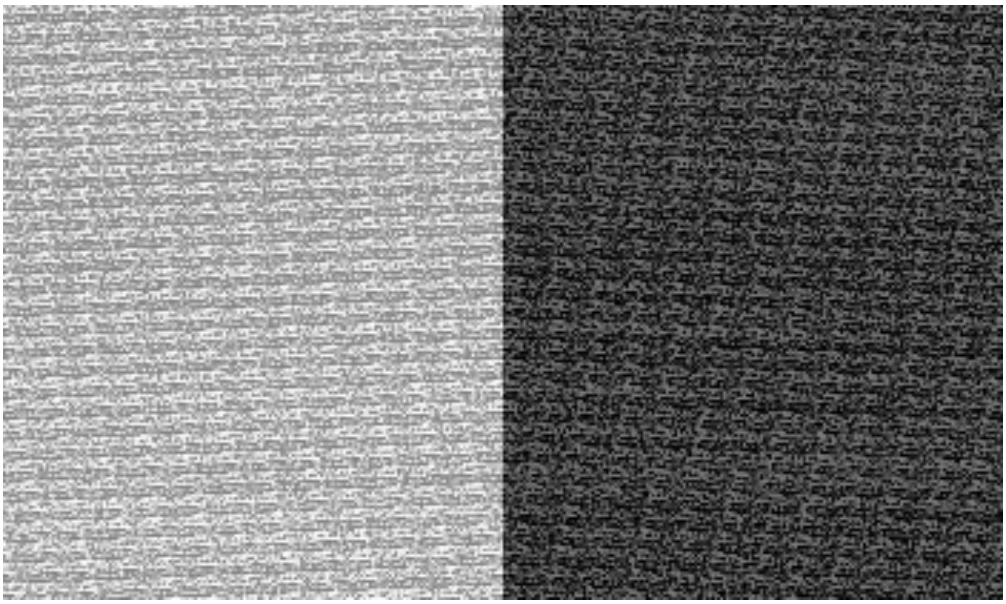

Figure 3.4: CCD image with correlated noise. Symmetric patterns of correlated noise are visible in the left and right side of the CCD, corresponding to the readout through the left and right amplifier (see text).

C. Master Bias

The CCD may present some localized defects which result in "hot" pixels with an abnormal value of the pedestal appearing in the same location over many images. An example is shown in Figure 3.6. These pixels must be properly treated in the analysis since they may be falsely reconstructed as energy clusters. Hot pixels are identified by calculating the mean pedestal of each CCD pixel using several images, and searching for pixels with a mean pedestal much larger than the majority of the pixels. A two-dimensional mask is then derived, and hot

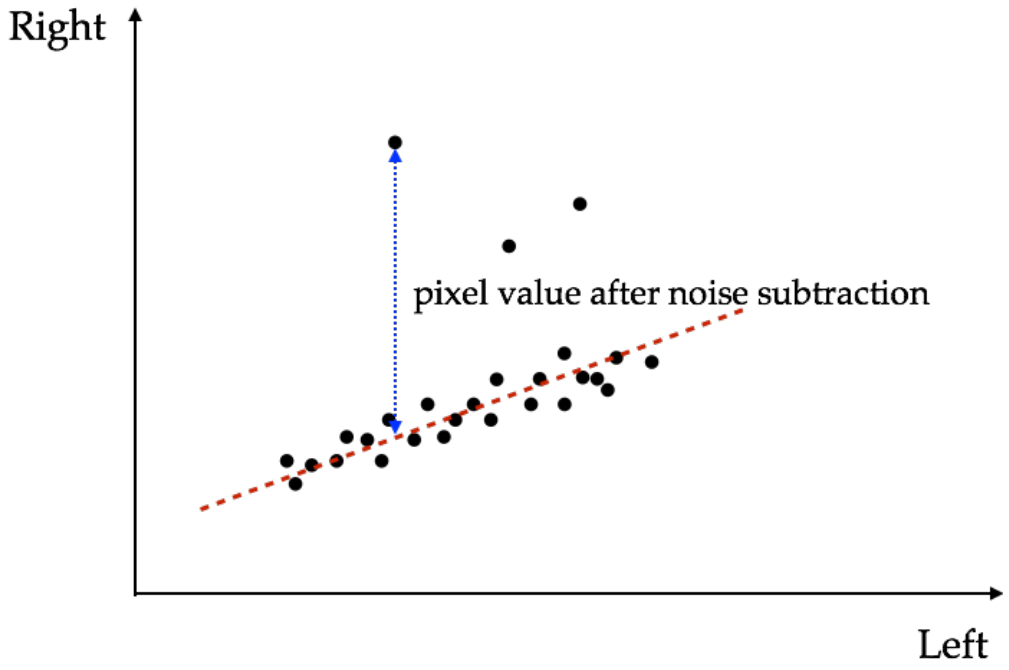

Figure 3.5: Illustration of the procedure for correlated noise subtraction. The vertical arrow indicates the best estimate for the charge of a pixel obtained by subtracting from R_i the correlated noise estimated from the (R_i, L_i) correlation.

pixels are excluded from further analysis.

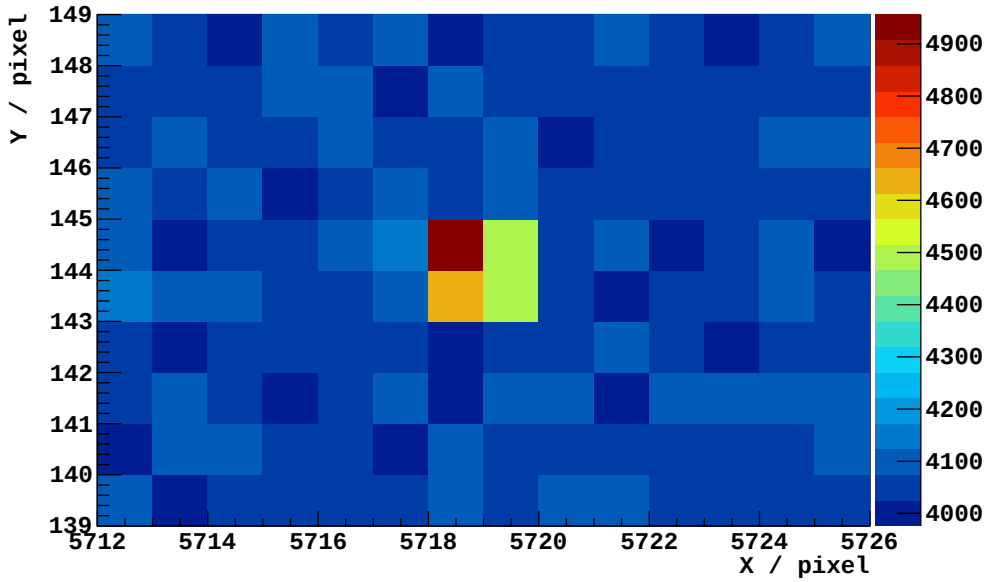

Figure 3.6: An example of a region with hot pixels, which can mimic a physical cluster.

D. Pattern Recognition

After steps A to C are completed, a pattern recognition algorithm is applied to the data to identify clusters of charge in the image as candidates for particle interactions. The search starts by selecting all pixels with charge greater than four times the standard deviation of the pixel pedestal, σ_{pix}. Each of these pixels is then used as a seed for further clustering. If any of the eight pixels surrounding the seed has a charge greater than 4 σ_{pix} (this value may be changed in the algorithm) it is marked as part of the cluster. This procedure is applied recursively to any new pixel associated to the cluster, till no more pixels above threshold are found. A more sophisticated clustering algorithm is described in Section 3.4.

E. Further Processing

Once a cluster is found by the pattern recognition algorithm, several quantities relevant for offline analysis are calculated, including the cluster energy and specific variables related to the its size and shape. An example of cluster is shown in Figure 3.7, with frequently used variables given in Table 3.1.

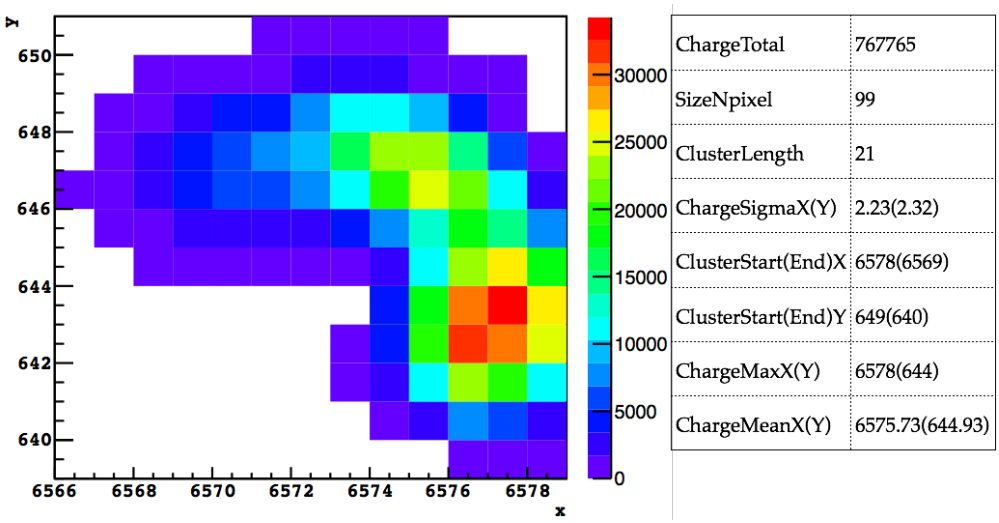

Figure 3.7: An example of selected cluster with its associated variables.

Variable Name	Definition
ChargeTotal	cluster energy in units of ADC counts
SizeNpixel	number of pixels in the cluster
ClusterLength	cluster length in units of pixels
ChargeSigmaX(Y)	standard deviation of pixel values along x(y) axis
ClusterStart(End)	start (end) point of the cluster
ChargeMaxX(Y)	X(Y) position of the pixel with maximum energy in the cluster
ChargeMeanX(Y)	X(Y) cluster position from a weighted mean of the pixels positions

Table 3.1: Definition of variables calculated for each cluster.

3.2 Simulation of particle interactions in CCDs

An important tool for the studies presented in this thesis has been the simulation of particle interactions in a CCD. We have used MCNP, a general-purpose Monte Carlo N-Particle code that is capable of neutron, photon, electron, or coupled neutron/photon/electron transport. It is developed and maintained by Los Alamos National Laboratory[26]. The code treats an arbitrary three-dimensional configuration of materials in geometric cells bounded by first- and second-degree surfaces and fourth-degree elliptical tori. The enlarged version MCNPX extends the capabilities of MCNP4C3 to nearly all particles, nearly all energies, and to nearly all applications without an additional computational time penalty. Besides, there is a PoliMi extension to MCNP and MCNPX which simulates fission events and subsequent interactions, and will be mentioned in Chapter 5. The neutron energy regime is from 10^{-11} MeV to 20 MeV for all isotopes and up to 150 MeV for some isotopes, the photon energy regime is from 1 keV

to 100 GeV, and the electron energy regime is from 1 KeV to 1 GeV. MCNP uses continuous-energy nuclear and atomic data libraries. The primary sources of nuclear data are evaluations from the Evaluated Nuclear Data File (ENDF)1 system [27]. Nuclear data tables exist for neutron interactions, neutron-induced photons, photon interactions, neutron dosimetry or activation, and thermal particle scattering. Photo-nuclear data are also included. MCNP is a well established Monte Carlo program unrivaled for low energy interactions, which makes it very appropriate for DAMIC. Most of our simulations have been performed with MCNPX. An typical input file for a simulation contains Cell Cards and Surface Cards which define the geometry of DAMIC CCDs, and Data Cards which define the physical characteristics of the simulation, including the type of source particles, the energy and spatial distribution of source particles, physics mode, output format and so on. For the specific application in DAMIC, we used customized TMesh tally which divides the CCD volume in 4196 $\times$ 2048 cells and records the depth where the energy deposit occurs. Then, a physically motivated diffusion model (Section 3.3) is applied to distribute the energy deposited in a pixel over surrounding pixels according to the depth of the interaction. Lastly, a gaussian noise of standard deviation as measured in data is introduced in the simulated image. An example of simulated CCD image with several electrons is given in Figure 3.8. We extensively used MCNP simulations to understand CCD data and estimate backgrounds.

3.3 Charge diffusion: measurements and parameterization

An important aspect of the CCD operation is the charge diffusion while drifting towards the pixel gates. Diffusion results in clusters whose spatial spread depends on the depth z of the interaction - a property which is very useful for the application of CCDs to searches of dark matter particles (Section 2.2). It can be shown [28] that the lateral charge spread of the holes at the potential wells is expected to be gaussian with a standard deviation σ given by $\sqrt{2Dt_{tr}}$ where D is the diffusion coefficient and t_{tr} is the holes' drift time. A physical model of charge diffusion model in thick CCDs [28] predicts a functional form

$$\sigma^2 = -Aln|1 - b(z - z_0)|, \tag{3.2}$$

where $A = 2k_BT\epsilon_{Si}/q\rho_D$, k_B is the Boltzmann constant, T is the temperature in kelvins, q is the hole charge, ϵ_{Si} is the permittivity of silicon, and ρ_D is the dopant density. The two

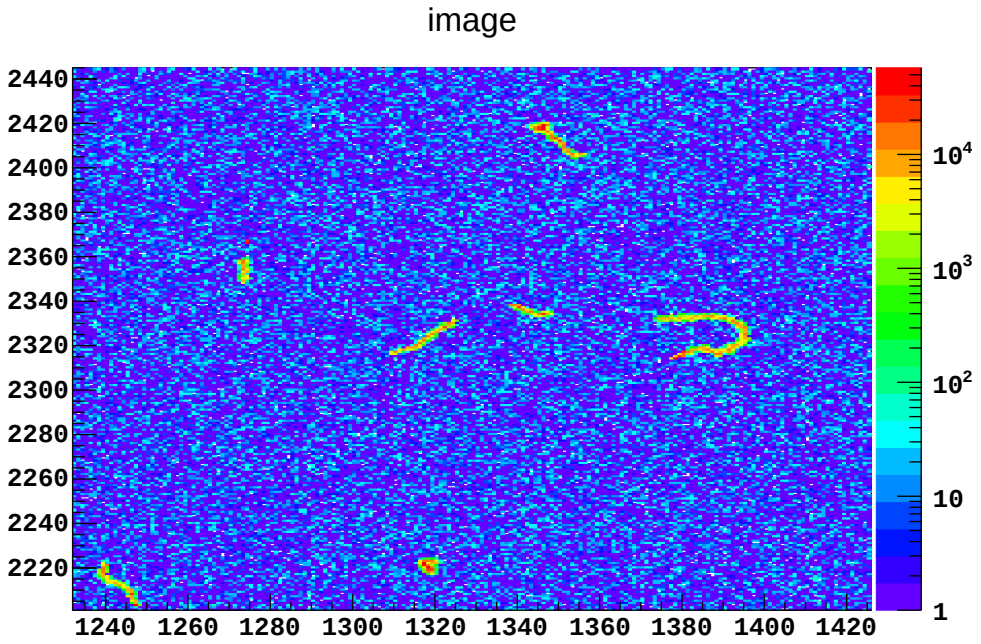

Figure 3.8: A simulated CCD image with several electrons.

parameters b and z_0 depends on the thickness of the CCD and on the potential across the depleted region.

We have developed a powerful method to characterize diffusion which makes use of CCD clusters induced by muons. A muon is detected as a straight track, with endpoints corresponding to the points of entrance and exit of the muon. The depth of any point along the track can be univoquely determined from simple geometrical considerations since the CCD thickness z_d is known. We expect the track to be "thin" for energy deposited by the muon close to the gates and "thick" for energy deposited close to the backside of the CCD. This effect is clearly visible in the example of muon track shown in Figure 3.9. To illustrate the general trend of the diffusion, we calculate for this muon track the spatial spread of the charge perpendicularly to the track as a function of depth, finding that a linear relation is a good approximation in the range of depths measured (Figure 3.10). For a more accurate determination of the diffusion model, we perform a maximum likelihood fit over a sample of muon tracks collected during test of the CCDs at ground level. The spatial distribution of the charge around the track is fitted assuming a charge diffusion given by Equation 3.2, taking into account the presence of gaussian pixel noise as well as the threshold used for pixel selection. Also, we assume a constant energy loss $\mathrm{d}E/\mathrm{d}l$ along the path l of the muon

in the CCD, which is left as a free parameter in the fit. Fitted as well are the track endpoints and the diffusion parameters z_0, σ_{max} (corresponding to the maximum of the diffusion at the CCD backside) and a, which are related to parameters A and b of Equation 3.2 through the relations:

$$\begin{aligned} A &= \frac{\sigma_{max}^2}{-ln(1-bz_d)} \\ b &= \frac{1}{z_d} - e^{-a}. \end{aligned} \tag{3.3}$$

The fit was performed over muon tracks collected with CCDs of different thicknesses and under different depletion bias voltages, providing a parameterization of the diffusion for different operating conditions. The resulting diffusion model was then included in the MCNP simulation (Section 3.2). To verify the correctness of the model for diffusion-limited clusters (as the ones expected for nuclear recoils) we exposed both the front and the back of a 250 μm thick CCD to X-rays from an ^{55}Fe source (Figure 3.11). A comparison of the reconstructed spatial spread of the clusters between data and simulation is shown in Figure 3.12, which shows good agreement.

3.4 Improved clustering algorithm

The pattern recognition algorithm described in Section 3.1 is not optimized to treat diffusion, which may spread the charge to a level where a pixel will not pass the 4σ selection. This results in lower efficiency and non-linearity in the energy determination due to the loss of charge, particularly for low-energy events. To mitigate these problems, we have developed an improved clustering algorithm which takes into account diffusion. The algorithm employs a maximum likelihood method to fit the charge in a given pixel as the sum of gaussian noise and signal from a 2-D Gaussian distribution (Figure 3.13):

$$N_e \times Gaus(x, y; \mu_x, \mu_y, \sigma(z)), \tag{3.4}$$

where N_e is total number of electrons produced by a point interaction, μ_x and μ_y corresponds to the position of the point interaction, and $\sigma(z)$ is the depth-dependent standard deviation of the charge diffusion model (Equation 3.2). Clusters are found by calculating the difference ΔLL between the best fit log-likelihood function (LL) of the 2-D signal charge hypothesis

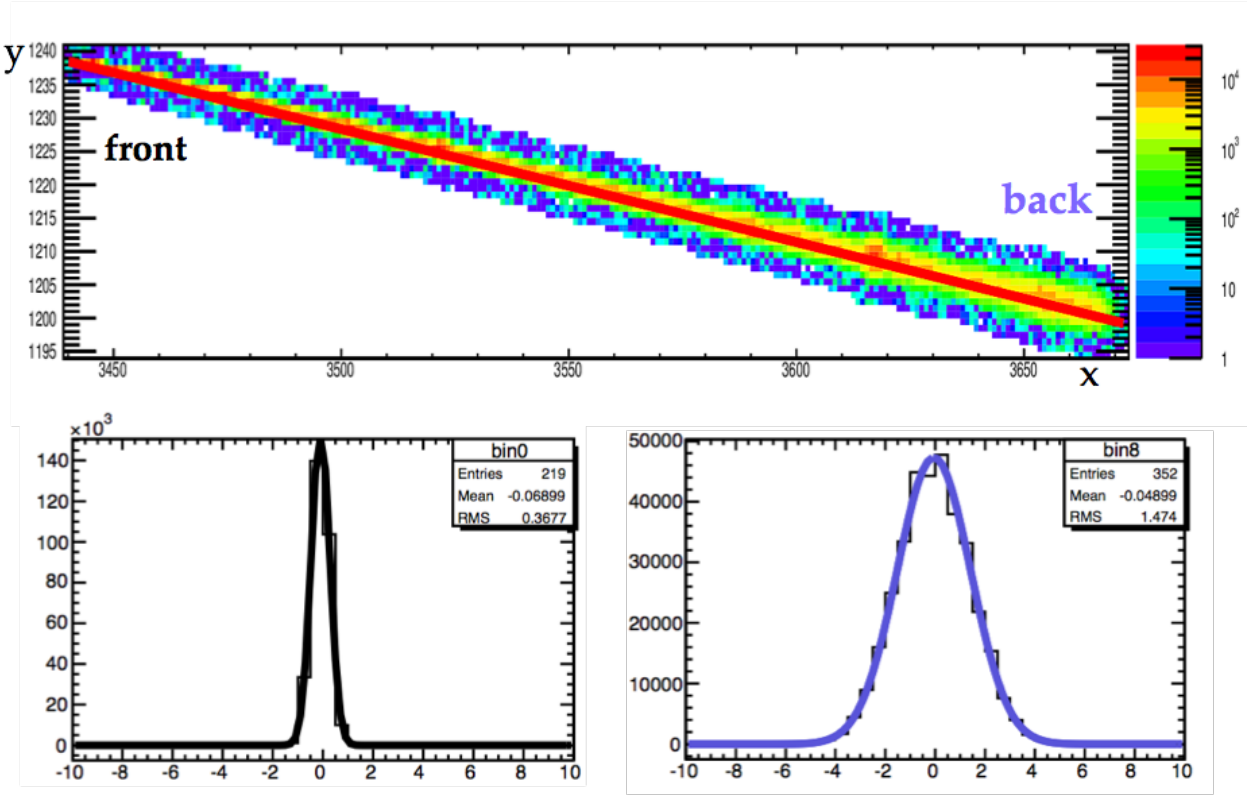

Figure 3.9: A muon track in a 675 μm thick CCD (top panel). On the bottom left (right) panel, the spatial spread of the charge calculated in a slice perpendicular to the track close to the front (back) of the CCD.

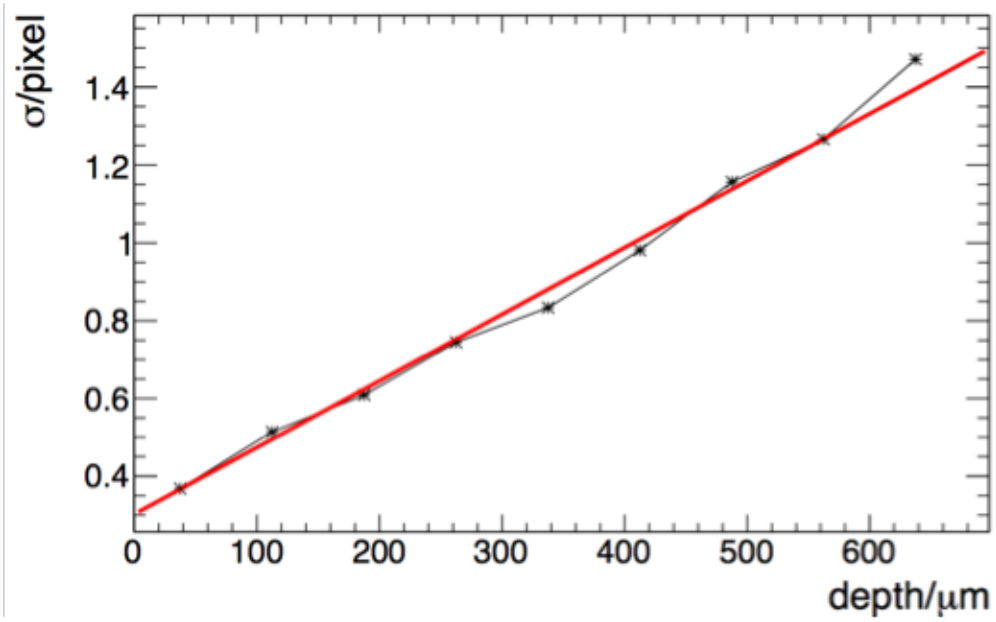

Figure 3.10: Spatial spread of the charge perpendicular to the muon track as a function of depth.

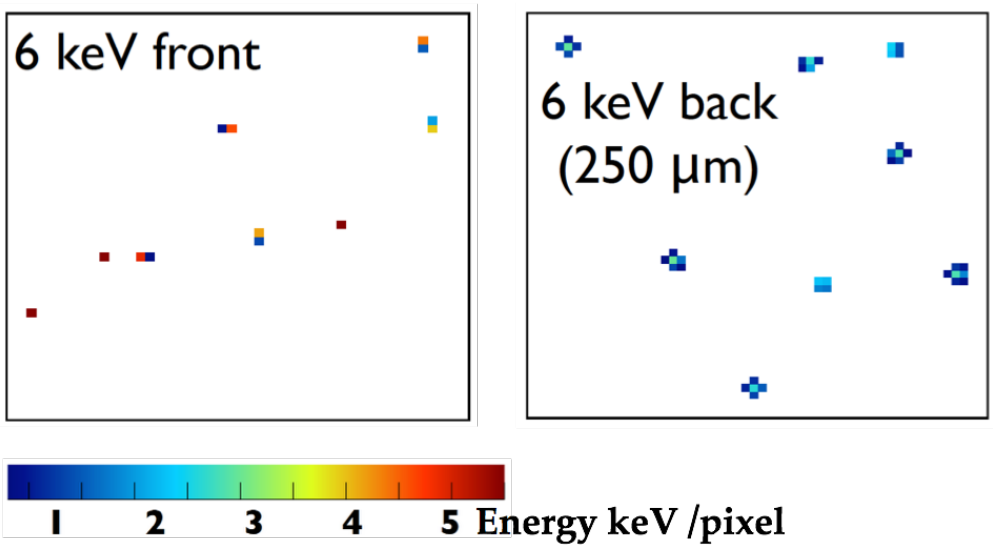

Figure 3.11: X-rays from a ^{55}Fe source illuminating the back (right panel) and front (left panel) of a 675 μm thick CCD.

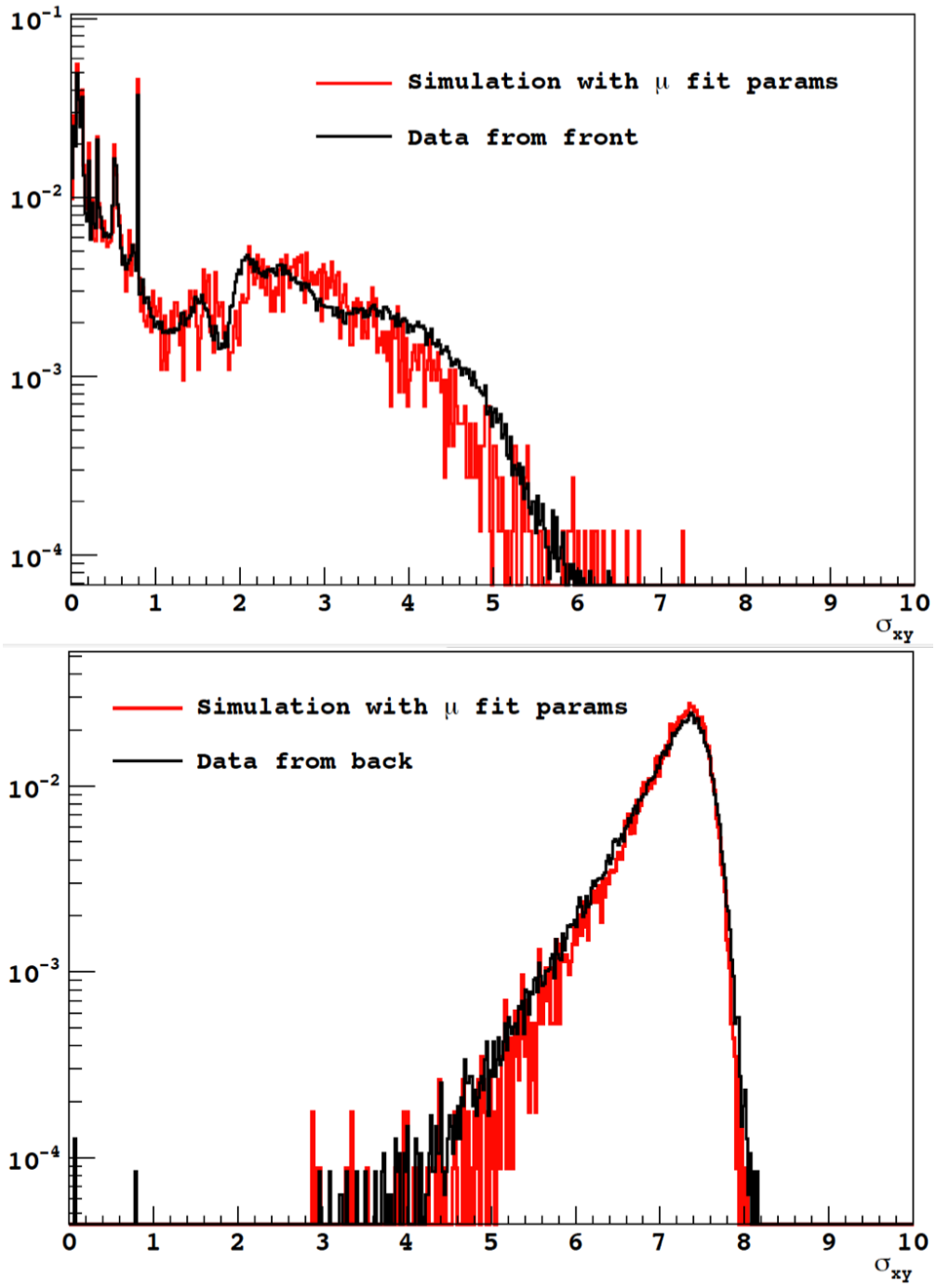

Figure 3.12: Comparison between simulation (red histogram) and data (black histogram) of X-rays from ^{55}Fe illuminating the CCD from the front (top panel) and back (bottom panel).

and the LL assuming only presence of noise. The difference ΔLL is calculated in a window of 7 pixels $\times$7 pixels (this is a typical size, the window is optimized depending on the thickness of the CCD and the applied depletion voltage) slid over the CCD image. The ΔLL distribution for a cluster search performed on data is shown in Figure 3.14 (black histogram). A similar study performed on simulated events shows that real events are optimally selected by requiring $\Delta\text{LL} < -22$. The performance of the "likelihood clustering" was evaluated by applying the algorithm to simulated events, and compared to that of the seed algorithm of Section 3.1. The selection efficiency obtained with the two methods is shown in Figure 3.15, while the energy reconstruction is shown in Figure 3.16. We find that the likelihood clustering provides a significant improvement in cluster finding and energy determination at the lowest energy.

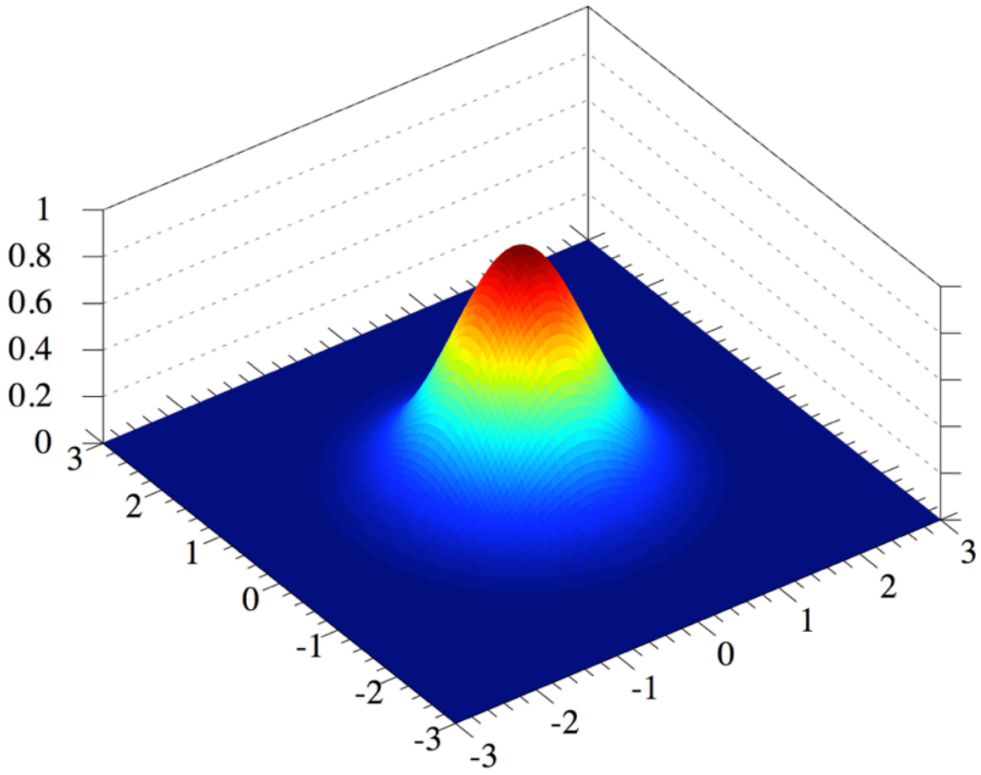

Figure 3.13: 2D Gaussian distribution of charge in 7 pixels $\times$ 7 pixels window used for the likelihood clustering algorithm.

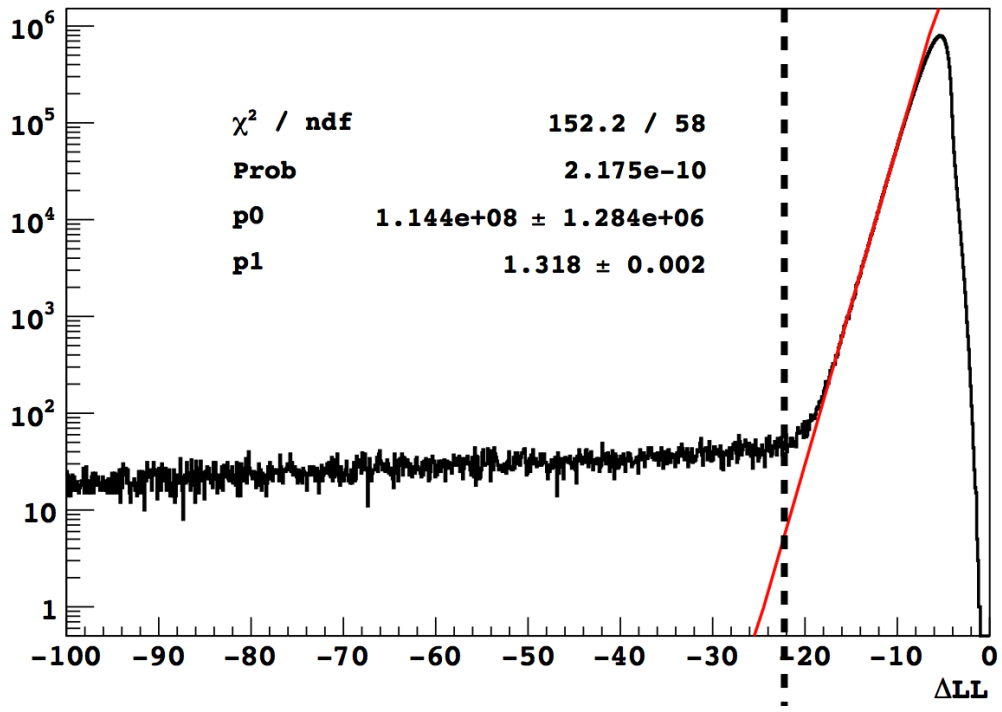

Figure 3.14: Distribution of the difference ΔLL for a cluster search in data. The events with ΔLL<-22 are considered candidates for physical events.

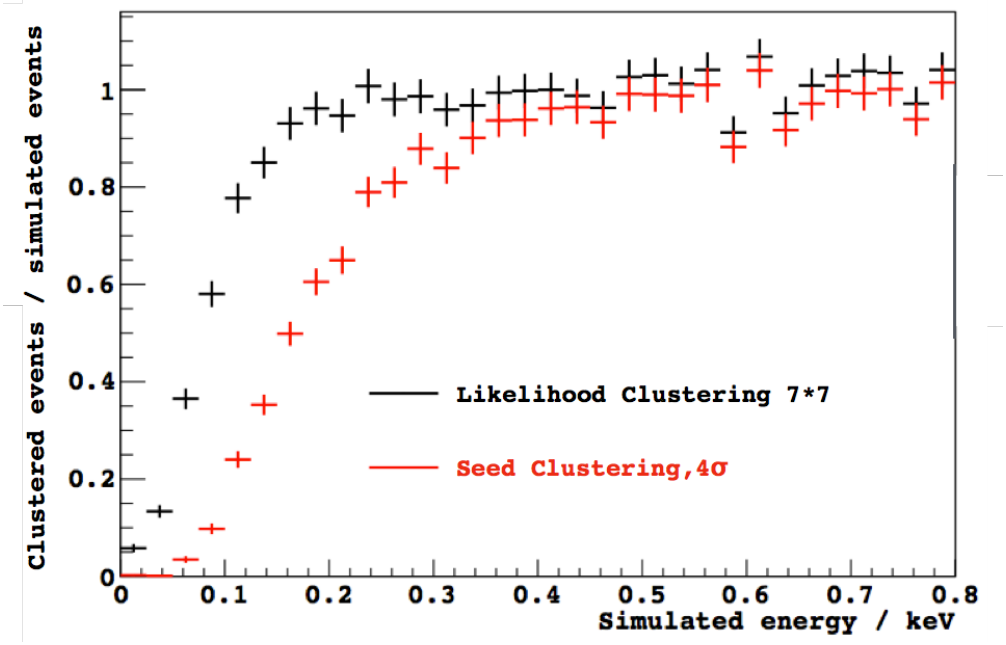

Figure 3.15: Comparison of likelihood clustering and seed clustering: selection efficiency as a function of cluster energy.

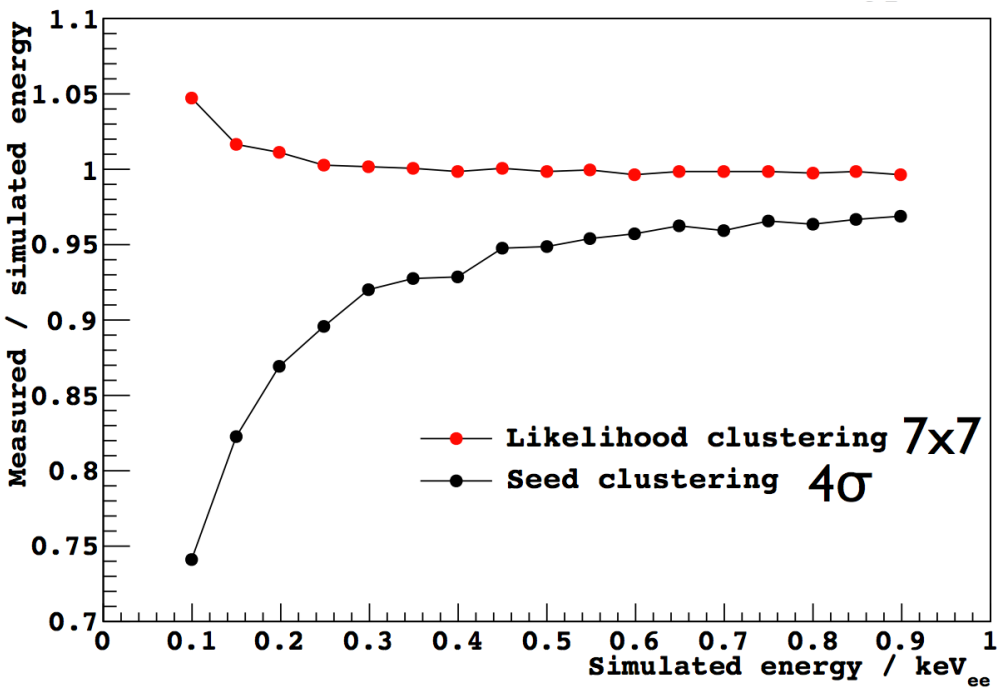

Figure 3.16: Comparison of likelihood clustering and seed clustering: ratio of the measured to simulated energy of the reconstructed cluster as a function of the cluster energy.

3.4.1 Calibration of CCD response to electron-induced ionization

We characterized the CCD energy response to electron-induced ionization by exposing the CCD to X-rays. The energy spectrum measured by a DAMIC CCD from exposure to a ^{55}Fe source is shown in Figure 3.17. The two main peaks of the spectrum are due to the K_α and K_β lines from the daughter Mn nucleus. The source holder is made of aluminum, which is the origin of the fluorescence Al Kα X-ray also observed. The main Mn K_α and K_β peaks are produced by X-rays that deposit their full energy in the CCD, while the Mn escape lines are due to partial energy deposits, where the subsequent Si fluorescence X-ray (1.7 keV) escapes the CCD. The absorption length of this X-ray is 14 μm, that is close to the size of a CCD pixel. Rarely, it occurs that the fluorescence X-ray travels far enough within the CCD so that its energy deposit is several pixels away from the first X-ray interaction, leading to two distinguishable clusters, as shown in Figure 3.18. Calibrations with fluorescence X-rays from a Kapton target exposed to the ^{55}Fe source or αs from ^{241}Am were also performed. Figure 3.19 demonstrates the linearity of the CCD in the measurement of ionization energy produced in the active region. The labeled Kx markers are fluorescence lines from elements

in the Kapton target and other materials in the CCD setup. The ^{55}Fe and ^{241}Am markers are X-rays emitted by the radioactive sources. Linearity in the measurement of ionization energy is demonstrated from 0.3 keV$_{ee}$ to 60 keV$_{ee}$[29]. For these calibrations the CCD was illuminated from the back, which, due to charge diffusion (discussed in 3.3), leads to a larger dynamic range and worse energy resolution than if the CCD had been illuminated from the front. Figure 3.20 quantifies the energy resolution of the CCD. The measured effective Fano factor, defined as σ^2/μ (σ^2 is the variance and μ is mean energy), is 0.16, larger than the accepted value of 0.1 in silicon, but typical for a CCD. Since the source illuminates the backside of the CCD, the charge is spread over many pixels. Thus, the readout noise added over many pixels leads to a limiting resolution of 30 eV$_{ee}$. This is shown in Figure 3.20, where the variance obtained from a gaussian fit of the energy distribution (see red line in Figure 3.17) is plotted as a function of the X-ray energy.

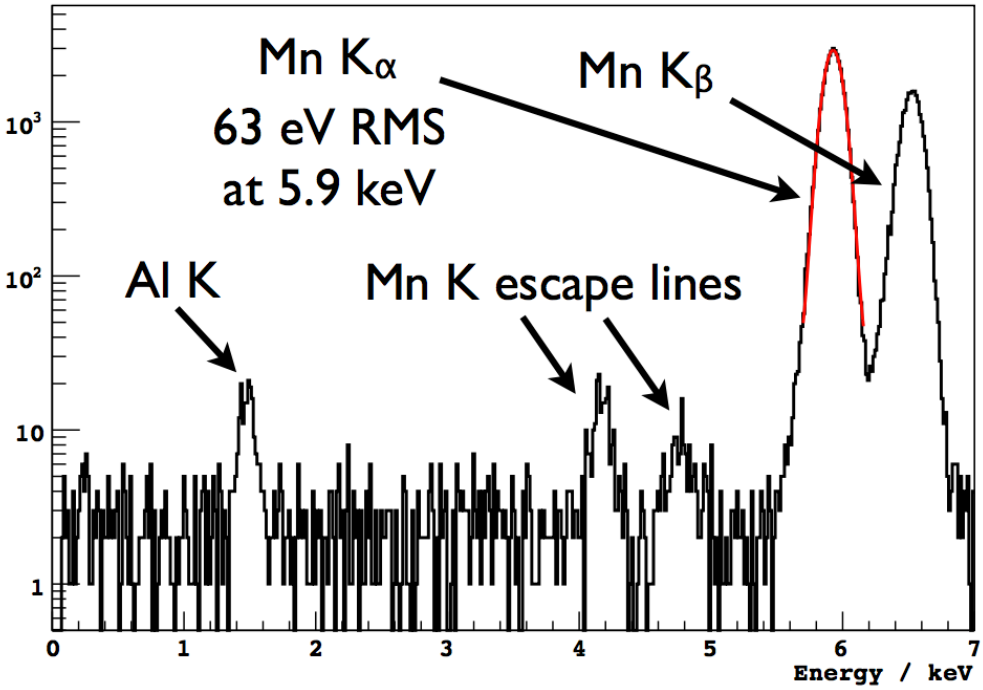

Figure 3.17: Energy spectrum measured by a DAMIC CCD exposed to a ^{55}Fe source. The two main X-rays from the source are the K$_\alpha$ and K$_\beta$ lines from the daughter Mn nucleus.

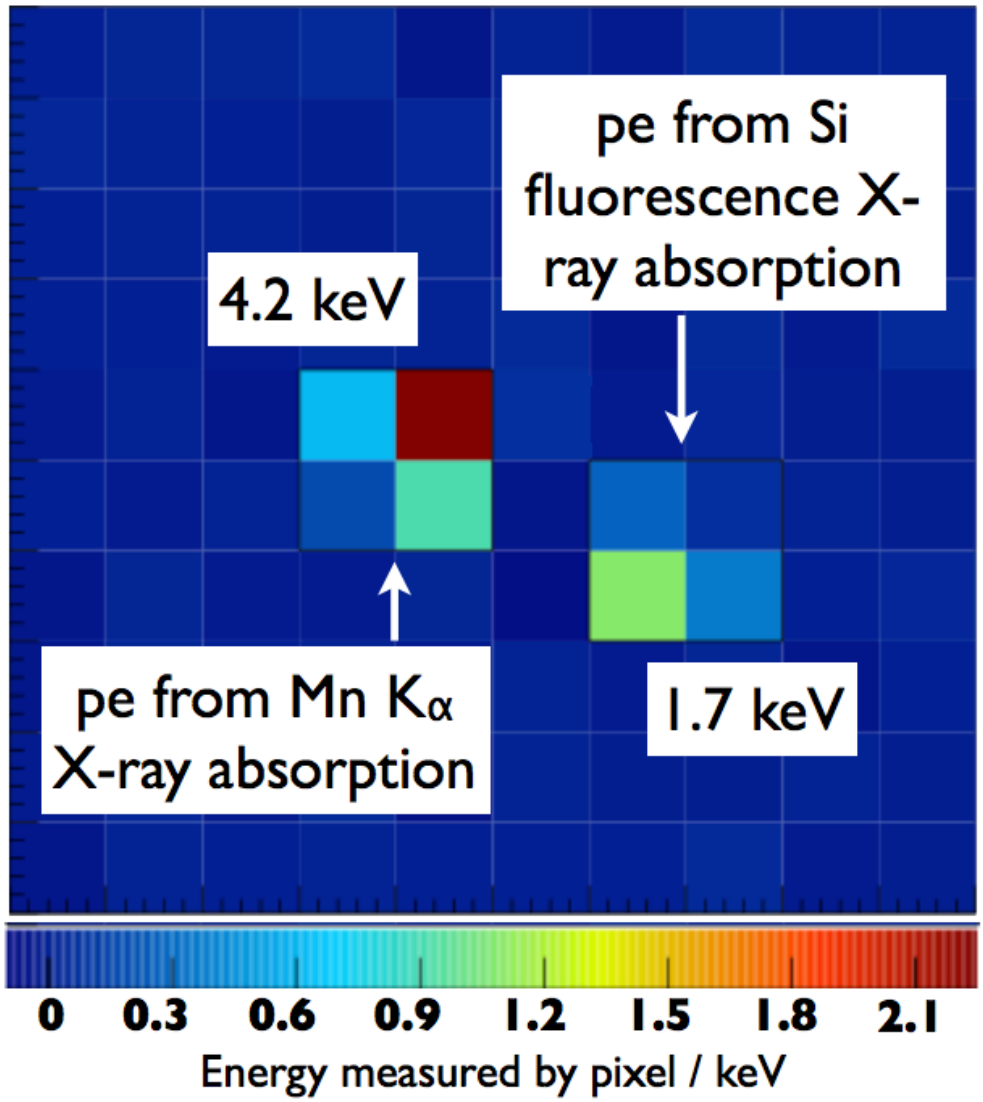

Figure 3.18: Example of a fluorescence X-ray traveling far enough in the CCD to produce a separate cluster.

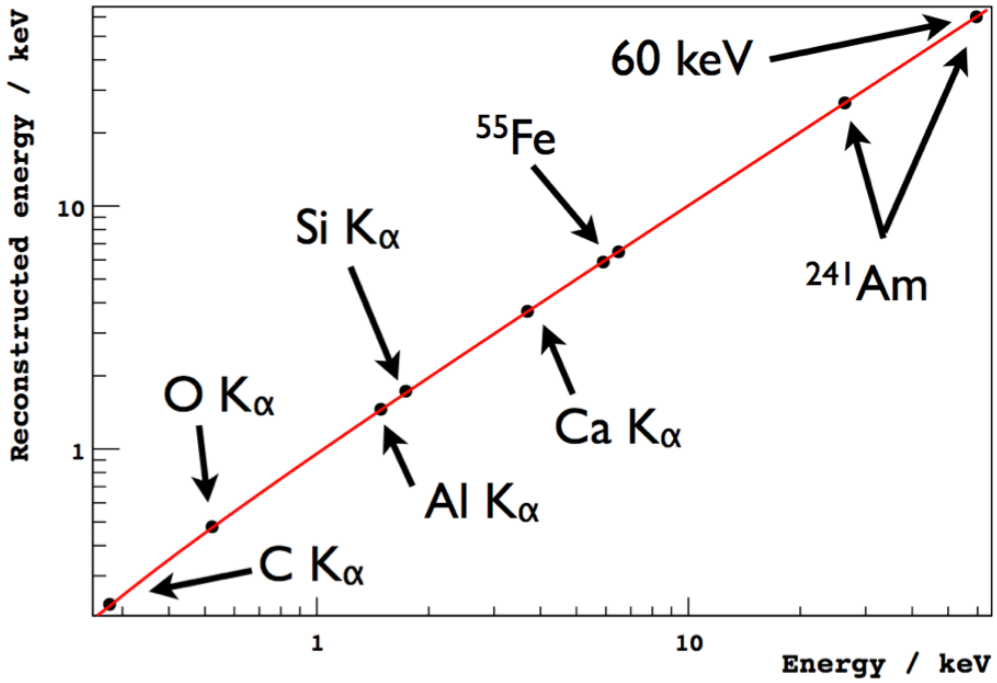

Figure 3.19: Linearity of the energy response of the DAMIC CCD: measured energy as a function of the energy of the X-ray.

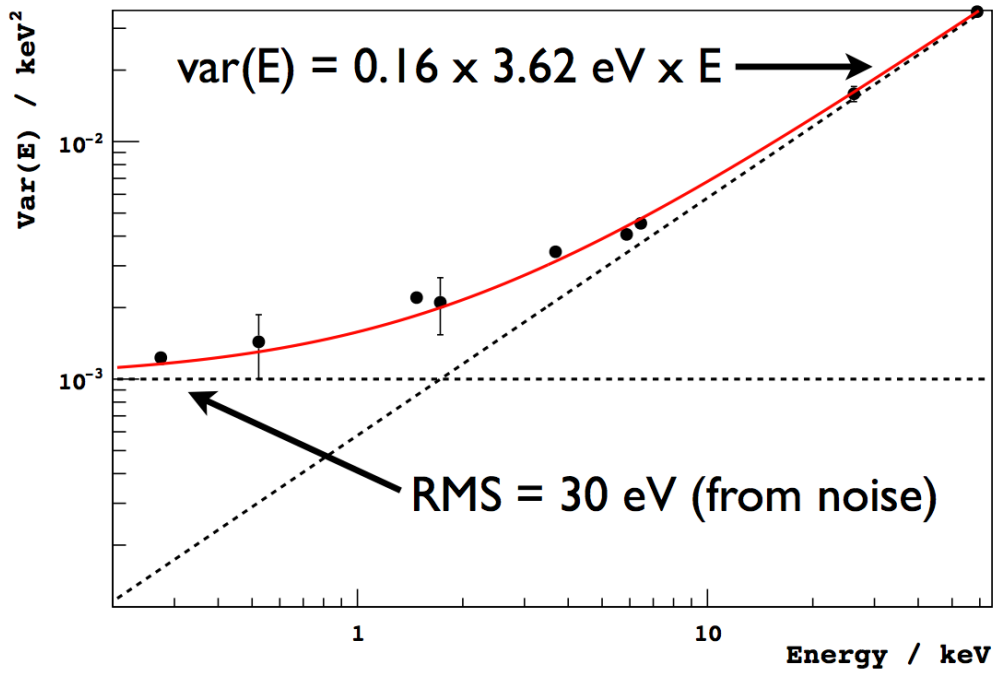

Figure 3.20: Energy resolution: variance of the energy as a function of the X-ray energy.

CHAPTER 4
BACKGROUND

4.1 Radioactive Sources

Radioactive background in a direct dark matter experiment should be analyzed and controlled. Radioactive isotopes in the detector are important potential sources of radioactive background.

4.1.1 Primordial Radioactivity

Many heavy elements found on earth were produced in supernova remnants which include radioactive isotopes with lifetimes that are sufficiently long for them to be present on earth in significant quantities today, yet not long enough for their radioactivity to be immeasurable. Half-lives and natural activities of common isotopes of such primordial radionuclei are presented in Table 4.1, among which ^{238}U , ^{232}Th and ^{40}K are dominant isotopes. The most common isotope of uranium found in nature is ^{238}U with a half-life of 4.5 billion years, constituting 99.28% uranium found on earth. Figure 4.1 [30] shows the decay chain of ^{238}U which decays by way of thorium-234 and protactinium-234 into uranium-234 with a half-life of 245 thousand years, emitting α-particles in the process. ^{234}U then undergoes a series of α decays into ^{214}Pb which decays into ^{214}Bi and to ^{214}Po with a half-life of 27 mins while producing high energy electrons and γ. The decay chain eventually terminates at ^{206}Pb. Another dominant primordial radionucleus, ^{232}Th produces a decay chain very similar to that of ^{238}U . The α particles, electrons and γ rays from these decay chains can cause significant backgrounds in DAMIC observations.

4.1.2 Man-made and Cosmogenic Radioactivity

Some radioactive sources are man-made isotopes. ^{60}Co is produced artificially in nuclear reactors with a half-life of 5.2 years and β decays to the stable isotope ^{60}Ni while emitting γ rays of 1.1 MeV and 1.3 MeV. High concentrations of ^{60}Co could be reached in the copper

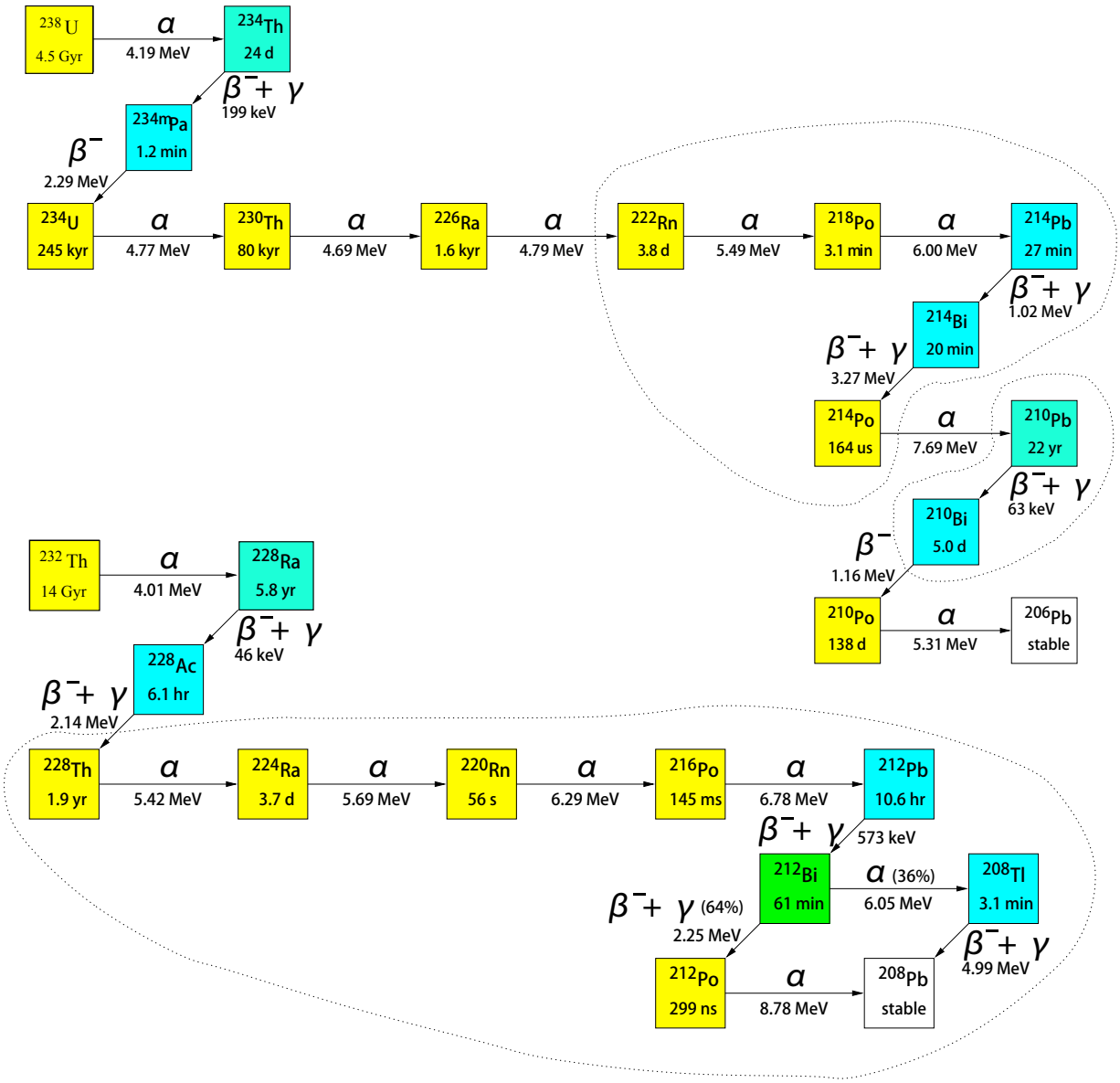

Figure 4.1: Decay Chains of ^{238}U and ^{232}Th . α (β) emitters are colored yellow (teal). For each isotope, α energies, β, Q-values, and half-lives are presented. Isotope sequences expected to be in secular equilibrium are grouped by dashed lines.

Nuclide	Symbol	Half Life	Natural Activity
Uranium 235	^{235}U	7.04 $\times 10^8$ yr	0.72% of natural uranium
Uranium 238	^{238}U	4.47$\times 10^9$ yr	99.28% of natural uranium;0.5 to 4.7 ppm total uranium in the common rock types
Thorium 232	^{232}Th	1.41$\times 10^{10}$ yr	1.6 to 20 ppm in the common rock types
Radium 226	^{226}Ra	1.6$\times 10^3$ yr	16 Bq/kg in limestone and 48 Bq/kg in igneous rock
Radon 222	^{222}Rn	3.82 days	Noble Gas; average air concentrations range from 0.6 Bq/m^3 to a few hundred Bq/m^3
Potassium 40	^{40}K	1.28 $\times 10^9$yr	soil - 0.037-1.1 Bq/g

Table 4.1: Primordial nuclides

used. And therefore the copper box and copper plates in the DAMIC detectors have been electropolished to remove any surface contamination. Cosmogenic nuclei are rare isotopes created when a high-energy cosmic ray interacts with the nucleus of an in situ Solar System atom, causing cosmic ray spallation. These rare isotopes are produced within materials found on earth, such as rocks and soil as well as the atmosphere. For example, ^{14}C ($\tau_{1/2}$=5.7 ky, Q=0.16 MeV) is produced by cosmic rays interacting with nitrogen in the atmosphere, and is absorbed into the Earth's biosphere in the form of CO_2. Another cosmogenic isotope important for DAMIC is ^{32}Si , produced when high-energy cosmic rays interact with Ar nuclei in the atmosphere. ^{32}Si β decays into ^{32}P which then β decays again into ^{32}S with a half-life of 14 days. The methods we use to estimate and reject the ^{32}Si background are discussed in detail in Section 4.5.

4.2 Screening

As discussed above, the background of DAMIC could come from ^{238}U , ^{232}Th , ^{40}K ^{32}Si , as well as other isotopes. Thus in order to estimate the background of DAMIC, we need to measure the radioactivity of every material in the detector. In general, we develop mainly two ways to measure the radioactivity - A: Glow discharge mass spectrometry (GD-MS)[31], and B: Germanium photon detectors. GD-MS is a mature, versatile technique for the direct determination of trace elements in a variety of materials. Solid samples are analyzed by exposing them to a gas discharge or plasma atomization/ionization source, sputtering the sample atoms into the plasma. The sputtered atoms could be analyzed by mass spectrometry which is an analytical chemistry technique. Thus GD-MS only requires a small amount of materials to obtain measurements with relatively high resolutions, making it possible to

measure the radioactivity of tiny and expensive parts in the DAMIC detectors.

4.2.1 High-purity Germanium (HPGe) Detectors

Germanium detectors are semiconductor diodes with a p-i-n structure within which the intrinsic region is sensitive to ionizing radiation, particularly x-rays and γ rays[32]. Under reverse bias, an electric field extends across the intrinsic or depleted region. When photons interact with the material within the depleted volume of the detector, charge carriers (holes and electrons) are produced and are swept by the electric field to the P and N electrodes. This charge, which is proportional to the energy deposited in the detector by the incoming photon, is converted into a voltage pulse by an integral charge sensitive preamplifier. Because germanium has a relatively low band gap, these detectors must be cooled in order to reduce the thermal generation of charge carriers (and therefore reverse leakage current) to an acceptable level. Otherwise, leakage current induced noise would destroy the energy resolution of the germanium detector. Liquid nitrogen, which has a temperature of 77 K, is the common cooling medium. The germanium detector is mounted inside a lead castle attached to an liquid N_2 Dewar. Figure.4.2 shows the HPGe detector we use to measure the radioactivity of materials.

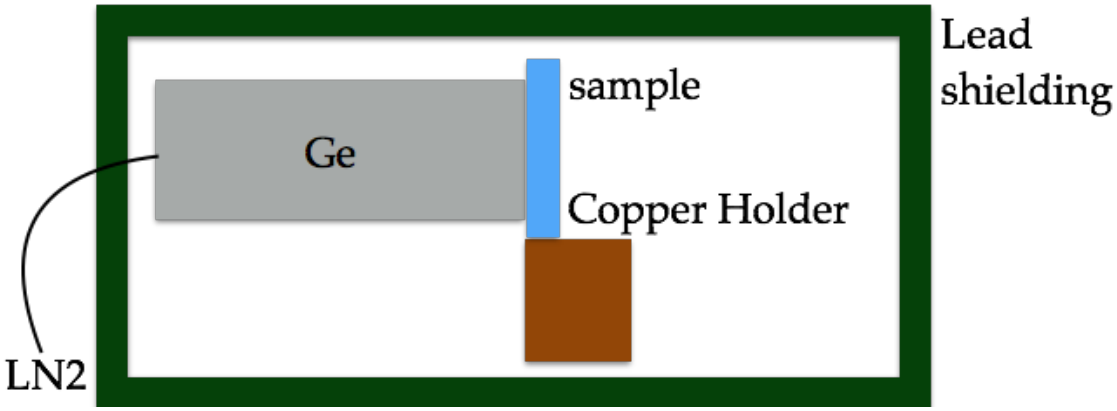

Figure 4.2: HPGe detector used.

4.2.2 Procedures

We develop the following procedure to measure the radioactivity with the HPGe detector:
1. measure the background radioactivity, mainly from the surrounding materials and ^{222}Rn

in the air, with the HPGe for 3 days.
2. put the material as close to the HPGe as possible, and record the mass and position of the material.
3. measure the material for 3 days.

After step 1-3, we obtain a spectrum for the X-ray and γ ray from the measurement. The result from when we screened the silicon support is shown in Figure 4.3 as an example. The red line shows the background and the blue line is with the silicon support. We could clearly see the excess along γ ray lines in the signal over background. The calibration from channel to energy is

$$E(\text{keV}) = -0.771 + 0.806 \times \text{N}. \tag{4.1}$$

N is the channel number in x-axis, shown in Figure 4.3. The X-ray or γ ray lines in Figure 4.3 are from ^{238}U , ^{232}Th , and ^{40}K decay chains. We use

$$\alpha = \frac{S}{t\epsilon IW} \tag{4.2}$$

to get the radioactivity, α, where S is the excess number of counts in the signal over background; ϵ is the detection efficiency for a given X-ray or γ ray line obtained from simulation with MCNP; t is the measuring time; W is the mass of the material; I is the decay branching ratio of this X-ray or gamma ray line. The main uncertainty of the measurement comes from the detection efficiency, ϵ, and the excess number of counts, S. The uncertainty in the former comes from the systematic uncertainty of simulations with MCNP, normally 10 -15%. The uncertainty in S is statistical, as $\sigma_S = \sqrt{N_0 + N_1}$, where N_0 (N_1) is the number of counts in a given X-ray or γ ray line in the background (signal).

4.2.3 Result

Results from measurements of radioactivity of materials used in DAMIC with both GD-MS and HPGe detectors are presented in Table 4.2.

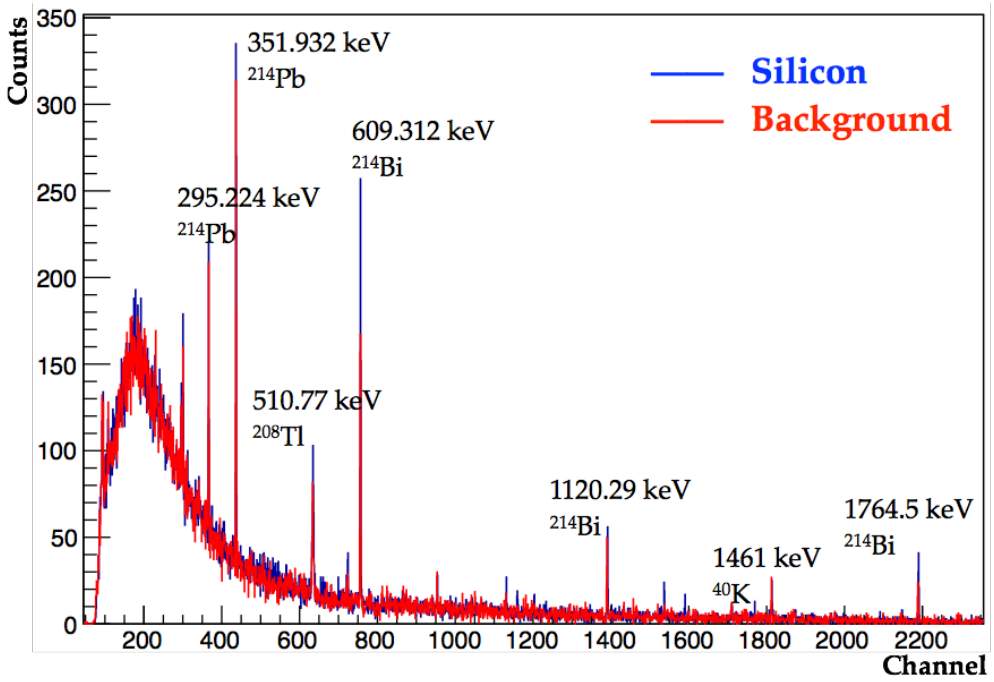

Figure 4.3: Spectrum of X-ray and γ ray from Si Support

Part	^{238}U	^{226}Ra	^{210}Pb	^{232}Th	^{40}K	other
	mBq kg^{-1}	mBq kg^{-1}	mBq kg^{-1}	mBq kg^{-1}	mBq kg^{-1}	mBq kg^{-1}
Kapton Cable	<460	<16	–	<14	118+/-88	-
EPOTEK	<12	<6.8	<0.5	1.12+/-0.07	13.3+/-3.5	^{14}C : 0.35
Si support	<0.36	0.36	<10^{-3}	<0.36	<4×10^{-4}	^{32}Si: 3.5
Copper slab	<0.6	–	0.5	<0.2	<0.03	^{60}Co: <0.6
DP110	–	<174	<0.5	10.6+/-1.5	620+/-60	–
VIB	–	10^3	–	30	350	–
Cold head	–	12	–	20	10	^{60}Co : 25
Pb block(old)	–	<0.12	(58 +/-18)×10^3	<0.04	<0.16	–
Cu vessel	–	<0.12	–	<0.04	<0.16	^{60}Co : <0.6
Pb shield	–	<0.12	(58 +/-18)×10^3	<0.04	<0.16	–

Table 4.2: Screening Results

Part	mass	rate in CCD
	g	events/(keV$_{ee}$·kg·d)
Kapton Cable	0.75	<5
EPOTEK	0.35	<0.5
Si support	7.7	0.3
Copper slab	36.4	<0.7
DP110	0.06	<0.01
VIB	1000	<0.7
Cold head	4500	<0.2
Pb block(old)	5.07×10^4	12+/-4
Cu Vessel	2.95×10^4	<60
Pb shield	4.9×10^6	75+/-23
Poly shield	4.6×10^6	<0.5

Table 4.3: Radio active background in DAMIC.

4.3 External Background in DAMIC

We determine the radioactive background in the CCD caused by contamination in the CCD package and surrounding materials through simulations. The geometry of the detector with the CCD, its packaging materials, and mechanical structure are shown in Figure 4.4. The whole detector is inside a polyethylene wall 40 cm thick. The copper vessel inside the lead (gray) castle contains the cold head and the VIB board. The copper box inside the castle includes three 675 μm CCDs each with 100 μm thickness Epoxy, a Kapton Cable, a 650 μm silicon support, a 2mm copper frame, a copper cover, and screws. Using isotopes with radioactivity represented by the screening measurements of materials discussed in the previous chapter as source particles in the simulations, uniformly distributed in the cell, MCNPX generates energy deposit within each pixel in the CCD. We present an example of how we simulate background from the Si support. Figure 4.5 shows the energy spectrum of ^{238}U decay chains. We simulate 60 images with 10000 decays of ^{238}U per image, corresponding to 6×10^5 decays in total. The simulated deposit energy spectrum in the CCD is shown in Figure 4.6. The background caused by ^{238}U in the Si support is about 3.5 events/(keV$_{ee}$·kg·d) in the 1-10 keV range. Table 4.3 shows the background in DAMIC from simulations.

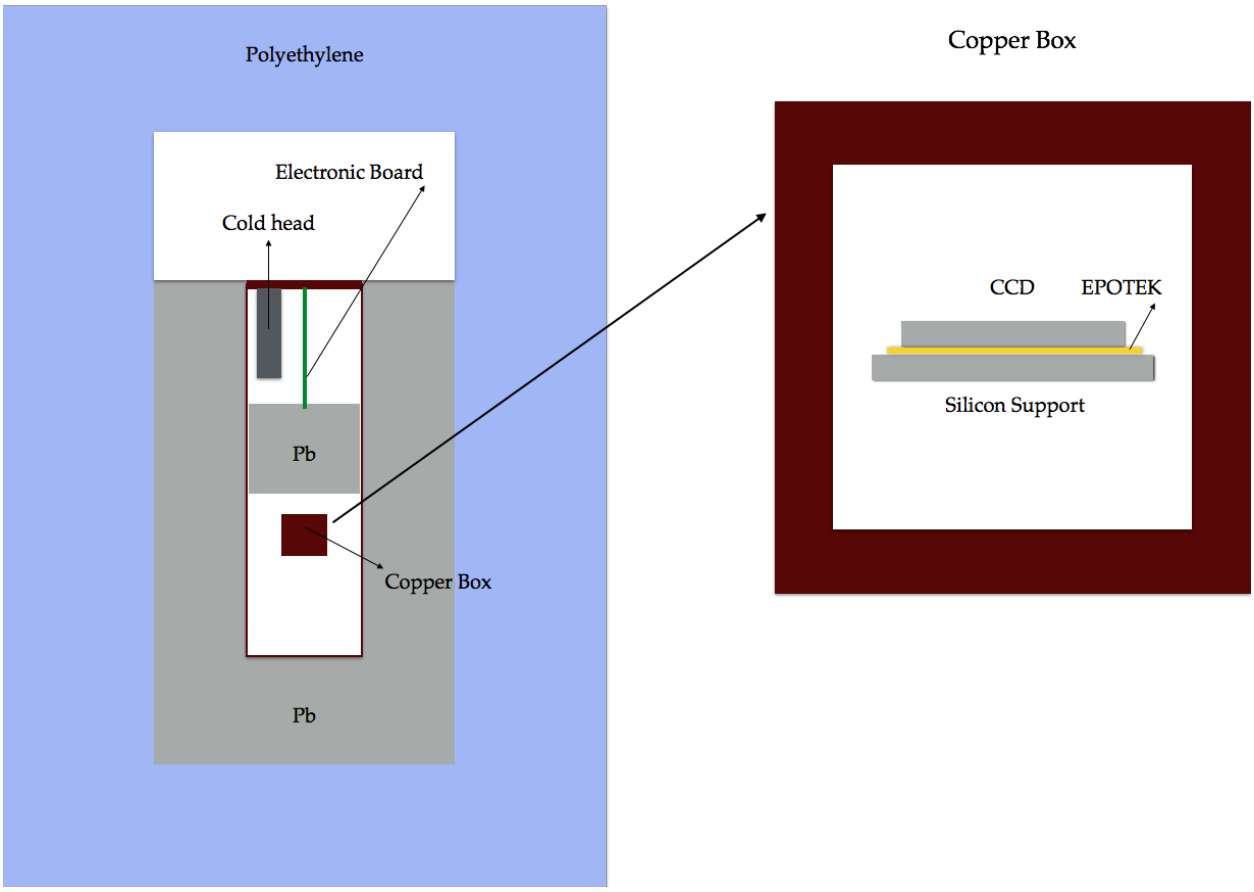

Figure 4.4: Geometry of the setup defined in the MCNPX simulation, including the polyethylene wall, the lead castle, the copper vessel, the cold head, the VIB, and the CCD with its packages contained in the copper box.

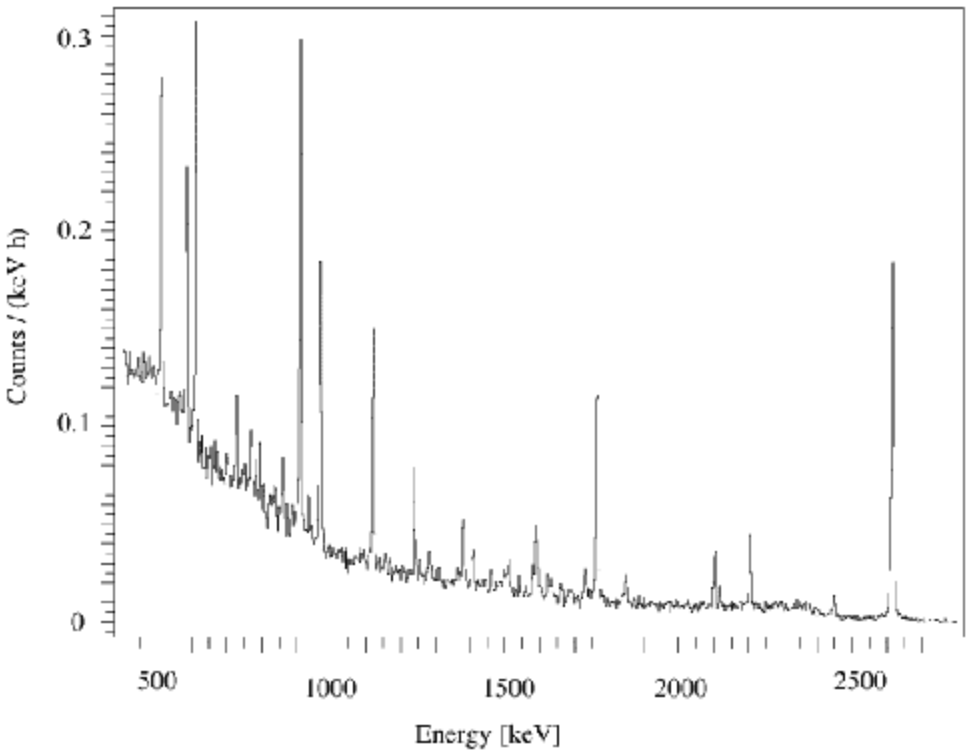

Figure 4.5: Spectrum from the ^{238}U decay chain.

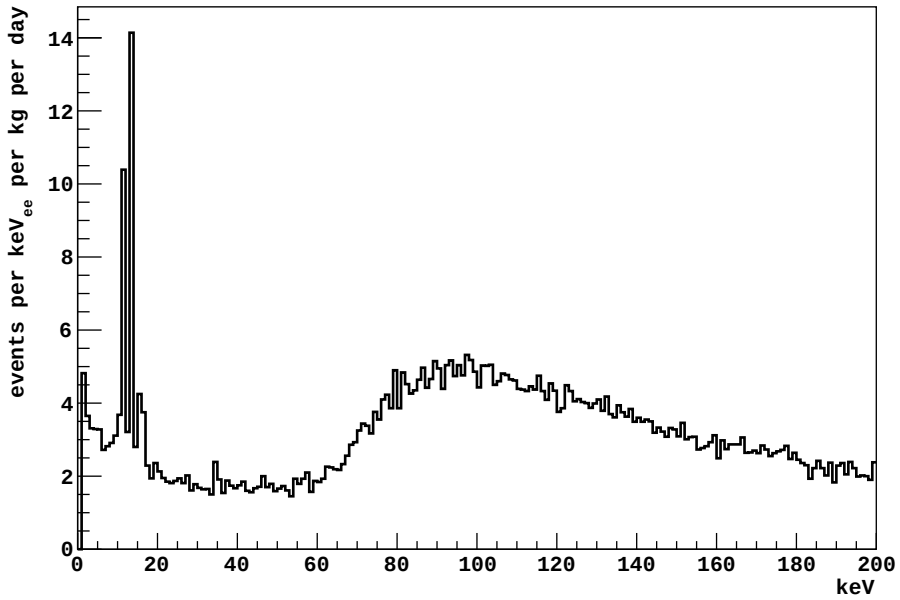

Figure 4.6: Simulated spectrum of X-rays and gamma rays from the ^{238}U decay chain in the silicon support with MCNPX.

4.4 Limits on Uranium and Thorium contamination from α spectroscopy

Uranium and thorium and their decay products (Figure 4.1) are ubiquitous in nature. They may be found within the bulk silicon of the CCD or the electrical elements of the device. They may also be present on the surface of the CCD, in particulates (e.g. dust) or as adsorbed radon daughters (mainly via deposition of ^{218}Po from ^{222}Rn decays in the air surrounding the device).

The CCD is >99.5% electronic-grade silicon [33] by mass. The remainder consists of light elements used in the oxidation, metallization and doping of the silicon to fabricate the semiconductor structures necessary for operation. Due to the extremely high chemical purity of the silicon, the substrate (photosensitive volume in Figure 2.1) can be doped with a donor density as low as $10^{11}\,\mathrm{cm}^{-3}$ [34]. Thus, even an unexpectedly large contamination of ^{238}U or ^{232}Th with an atomic abundance ∼10% of the donor density would only correspond to ppt (10^{-12}) levels by mass.

The CCDs are consistently handled in ESD-safe clean rooms (class 1000 or better). DAMIC CCDs are packaged at Fermilab, with facilities developed for DECam, an astronomy camera whose requirements for the deposition of dust on the CCD surface are much more stringent than that of DAMIC. However, the clean rooms are not radon-free, and deposition of radon daughters, mostly on the front CCD surface, will occur during the packaging. In particular, after being glued to their support, CCDs are left for two days under an air column of a few centimeters in height to cure the epoxy. We estimate that this procedure may induce a residual surface activity of ^{210}Pb and its daughters of less than -3×$10^3\,\mathrm{cm}^{-2}\,\mathrm{d}^{-1}$, assuming a typical ^{222}Rn activity for indoor air of $30\,\mathrm{Bq\,m}^{-3}$.

Many of the isotopes in the ^{238}U and ^{232}Th decay chains (Figure 4.1) are α emitters, and can be efficiently identified by α spectroscopy.

4.4.1 Characteristics and selection of α-induced clusters

Radiogenic αs lose most of their energy by ionization, creating a dense column of electron-hole pairs that satisfy the plasma condition [35]. The local electric field within the plasma is much greater than the electric field applied across the substrate. For interactions deep in the substrate, where the electric field is only along z, the charge carriers diffuse laterally toward

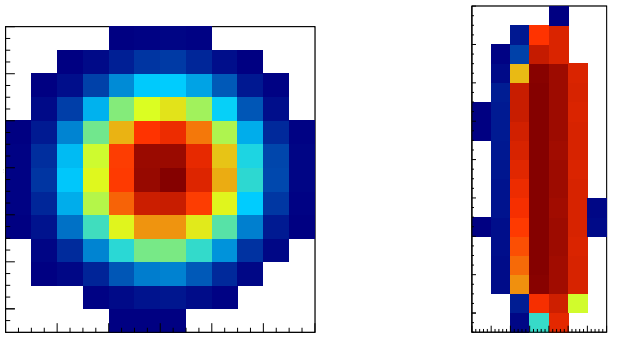

(a) Plasma α (b) Bloomed α

Figure 4.7: a) A highly-diffuse, round cluster due to plasma effect from an α particle originating in the bulk or the back of the CCD. b) An example of blooming, where an α particle originating in the front of the CCD produces a mostly vertical cluster.

regions of lower charge concentration until the substrate electric field becomes dominant. Thus, αs originating in the bulk or the back surface of the CCD lead to highly-diffuse, round clusters of hundreds of micrometers in diameter. On the other hand, α particles that strike the front of the CCD deposit their energy less than 20 μm below the gates. The high-density charge cloud can easily overcome — and spillover — the barrier phases between vertical pixels, while it is harder for it to overcome the potential barrier of the vertical channel stops between columns. This phenomenon is known as blooming [18], and leads to mostly vertical clusters. Examples of "plasma" and "bloomed" αs detected in DAMIC are shown in Figs. 4.7(a)- 4.7(b).

Due to their distinctive features, simple criteria are sufficient to efficiently select and classify αs. In the energy range of radiogenic αs (>1 MeV), electron tracks are long (∼mm or more) and deposit their energy in extended "worm"-like tracks over many CCD pixels. To differentiate electrons from αs, we determine the smallest rectangular box that can contain a cluster, and compute the fraction of pixels, $f_{\rm pix}$, in this "bound box" which are part of the cluster. For small, symmetric clusters (i.e. αs) $f_{\rm pix}$ is large ($\sim\pi/4$ for a round cluster). For the long and irregularly shaped worms characteristic of electrons, $f_{\rm pix}$ is small and decreases with increasing electron energy. Figure 4.8 shows the successful separation between βs and αs in the low-gain data set according to this variable.

To further distinguish plasma from bloomed αs, we calculate the spatial RMS $\sigma_{x,y}$ of the cluster as the signal-weighted RMS value of the pixels' x,y coordinate. Plasma αs present a round-shaped cluster, with $\sigma_x/\sigma_y \sim 1$, while bloomed αs are generally longer along the

y axis, giving $\sigma_x/\sigma_y<1$. In addition, the diffused clusters from plasma αs have more pixels ($N_{\rm pix}$) than bloomed αs. We used the variable $N_{\rm pix}\,\sigma_x/\sigma_y$ to separate plasma from bloomed αs (Figure 4.9).

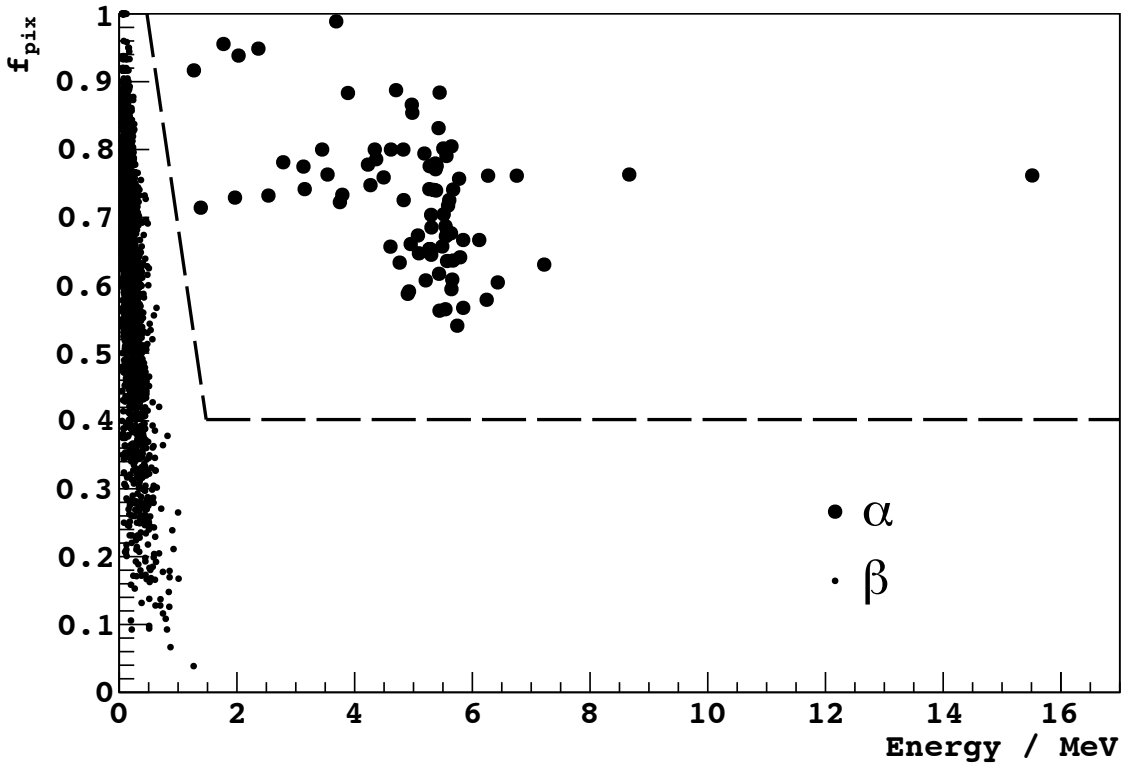

Figure 4.8: Selection of α particles. The fraction $f_{\rm pix}$ as a function of the cluster energy. Clusters in the region above the dashed line are selected as αs.

4.4.2 Limits on radioactive contamination from α analysis

The measured rate of αs in the three installed CCDs is reported in Table 4.4.

Most of the bloomed αs are clustered around the characteristic energy of ^{210}Po decay (5.3 MeV, Figure 4.9), which may be present as residual surface contamination following exposure to ^{222}RnȦlso, a significant number of αs have energies <4 MeV, lower than any αs from the ^{238}U and ^{232}Th chains (Figure 4.1). Most likely, these are α particles which lose some energy before reaching the active region of the device, and originate from surface contamination of the CCD or nearby materials. If we conservatively assume that all bloomed αs with energies <6 MeV are due to ^{210}Po decays from ^{210}Pb contamination on the front surface of the CCD, we obtain an activity of $0.078\pm0.010\,{\rm cm}^{-2}\,{\rm d}^{-1}$. This is twenty times

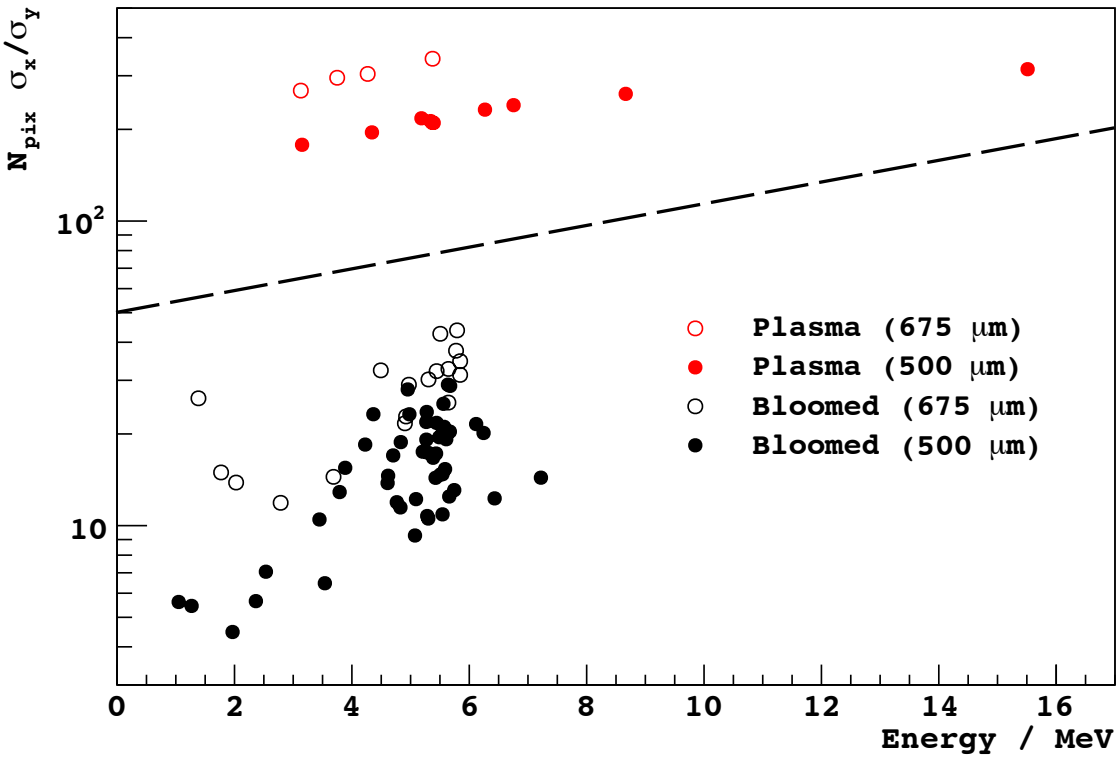

Figure 4.9: The variable $N_{\rm pix}\,\sigma_x/\sigma_y$ as a function of the α energy. Plasma (bloomed) αs are indicated by red (black) dots above (below) the dashed line. Open (closed) dots refer to clusters detected in the 675 μm (500 μm) -thick CCD. Clusters are more diffuse in the thicker CCD, resulting in larger $N_{\rm pix}$.

Table 4.4: CCD physical properties and rate of observed αs for the three CCDs installed at SNOLAB.

CCD	Mass / g	Area / cm^2	Bloomed rate / d^{-1}	Plasma rate / d^{-1}
500 μm top	2.2	19	0.87±0.17	0.21±0.09
500 μm bottom	2.2	19	0.87±0.17	0.14±0.07
675 μm	2.9	19	0.63±0.15	0.10±0.06
Average	2.4	19	0.79±0.10	0.15± 0.04

larger than the upper limit of -$3\times10^3\,cm^{-2}\,d^{-1}$ previously estimated from the exposure to ^{222}Rn during packaging. However, a significant number of the observed αs are likely to originate from the surfaces facing the CCD, i.e. the copper plates above the 675 μm and the top 500 μm CCD, and the silicon support piece above the bottom 500 μm CCD. Unfortunately, contributions from all these different surfaces cannot be disentangled with the available data. Similar considerations can be applied to plasma αs, which should release their full energy if occurring in the bulk. Many of the plasma αs have energies lower than those from ^{238}U and ^{232}Th chains, suggesting surface contamination. Taking again the conservative assumption that all plasma αs with energies <6 MeV originate from ^{210}Po back-surface contamination, we obtain an activity of $0.011\pm0.004\,cm^{-2}\,d^{-1}$.

Spectroscopy of plasma αs can be used to establish limits on ^{210}Pb , ^{238}U and ^{232}Th contamination in the bulk of the CCD. Four plasma αs whose energies are consistent with ^{210}Po were observed (Figure 4.9). One of them cannot be ^{210}Po, as it coincides spatially with two higher energy αs recorded in different CCD exposures, and is therefore likely part of a decay sequence (Section 4.4.3). When interpreting the other three as bulk contamination of ^{210}Po (or ^{210}Pb), an upper limit of $<37\,kg^{-1}\,d^{-1}$ (95% CL) is derived. In the ^{238}U chain, the isotopes ^{234}U, ^{230}Th and ^{226}Ra decay by emission of αs with energies 4.7–4.8 MeV (Figure 4.1). Since the isotopes' lifetimes are much longer than the CCD exposure time, their decays are expected to be uncorrelated. No plasma αs are observed in the 4.5–5.0 MeV energy range, and an upper limit on the ^{238}U contamination of $<5\,kg^{-1}\,d^{-1}$ or <4 ppt (95% CL) is correspondingly derived (secular equilibrium of the isotopes with ^{238}U was assumed). In the ^{232}Th chain, the timescale of the short-lived decay sequence of ^{224}Ra–^{220}Ra–^{216}Po is ∼1 min, which is much smaller than the CCD exposure time. Thus, such decay sequence would result in a single cluster when occurring in the bulk, with a total of 18.8 MeV of energy deposited by the pile-up of the three decays. No cluster with energy >16 MeV is observed, which results in an upper limit of $<15\,kg^{-1}\,d^{-1}$ or <43 ppt (95% CL) on ^{232}Th contamination

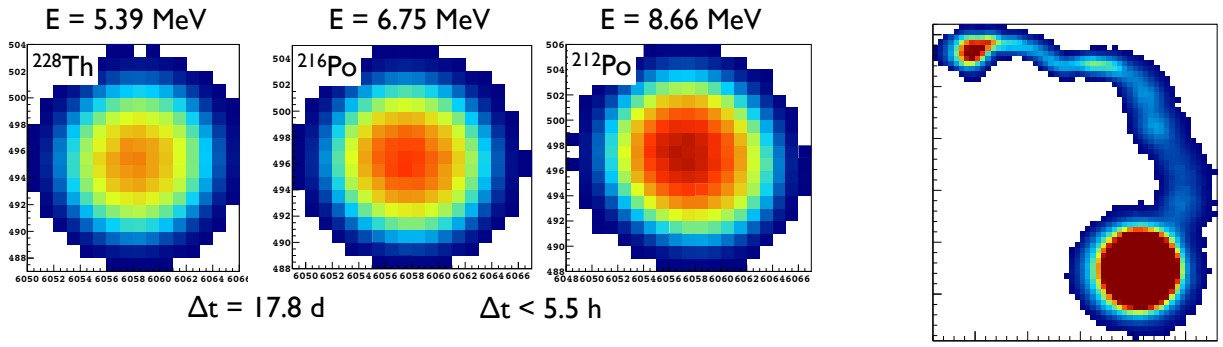

(a) Triple α sequence

(b) α–β coincidence

Figure 4.10: a) Three α particles detected in different CCD images at the same x-y position. Their energies and the time separation between images are consistent with a sequence from a ^{232}Th decay chain. b) A peculiar cluster found in a single image, consistent with a plasma α and a β track originating from the same CCD position. This may happen for a radioactive decay sequence occurring within the 8-hour exposure time of an image.

in the CCD bulk.

4.4.3 Observation of spatially correlated α decay sequences

We detected four plasma αs with energies >5.5 MeV (Figure 4.9), which cannot be accounted for by ^{210}Po decay. They all occur in the top 500-μm CCD. Two of them, along with an α close in energy to the ^{210}Po line, have their centroids within 1 pixel on the CCD x-y plane (Figure 4.10(a)). Since the accidental probability of this occurence is negligible, these three strongly spatially correlated events must have a common origin. A likely explanation is that we have observed a decay sequence starting with a ^{228}Th nucleus located in the thin (60 nm) ITO layer covering the backside of the CCD. The energies of the αs and the time separation between decays are consistent with those from the decays of ^{228}Th, ^{216}Po and ^{212}Po (Figure 4.1). The two other αs of the sequence, ^{224}Ra and ^{220}Rn, must have been emitted away from the CCD and thus gone undetected. Note that the recoiling nuclei corresponding to the ^{224}Ra and ^{220}Rn decays may penetrate the device, but their deposited energy would be too small to be observable on top of the ^{216}Po α once the detector resolution is considered. Likewise, the βs from ^{212}Pb and ^{212}Bi must have been emitted away from the CCD or have deposited <100–200 keV in the CCD. The observation of this single decay sequence is compatible with ∼100 ppb of ^{232}Th contamination in the ITO [36].

The highest energy plasma α (15.3 MeV) must be due to pile-up, either of two αs (e.g.

^{216}Po and ^{212}Po) or αs and βs with energies <100–200 keV (so that the beta track is too short to protrude outside of the α cluster). Likewise, the remaining 6.2 MeV α could be due to either a single α (e.g. ^{220}Ra) or a less energetic α piled-up with a <100-200 keV β. In either case, these decays are unlikely to have occurred in the bulk of the CCD, as there are no isolated decays or short sequences of decays ($\lesssim$hours) corresponding to these energies in the ^{238}U or ^{232}Th decay chains (Figure 4.1).

A spatial coincidence search between αs and βs is limited by the large number of accidentals from background, as the β rate is $\sim$100 times greater than the α rate in the low-gain data set. In one of the latter data sets we have observed a coincidence between an α and a β within the same exposure, shown in Figure 4.10(b). As the energy of the α cannot be measured due to digitizer saturation, this particular decay sequence cannot be identified.

4.5 Limits on ^{32}Si and ^{210}Pb contamination from β decay sequences

We have performed a search for decay sequences of two β tracks to identify radioactive contamination from ^{32}Si and ^{210}Pb and their daughters, whose β spectra extend to the lowest energies and could represent a significant background in the region of interest for the WIMP search. These isotopes do not emit α or penetrating γ radiation, and their decay rates are significant for extremely low atomic abundances due to their 10–100 y half-lives, making conventional screening methods ineffective in determining their presence at the low levels necessary for a WIMP search.

^{32}Si is produced by cosmic ray spallation of argon in the atmosphere, and then transported to the Earth's surface, mainly by rain and snow. Detector-grade silicon is obtained through a chemical process starting from natural silica. Therefore, the ^{32}Si content of a silicon detector should be close to its natural abundance in the raw silica. Spectral measurements of background radiation in silicon detectors suggest a rate of ^{32}Si at the level of 100s of decays per kg day [37]. ^{32}Si leads to the following decay sequence:

$$^{32}\mathrm{Si} \longrightarrow {}^{32}\mathrm{P} + \beta^- \text{ with } \tau_{1/2} = 150\,\mathrm{y},\ \mathrm{Q-value} = 227\,\mathrm{keV} \tag{4.3}$$

$$^{32}\mathrm{P} \longrightarrow {}^{32}\mathrm{S} + \beta^- \text{ with } \tau_{1/2} = 14\,\mathrm{d},\ \mathrm{Q-value} = 1.71\,\mathrm{MeV} \tag{4.4}$$

Table 4.5: Analyzed data sets. The background rate refers to electron-like tracks in the 675 μm-thick CCD.

Start date	End date	Live-time	Pixel integration time	Background rate
		day	μs	$g^{-1}\,d^{-1}$
2014/06/06	2014/07/07	28.7	0.6	45.9±0.7
2014/07/11	2014/08/21	36.1	40	5.1±0.2
2014/09/03	2014/09/29	20.7	40	4.8±0.3

^{210}Pb is a member of the ^{238}U decay chain (Figure 4.1) and is often found out of secular equilibrium, as chemical processes in the manufacture of materials separate it from other ^{238}U daughters. It may also remain as a long-term surface contaminant following exposure to environmental ^{222}Rn . ^{210}Pb leads to the following decay sequence:

$$^{210}\mathrm{Pb} \longrightarrow {}^{210}\mathrm{Bi} + \beta^- + \text{I.C. (80\%) / } \gamma \text{ (4\%) with } \tau_{1/2} = 22\,\mathrm{y},\ \mathrm{Q-value} = 63.5\,\mathrm{keV} \quad (4.5)$$

$$^{210}\mathrm{Bi} \longrightarrow {}^{210}\mathrm{Po} + \beta^- \text{ with } \tau_{1/2} = 5\,\mathrm{d},\ \mathrm{Q-value} = 1.16\,\mathrm{MeV} \quad (4.6)$$

The ^{210}Pb nucleus decays 84% of the time into an excited state of ^{210}Bi which promptly releases its 46.5 keV of energy by internal conversion of an atomic electron (I.C.) in 80% of the decays or by emission of a γ-ray in 4% of the decays. ^{210}Po is itself radioactive and decays by α emission. The possible contamination from ^{210}Po in the CCD has been discussed in Section 4.4.2.

The intermediate nuclei, ^{32}P and ^{210}Bi, are expected to remain in the same lattice site as their parent nuclei and throughout their lifetimes. Therefore, the βs produced by each decay pair should originate from the same pixel (out of 6×10^8) on the x-y plane of the CCD. Through a search for electron-like tracks starting from the same spatial position, individual ^{32}Si–^{32}P and ^{210}Pb–^{210}Bi decay sequences can be selected with high efficiency. We performed this search with the lowest background data set (Table 4.5) in the 675 μm CCD. Given the background level ($\sim$10 electrons per day in a CCD), the number of accidental coincidences among uncorrelated tracks are small for periods of time comparable to the half-lives of ^{32}P and ^{210}Bi. A candidate decay sequence found in the data is shown in Figure 4.11 to illustrate the search strategy.

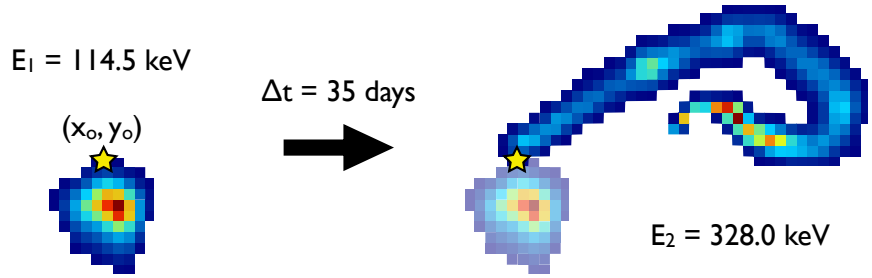

Figure 4.11: Candidate β decay sequence found in data. The first cluster was detected in an image taken on 2014/08/05 and deposited 114.5 keV of energy. A second cluster, with energy 328.0 keV, was observed in an image taken 35 days later. Both tracks appear to originate from the same point (yellow star) in the CCD x-y plane.

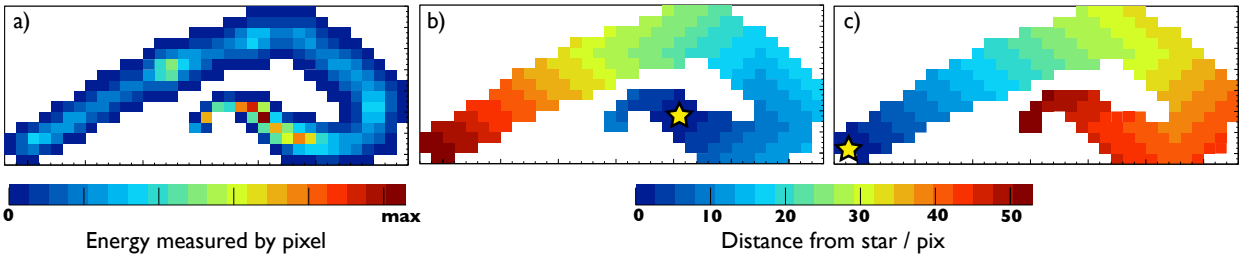

Figure 4.12: Algorithm to find the end-points of a cluster. a) The pixel with maximum signal is chosen as seed point. b) The distance of each pixel in the cluster to the seed point (star) is computed. c) The pixel with the largest distance is chosen as the first end-point (star). Distances to the first end-point are calculated, and the pixel with the largest distance is taken as the second end-point (the reddest pixel).

4.5.1 Search procedures for spatially-correlated β decay sequences

The first step in the search for decay sequences is to find the end-points of the β tracks. The procedure is illustrated in Figure 4.12. First, we find the pixel with the maximum signal in the cluster, and we use it as a seed point. Then, for every pixel of the cluster we compute the length of the shortest path to the seed point, where the path is taken only along pixels that are included in the cluster. We refer to this as the "distance" from the seed point. The pixel with the greatest distance is taken as the first end-point of the track. Finally, we recompute the distance of every pixel from the first end-point, and take the pixel with the largest distance as the second end-point of the cluster.

To find a β decay sequence, we calculate the distance from the end-points of every β cluster in an image to the end-points of every β cluster in later images. Thus, for every

pair of clusters we have four distances corresponding to each end-point combination. The minimum of these distances is defined as the "cluster distance". The pair is considered a candidate for a decay sequence if the cluster distance is smaller than 20 pixels and the clusters have at least one pixel in common. We refer to the cluster in the earlier (later) image as the "first" ("second") cluster.

To reduce the number of accidental pairs, we impose additional criteria on the energy of the clusters and their time separation. For the ^{32}Si–^{32}P sequence search, we require the energy of the first cluster to be <230 keV and the energy of the second cluster to be <1.8 MeV. For the ^{210}Pb–^{210}Bi sequence search, we require the energy of the first cluster to be in the range 30–65 keV, which mostly includes the 80% of decays with an electron from internal conversion (Eq. 4.5). Clusters from I.C. will be diffusion limited, as they will be constituted by a cascade of β, conversion and Auger electrons with energies <30 keV. The energy of the second cluster is restricted to be <1.2 MeV.

Lastly, we require the time separation between the clusters of each pair, $\Delta t_{\rm pair}$, to be less than five half-lives of the daughter nuclei. This corresponds to 70 (25) days for the ^{32}Si–^{32}P (^{210}Pb–^{210}Bi) decay sequence search.

4.5.2 Pair selection efficiency

The efficiency of the pair selection described in Section 4.5.1 was estimated with Monte Carlo simulations. We used the MCNPX5 [38] program with full electron tracking to simulate β particle interactions in a rectangular block of silicon with the same dimensions of a DAMIC CCD. The energy deposited by a particle is recorded in a mesh with cells of the size of a CCD pixel. The average z-coordinate of the simulated particle track within each cell is also recorded. Then, a realistic resolution and diffusion model is applied to the number of ionized charge carriers from the position at which they were produced along the electron's path, and a simulated pixel cluster on the x-y plane of the CCD is obtained. For the purpose of the decay sequence search, the origin of the β particle was randomly generated in the silicon volume of the CCD to simulate a decay occurring in the bulk.

To properly include the measured readout noise in the analysis, we used data "blanks". These are zero-length exposures read out immediately after every data exposure, which feature true readout noise patterns but no physical tracks. There are 159 blanks taken during the decay sequence search period. In each of them, we introduced the simulated clusters of

five βs from ^{32}Si to approximately reproduce the rate of electron-like tracks measured in data. For each simulated ^{32}Si decay, a ^{32}P decay was generated from the same location in a later image, distributed in time according to the half-life of ^{32}P. With this method, 496 decay pairs were introduced in the sample of blank images. We used the standard CCD image reduction (Section 3) to reconstruct clusters. To properly account for inefficiencies of the CCD, bad pixels found in data were also masked in the blanks. Then, the pair selection procedure was applied to this set of simulated images. We found 504 candidate pairs ($N_{\rm pairs}$) with a cluster distance distribution shown in Figure 4.13. As most of the pairs have a cluster distance <7 pixels, we adopt this additional criterion for the pair selection.

First, we estimated the efficiency $\epsilon_{\rm pair}$ of requiring a cluster distance <7 pixels and cluster energies consistent with a ^{32}Si–^{32}P decay sequence (Section 4.5.1). Of the 486 pairs with cluster distance <7 pixels, 475 are true pairs. Thus, the pair selection procedure is highly efficient in recovering decay sequences ($\epsilon_{\rm pair}$=475/496=95.8%), while keeping background at a reasonable level. The inefficiency is mostly due to pairs for which one or both tracks were not properly reconstructed due to masked pixels (16 out of 21 lost pairs).

Secondly, we determined the efficiency $\epsilon_{\rm time}$ to select a ^{32}Si–^{32}P decay sequence with pairs separated in time by less than 70 days (see Section 4.5.1) and occurring during the live-time of our data set (a decay sequence will not be found if the CCD was not operational when a decay occurred). In Figure 4.14, the probability for a ^{32}P decay to be selected within the live-time of the data taking period is calculated as a function of the parent ^{32}Si decay time. Integrated over the live-time of the data set, this gives an average $\epsilon_{\rm time}$ =51.3%.

An analogous simulation study was performed for the ^{210}Pb–^{210}Bi decay sequence. In this case, $\epsilon_{\rm pair}$ is mainly determined by the requirement on the energy of the first cluster to be in the range 30–65 keV (see Section 4.5.1). To estimate this efficiency, we have considered all possible processes following ^{210}Pb decay, including the cases where some of the energy is radiated in γ-rays or X-rays that escape the decay site and will not form part of the cluster. Only 82% of ^{210}Pb decays fall in this energy range. Of those, about 7.4% are not selected because their measured cluster energy is <30 keV due to pixel saturation. The corresponding pair selection efficiency is found to be $\epsilon_{\rm pair}$ = 71.0%. Also, an average $\epsilon_{\rm time}$ =65.1% is obtained for this decay sequence.

The overall efficiency for detection of ^{32}Si–^{32}P (^{210}Pb–^{210}Bi) decay sequences in our data set, $\epsilon_{\rm X}$=$\epsilon_{\rm pair}\epsilon_{\rm time}$, where X = Si and Pb, is determined to be $\epsilon_{\rm Si}$=49.2% ($\epsilon_{\rm Pb}$=46.2%).

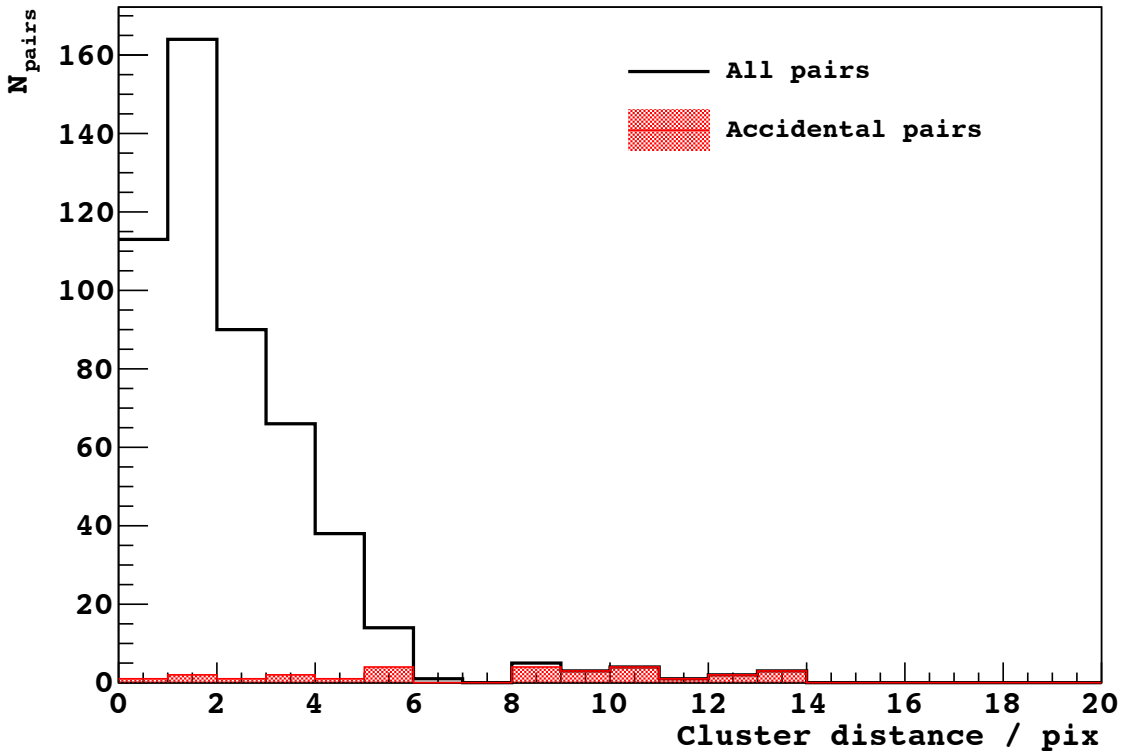

Figure 4.13: Cluster distance distribution (black histogram) for the ^{32}Si–^{32}P candidate pairs found in the simulated sample. Accidental pairs are represented by the red shaded histogram.

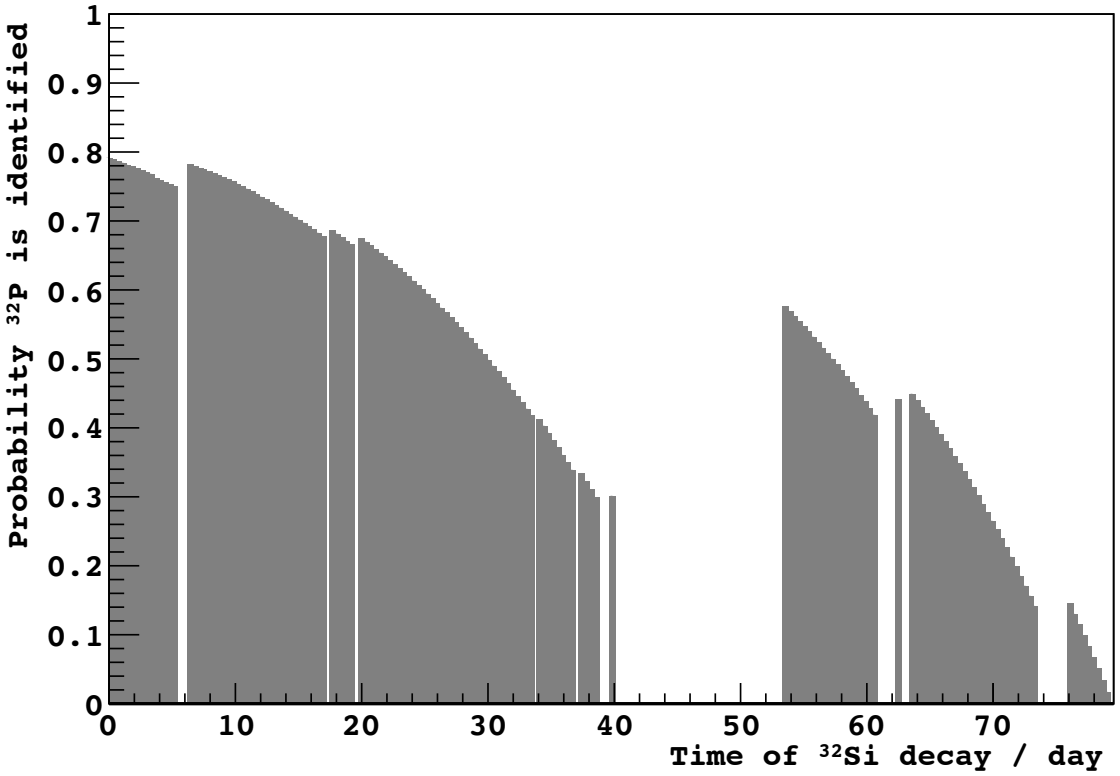

Figure 4.14: Probability for the ^{32}P decay to be selected within the live-time of the data taking period, as a function of the parent ^{32}Si decay time. The probability is zero when data was not acquired.

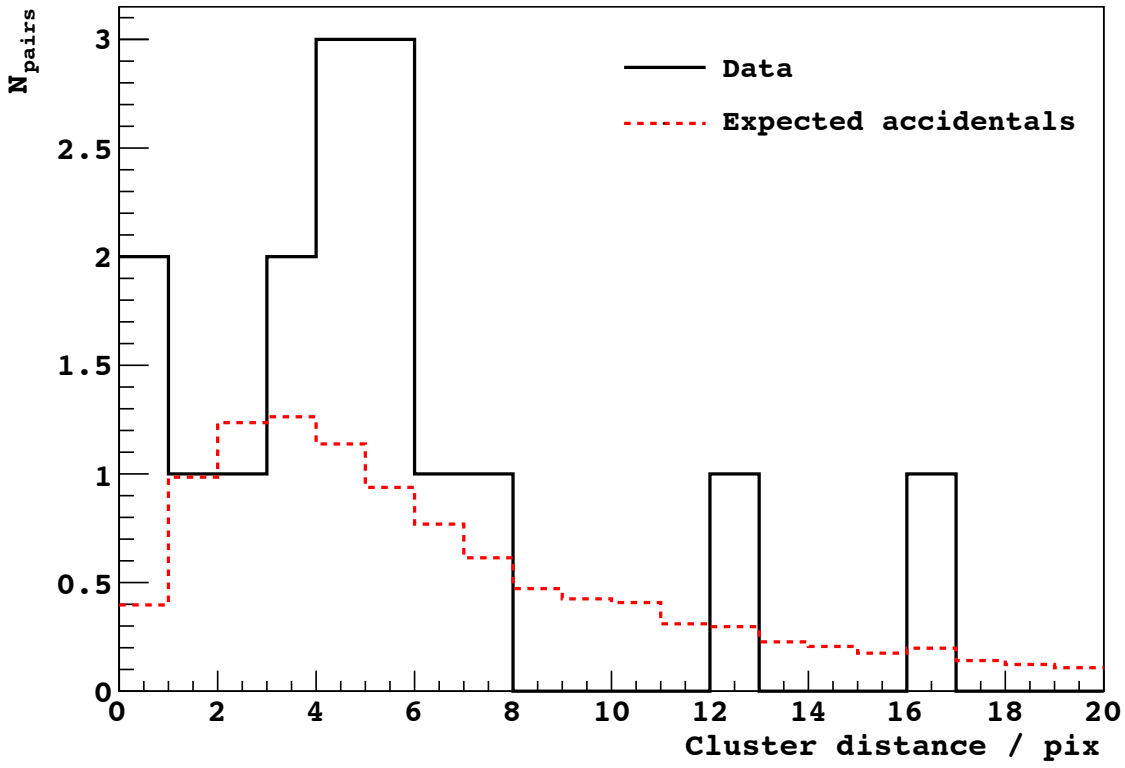

Figure 4.15: Cluster distance distribution for the 16 ^{32}Si–^{32}P candidate pairs found in 56.8 days of data.

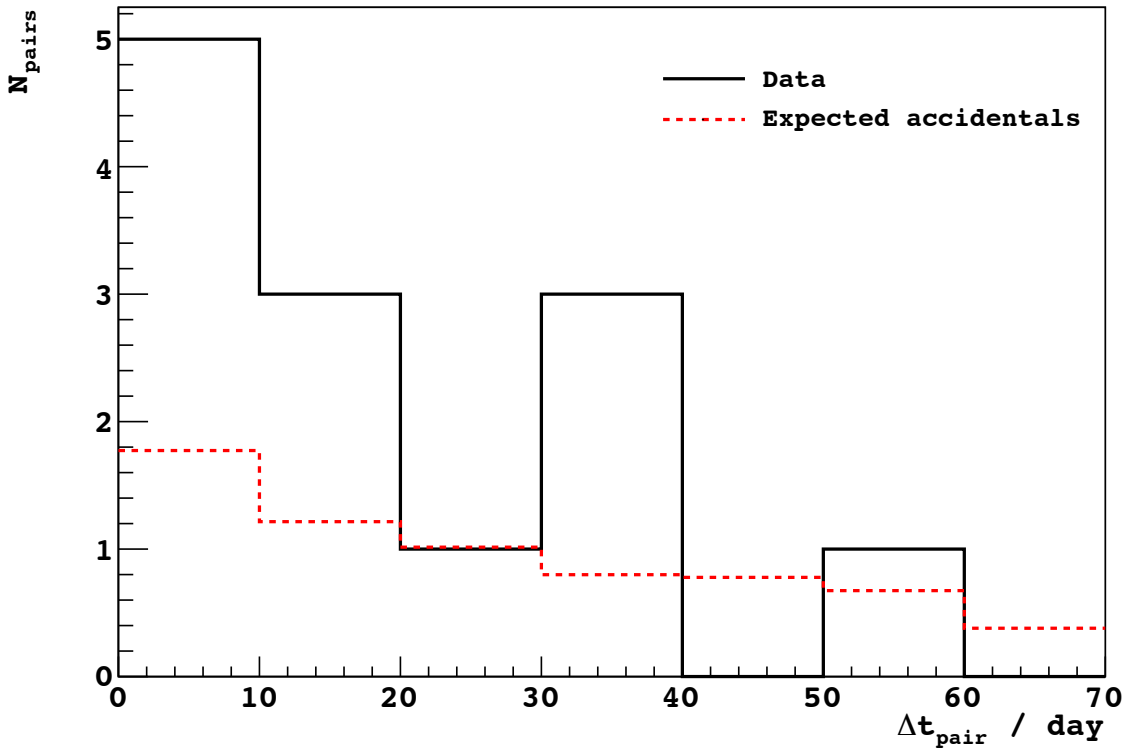

Figure 4.16: Distribution of the time separation Δt_{pair} of the 13 pairs with cluster distance <7 pixels. The red dashed line is the expectation for accidental pairs.

4.5.3 Limits on ^{32}Si and ^{210}Pb contamination

The search procedure described in Section 4.5.1 was applied to the data. No candidate was found in the ^{210}Pb–^{210}Bi search. The ^{32}Si–^{32}P decay sequence criteria yielded 16 candidate pairs, 13 of which have a cluster distance <7 pixels (Figure 4.15). The Δt_{pair} distribution of these 13 pairs is shown in Figure 4.16. Also shown are the corresponding distributions expected for purely accidental pairs, which were estimated directly from the data. For this purpose, we randomized the position of the clusters in all data images, effectively eliminating any spatial correlation between βs from decay sequences potentially present in the data. In the randomization process, the overall x-y distribution of the clusters was maintained to avoid introducing a bias. Accidental pairs were then found in the set of randomized images by applying the search criteria. The procedure was repeated one thousand times, obtaining for each randomized search the accidental pairs distribution of cluster distance and Δt_{pair}. The average of the one thousand distributions (red dashed line) is shown in Figs. 4.15-4.16. Within the limited statistics, an excess of pairs is observed in data. Also, the Δt_{pair} distribution is compatible with the 14 days half-life of ^{32}P.

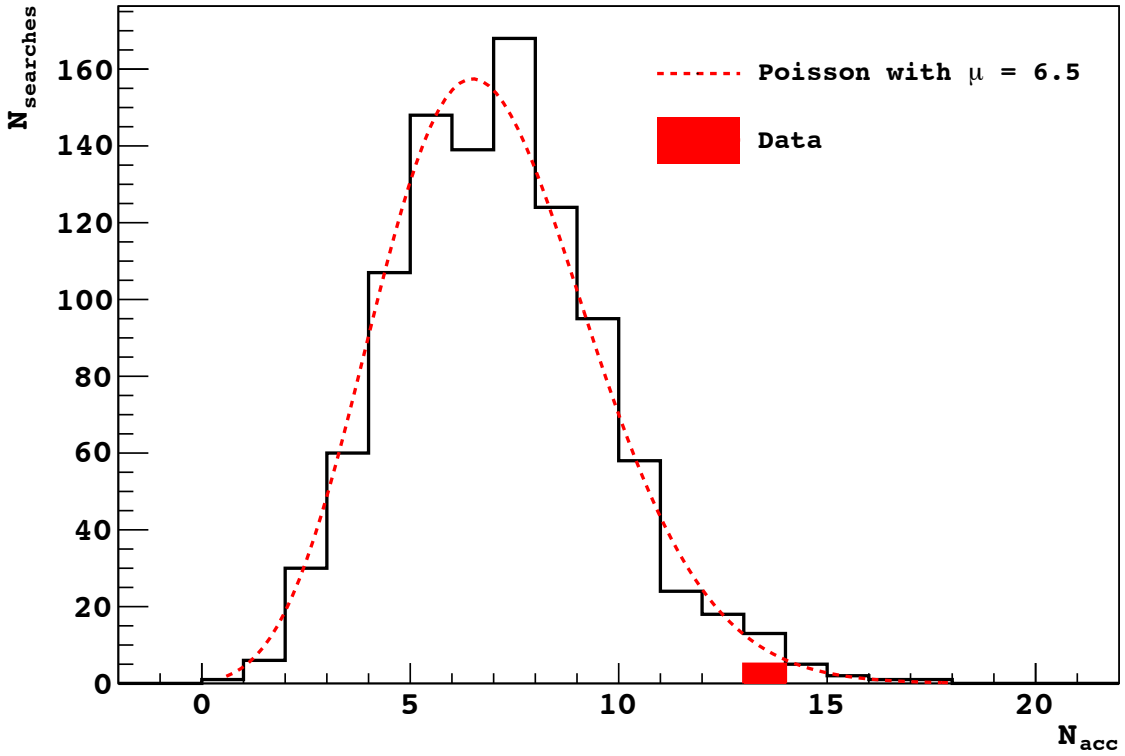

Figure 4.17: Distribution of the number of accidental pairs with cluster distance <7 pixels for the ^{32}Si–^{32}P decay sequences. The distributions were obtained by performing 1000 searches over spatially randomized data images. The blue-dashed line is the Poisson distribution corresponding to the mean of the histogram. The red entry is the number of candidate pairs found in data.

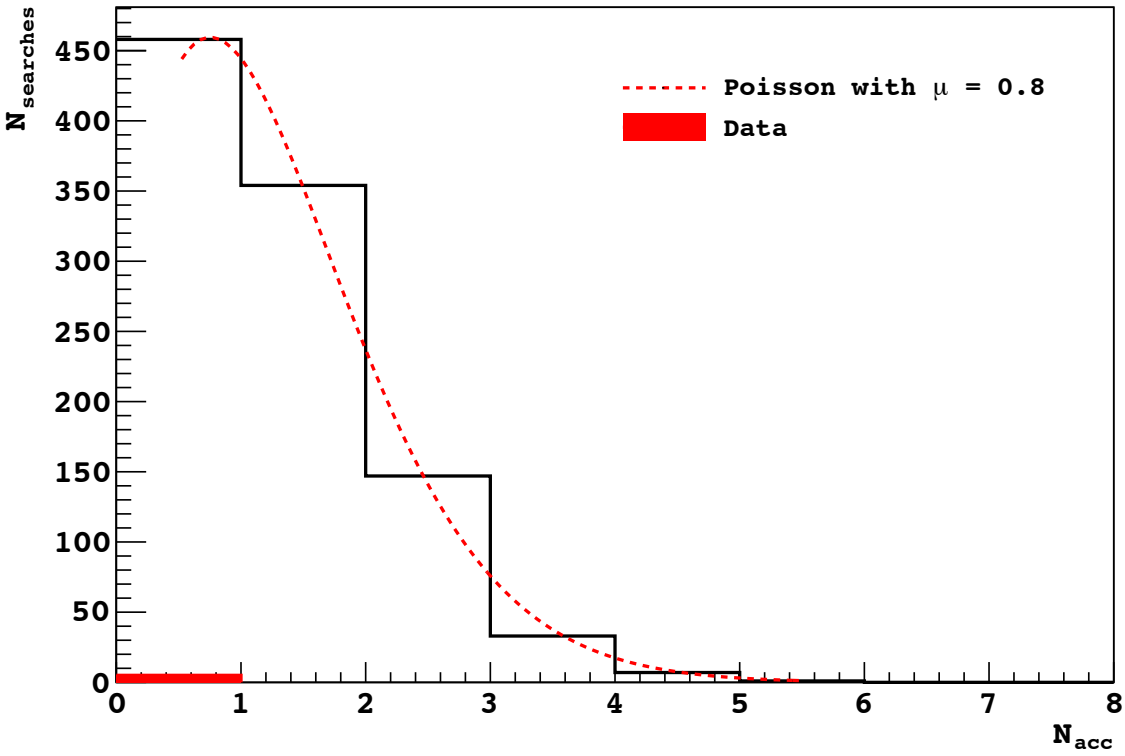

Figure 4.18: Distribution of the number of accidental pairs with cluster distance <7 pixels for the ^{210}Pb–^{210}Bi decay sequences. The distributions were obtained by performing 1000 searches over spatially randomized data images. The blue-dashed line is the Poisson distribution corresponding to the mean of the histogram. The red entry is the number of candidate pairs found in data.

Table 4.6: Summary of results presented in this paper. All values are 95% C.L. upper limits or intervals, except for the ^{210}Po surface rate, where the uncertainties are 1-σ. The two measurements of the ^{210}Po surface rate correspond to the two (back, front) CCD surfaces. For ^{238}U and ^{232}Th we quote the corresponding ppt contamination in parenthesis.

Analysis method	Isotope(s)	Tracer for	Bulk rate $\mathrm{kg^{-1}\,d^{-1}}$	Surface rate $\mathrm{cm^{-2}\,d^{-1}}$
α spectroscopy	^{210}Po	^{210}Pb	<37	0.011±0.004, 0.078±0.010
	^{234}U + ^{230}Th + ^{220}Ra	^{238}U	<5 (4 ppt)	–
	^{224}Ra–^{220}Ra–^{216}Po	^{232}Th	<15 (43 ppt)	–
β spatial coincidence	^{32}Si–^{32}P	^{32}Si	80^{+110}_{-65}	–
	^{210}Pb–^{210}Bi	^{210}Pb	<33	–

To evaluate the significance of the excess in the ^{32}Si–^{32}P search and establish a limit on ^{210}Pb contamination, the probability distribution of the number of accidental pairs, P_{acc}, was determined with the same spatial randomization procedure described above. For each randomized search, the number of accidental pairs with cluster distance <7 pixels, N_{acc}, was obtained. A N_{acc} distribution was derived from one thousand randomized searches, and taken as an estimate of P_{acc}. We verified with Monte Carlo simulations that the true P_{acc} is indeed recovered by this procedure. Figure **??** shows the N_{acc} distributions obtained for the ^{32}Si–^{32}P and ^{210}Pb–^{210}Bi decay sequence searches. These distributions are well represented by Poisson distributions of mean 6.5 for the ^{32}Si–^{32}P search, and mean 0.8 for the ^{210}Pb–^{210}Bi search. With this assumption, the 13 observed candidate pairs correspond to $1.2<N_{\mathrm{Si}}<15.3$ (95% C.L.) [39], where N_{Si} is the number of estimated ^{32}Si–^{32}P decay sequences in the data. The null result for the ^{210}Pb–^{210}Bi search corresponds to $N_{\mathrm{Pb}}<2.5$ (95% C.L.) [39], where N_{Pb} is the number of estimated decay sequences in the data.

The ^{32}Si and ^{210}Pb decay rates are then obtained from the ratio $N_{\mathrm{X}}/\epsilon_{\mathrm{X}}/\mathrm{T}/\mathrm{M_{CCD}}$, with ϵ_{X} as given in Section 4.5.2, T=56.8 d is the data live-time and $\mathrm{M_{CCD}} = 2.9 \cdot 10^{-3}$ kg. We estimate a decay rate of $80^{+110}_{-65}\,\mathrm{kg^{-1}\,d^{-1}}$ (95% C.L.) for ^{32}Si in the CCD bulk. This result also establish the detection of ^{32}Si–^{32}P pairs in our data set at 98% C.L.. The derived upper limit on the ^{210}Pb decay rate in the CCD bulk is $<33\,\mathrm{kg^{-1}\,d^{-1}}$ (95% C.L.).

CHAPTER 5
NEUTRON CALIBRATION

5.1 Ionization Efficiency and the Lindhard Theory

As described previously, a WIMP can elastically scatter with a silicon nucleus in the CCD, producing a nuclear recoil. However, not all of the nuclear recoil energy is spent on ejecting electrons from silicon atoms, i.e. ionization. The remaining energy is assumed to be transferred to atomic motion. The fraction of nuclear recoil energy spent on ionizing silicon atoms, defined as the ionization efficiency f, is described by the Lindhard theory [40]. Using first-order perturbation theory and random phase approximation, the Lindhard theory calculates the effects of electrons screening the electric field in a solid. The recoiled atom with energy $E_{\rm nr}$ undergoes a cascade of collisions while slowing down, and the competition between electronic and nuclear cross-sections determines the partitioning between the energy used to ionize silicon atoms and that transferred to atomic motion. The average of the latter is obtained by integrating over all possible partitioning,

$$k\epsilon^{1/2}f(\epsilon) = \int_0^{\epsilon^2} \frac{dt}{2t^{3/2}} f(t^{1/2})[f'(\epsilon - \frac{t}{\epsilon}) - f'(\epsilon) + f'(\epsilon + \frac{t}{\epsilon}), \tag{5.1}$$

where

$$\epsilon = E\frac{a}{2Z^2e^2} \tag{5.2}$$

is the dimensionless reduced energy, $f(\epsilon)$ the ionization efficiency, $k = 0.133Z^{2/3}A^{-1/2}$, and $t = \epsilon^2 \sin^2(\Theta/2)$ with Θ being the scattering angle in the center-of-mass frame [41]. Analytical solutions are only possible for unrealistic atomic potentials. Numerical solutions for the Lindhard theory can be written as

$$f = \frac{kg(\epsilon)}{1 + kg(\epsilon)} \tag{5.3}$$

with

$$g(\epsilon) = 3\epsilon^{0.15} + 0.7\epsilon^{0.6} + \epsilon. \tag{5.4}$$

However, no measurement for silicon exists for electron recoil energy below a few keV, which is the region of interest for DAMIC. We use a monochromatic neutron beam as source particles to measure the ionization efficiency in the energy range of interest for DAMIC. With the DAMIC type CCD facing the neutron source, neutrons elastically scatter with silicon nuclei in a way similar to interactions with WIMPs. The electron recoil energy spectrum ($E_{\rm ee}$) is measured by the CCD while the nuclear recoil spectrum ($E_{\rm nr}$) is obtained from simulations using MCNP. Finally, the ionization efficiency is extracted by mapping $E_{\rm ee}$ to $E_{\rm nr}$.

5.2 Neutron Calibration Setup

The setup of the neutron calibration is shown in Figure 5.1. The whole system contains the CCD chamber, data acquisition system, cooling and vacuum system, and the lead castle with the source inside. The chamber is 6-inch by 6-inch made of stainless steel with two nipples on the left and right sides connecting the CCD to the cold head and the readout cables, respectively. The vacuum in the chamber is maintained by a turbo pump. A temperature sensor and a heater are mounted in the cold tip inside the chamber to keep the temperature at 128K while exposing and reading out the CCD. As discussed in Chapter 2, this temperature lowers the dark current and reduces noise.

We use a CCD 500 μm thick with 2k $\times$ 4k pixels packaged in a silicon support and a copper holder frame to measure the electron recoil spectrum, as shown in Figure 5.2.

The neutron source containing activated Sb and BeO is located about 30 cm away from the CCD in the lead castle, shown in Figure 5.3. Natural Sb contains 57.36% ^{121}Sb and ^{123}Sb. The latter can be activated in a nuclear reactor to the unstable ^{124}Sb with a half-life of 60 days, undergoing beta decays with Q-value = 2.9 MeV and emitting a few γ lines. Among them, the 1.69 MeV γ ray interacts with Be through photonuclear reaction (γ,n), and produces 23.5 keV monochromatic neutron with a branching ratio of about 47.8%. The lead castle stops most of the high energy γ rays from ^{124}Sb. We also build aluminum pieces with dimensions the same as those of BeO pieces to measure background from environment and γ rays from ^{124}Sb. The Sb source was activated on Jan 7th, 2015 with a measured intensity of 5.32 mCi +/- 5% . We could replace any of the three parts with Al pieces with the same dimensions for different configurations of data taking or for background measurement.

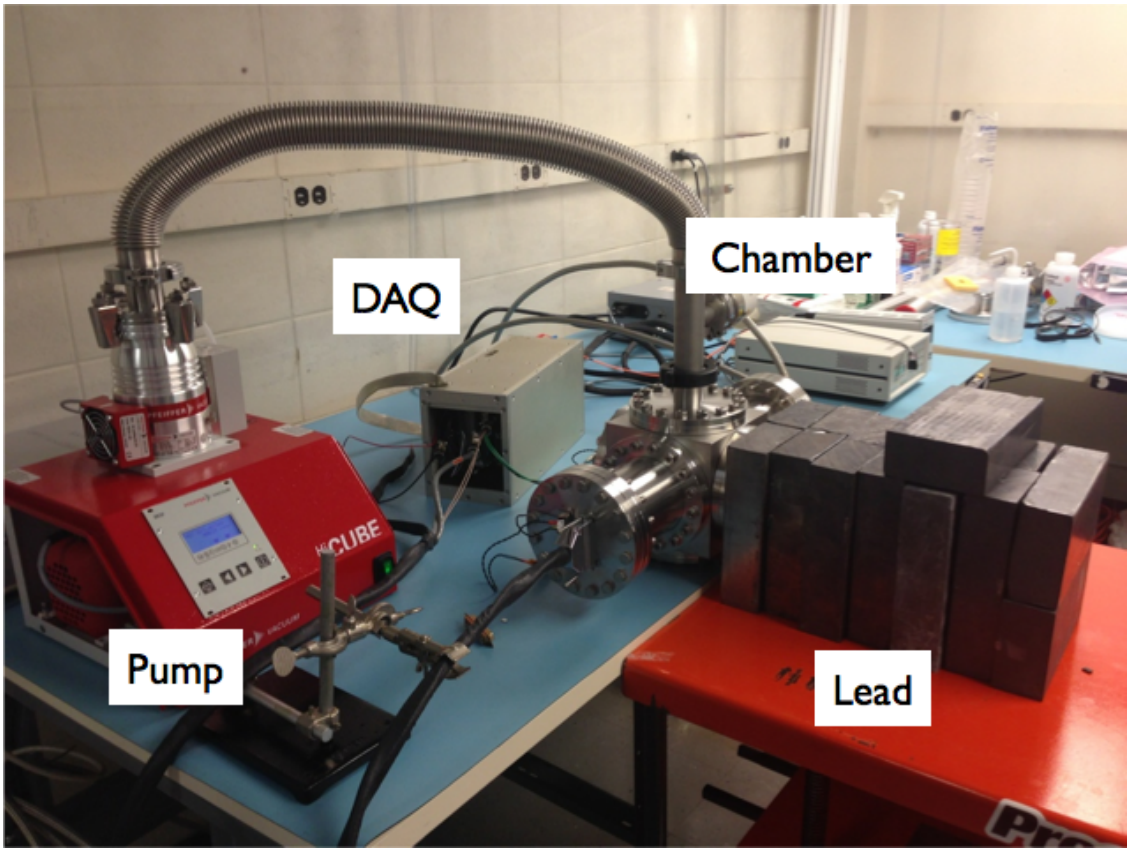

Figure 5.1: The whole system containing the CCD chamber, the data acquisition system, the cooling and vacuum system, and the lead castle with the source inside. The chamber is 6-inch by 6-inch made of stainless steel with two nipples on the left and right sides connecting the CCD to the cold head and the readout cables, respectively.

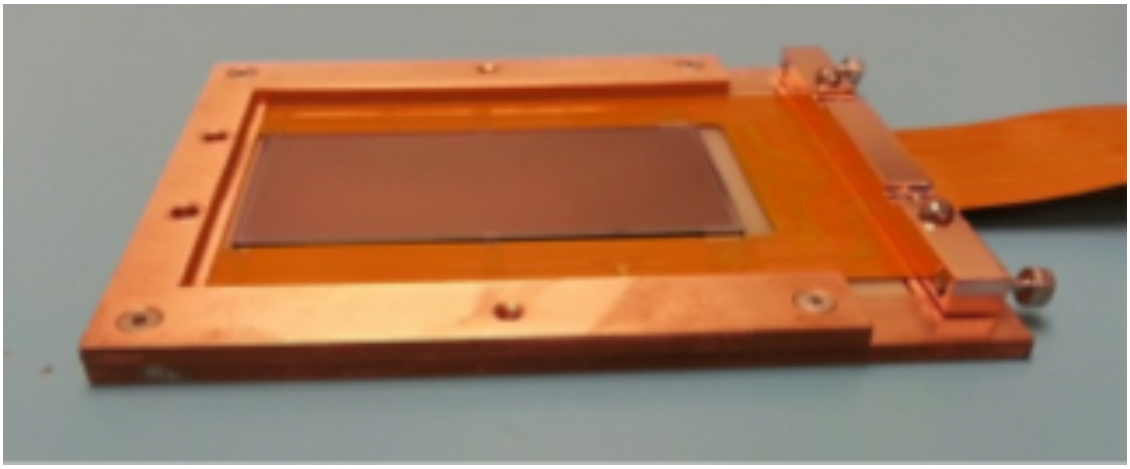

Figure 5.2: We use a CCD 500 μm thick with 2k $\times$ 4k pixels packaged in a silicon support and a copper holder frame to measure the electron recoil spectrum.

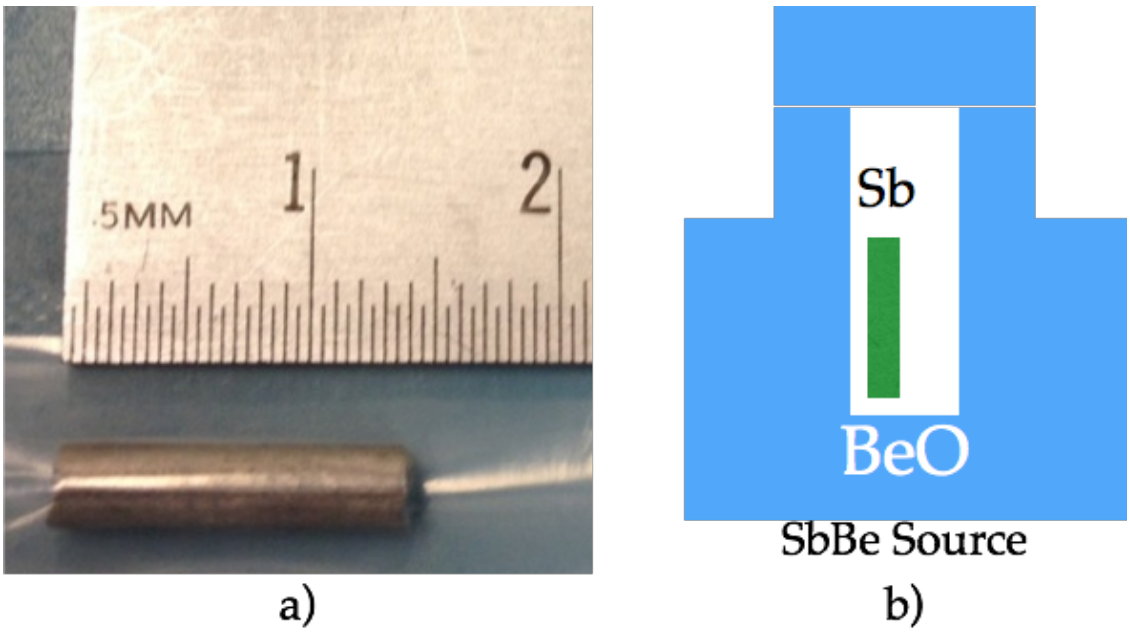

Figure 5.3: a) The Sb cylinder, activated on Jan 7th, 2015 with a measured intensity of 5.32 mCi. b) Geometry of the source illustrating the Sb source located inside the BeO castle.

5.3 Simulation of the Calibration

We do Monte Carlo simulations to get the nuclear recoil spectrum in the CCD with MCNPX-polimi. The definition of the geometry from the side is shown in Figure 5.4, where the green part is the stainless steel chamber with two nipples on the sides. Details of the CCD package and the source are also included in the simulations. We turn on photonuclear interactions in the MCNPX-polimi in order to get the correct energy and directional distribution of neutrons from BeO, shown in Figure 5.5 which clearly demonstrates monochromatic neutrons peaking at 23.5 keV in the spectrum. The tail in the lower energy range in the spectrum is due to neutron moderation by BeO. The cross-section of ^{9}Be(γ, n) at 1.69 MeV is 1.64 mbar from xxxx measurement in Figure 5.6. It shows that the efficiency of neutron production with 135.8g of BeO is 1.47e-4 in the simulations.

The neutrons go through the stainless steel flange with a thinkness of 9/16" after propagating in the lead. We use a ^{3}He detector to measure the neutron fluxes around the lead castle and around the CCD chamber to test the neutron propagation in the lead and the ^{9}Be(γ, n) photonuclear cross-section in the simulations, shown in Figure 5.7. ^{3}He reacts by absorbing thermal neutrons, producing a ^{1}H and a ^{3}H ion. Its sensitivity to γ rays is negligible, and therefore providing a very useful neutron detector. In order to moderate

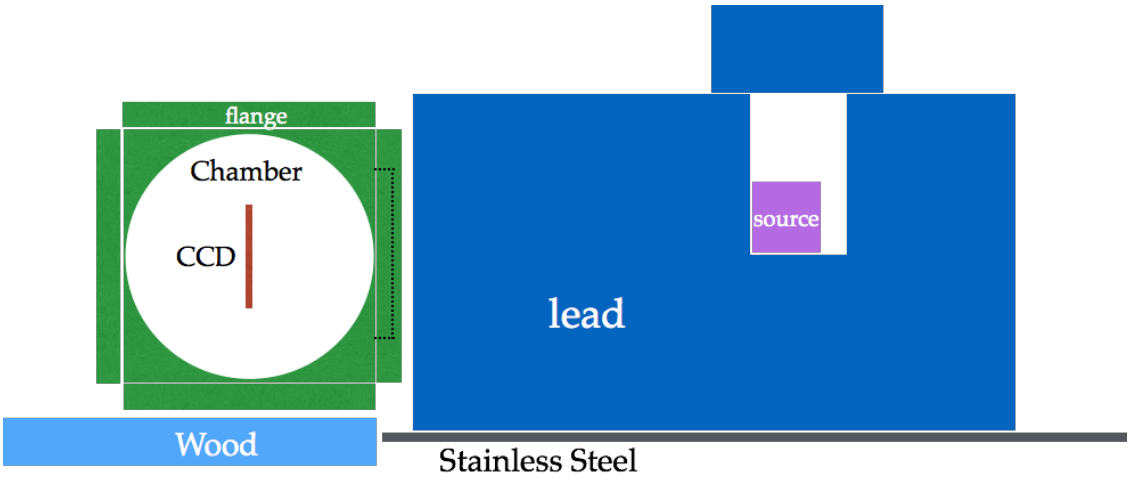

Figure 5.4: Setup geometry defined in the MCNP simulations viewed from the side.

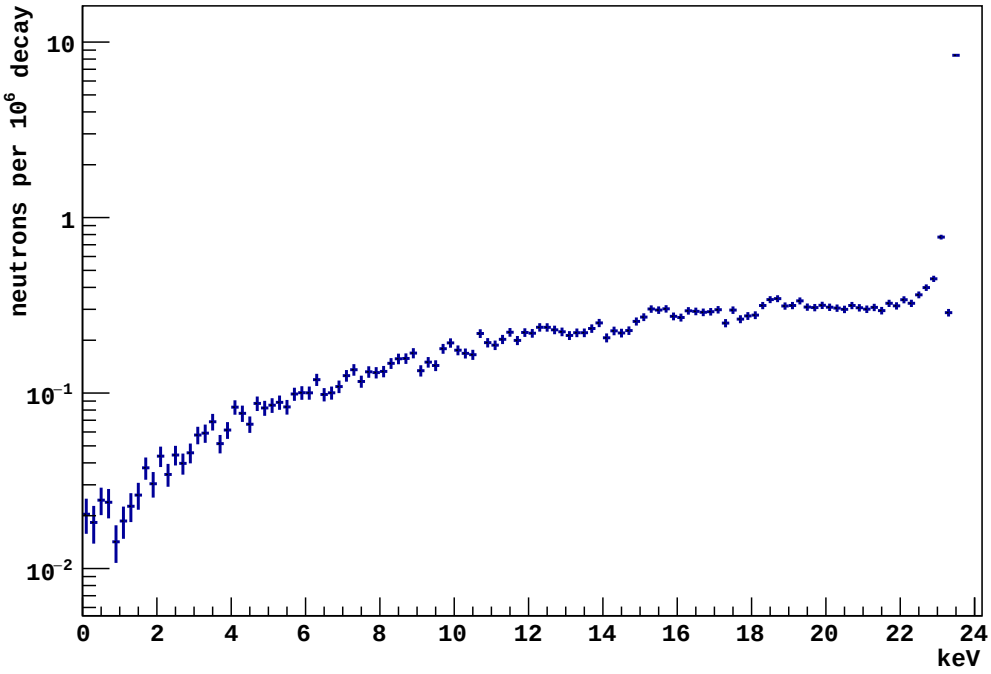

Figure 5.5: Neutron flux spectrum from BeO with a peak at 23.5 keV.

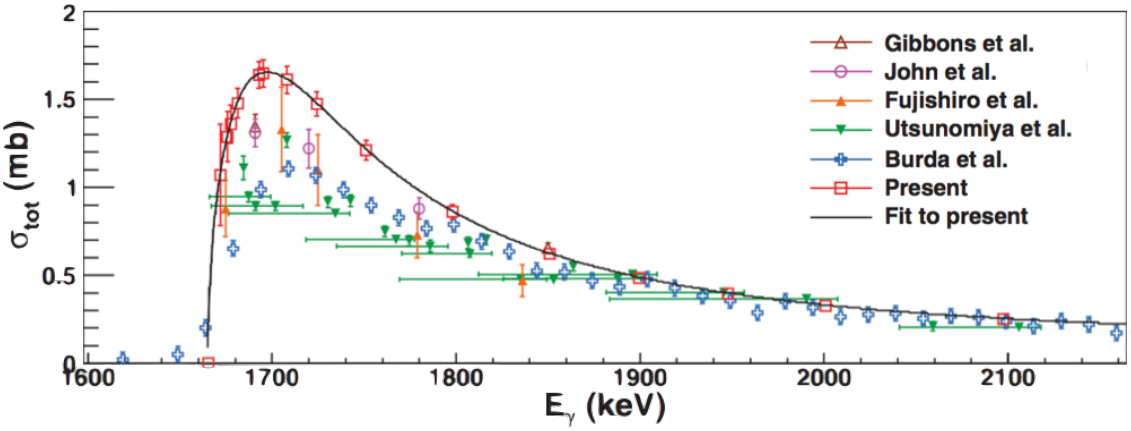

Figure 5.6: Measurement of ^{9}Be photonuclear (γ, n) cross-section. The most recent measurement determines the cross-section to be 1.64 mbar at 1.69 MeV.

neutrons from BeSb to thermal neutrons, we put a polyethylene cylinder 1-inch thick around the ^{3}He detector. Figure 5.8 shows the flux of neutrons before reaching polyethylene that are actually captured by ^{3}He which demonstrates that the detector with polyethylene is sensitive to neutrons peaked at energy $\sim$ 23 keV. We put a 6mm cadmium foil around the ^{3}He detector to absorb thermal neutrons in order to decrease their influences. Natural cadmium contains 12.22 % ^{113}Cd with a cross-section of 10^{4} barn in the thermal energy range. Historical measurements with the ^{3}He detector show a 10% uncertainty.

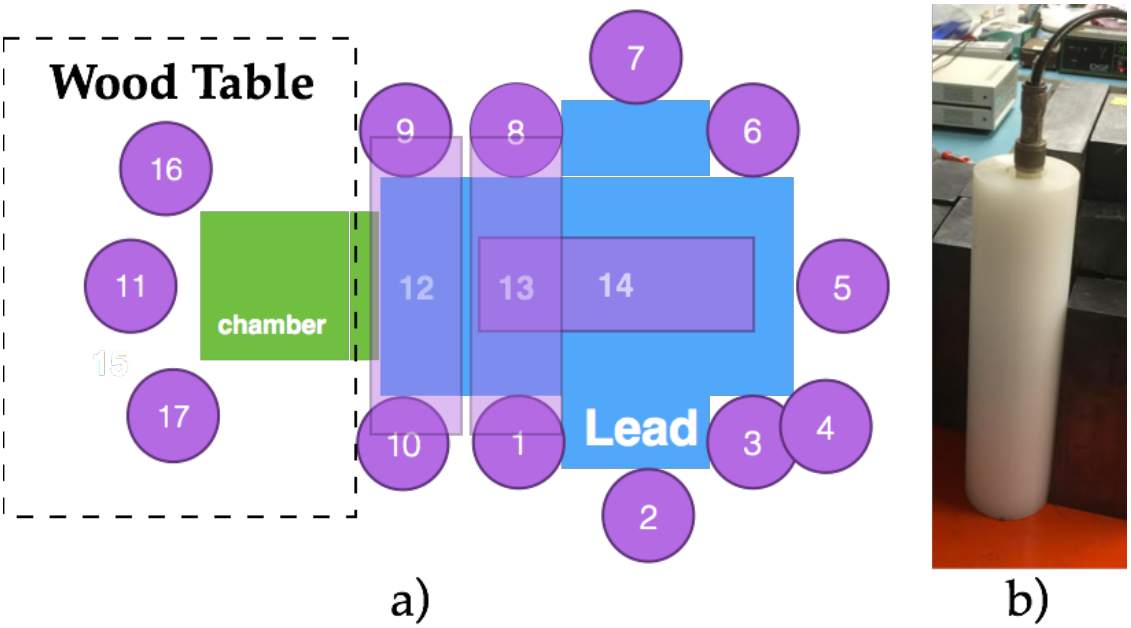

Figure 5.7: Setup of the ^{3}He detector. a) Viewed from above where circles show measurement locations. b)^{3}He detector with polyethylene wrapped around.

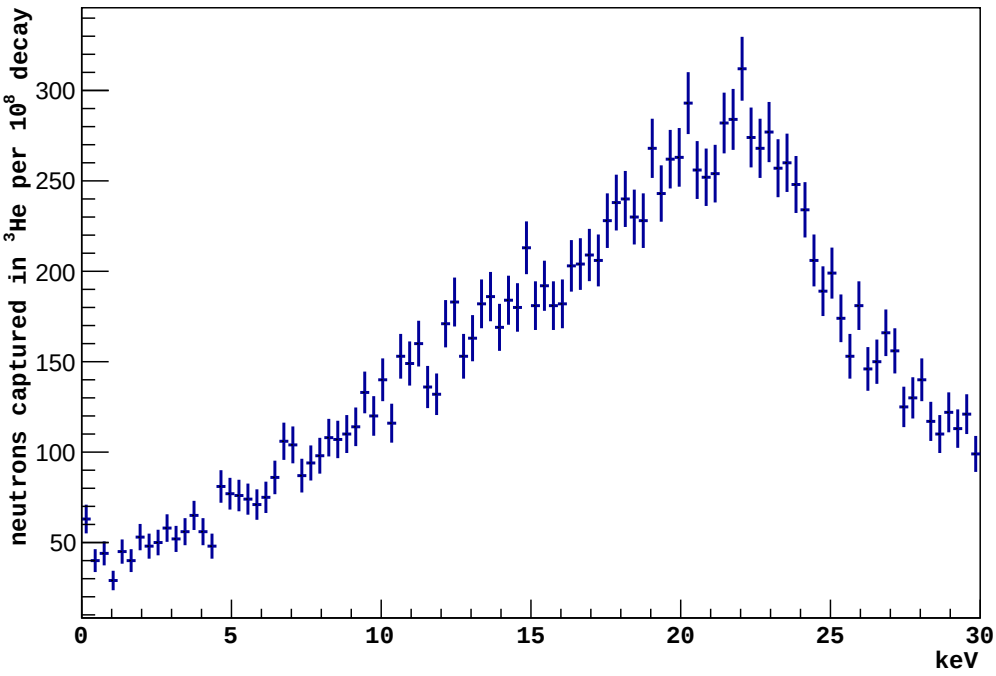

Figure 5.8: Flux of neutrons before reaching polyethylene that are actually captured by ^{3}He which demonstrates that the detector with polyethylene is sensitive to neutrons peaked at energy $\sim$ 23 keV.

Position	measurement(n/s)	simulation (n/s)	sim/mea
8	14.81	17.85	1.20
9	4.00	4.90	1.24
10	4.01	4.92	1.23
11	0.45	0.55	1.21
12	3.95	4.96	1.25
16	0.7	0.75	1.08
17	0.65	0.7	1.08

Table 5.1: Measurements and simulations of neutron flux with the ^{3}He detector around the chamber.

Figure 5.7 shows 17 measurement positions with the ^{3}He detector. The spectrum from ^{3}He is shown in Figure 5.9. Table 5.1 presents the result, where column 1 is the position number, column 2 the measurement with the ^{3}He detector in units of neutrons per second (n/s), column 3 the neutron flux from simulations with MCNP in the same units, column 4 the ratio between simulations and measurements, indicating an average simulation-over-measurement ratio of 1.18+/- 0.07. This means that the cross-section we use in the simulation should be scaled down to 1.64/1.18 = 1.39 mbar.

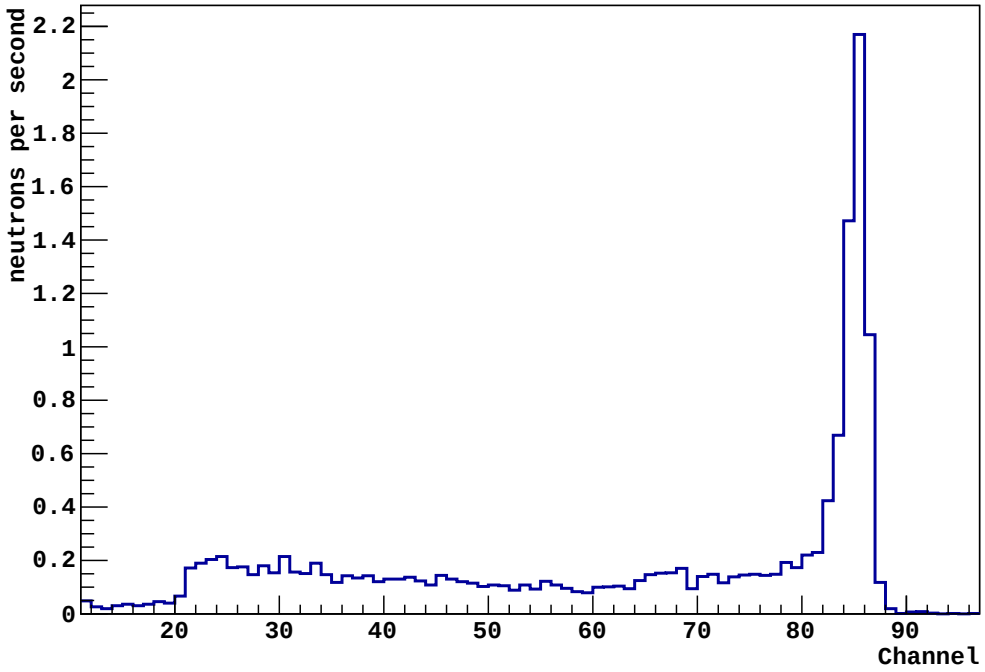

Figure 5.9: Spectrum of neutrons detected by the ^{3}He detector.

We scale the neutron flux going through the CCD as shown in Figure 5.10 according to ^{3}He measurements. The peaks and dips come from resonances in Cu(n, elastic), Fe(n, elastic) cross-sections. X-axis is the energy and y-axis is the flux of neutrons in units of neutrons per 10^9 decays of ^{124}Sb.

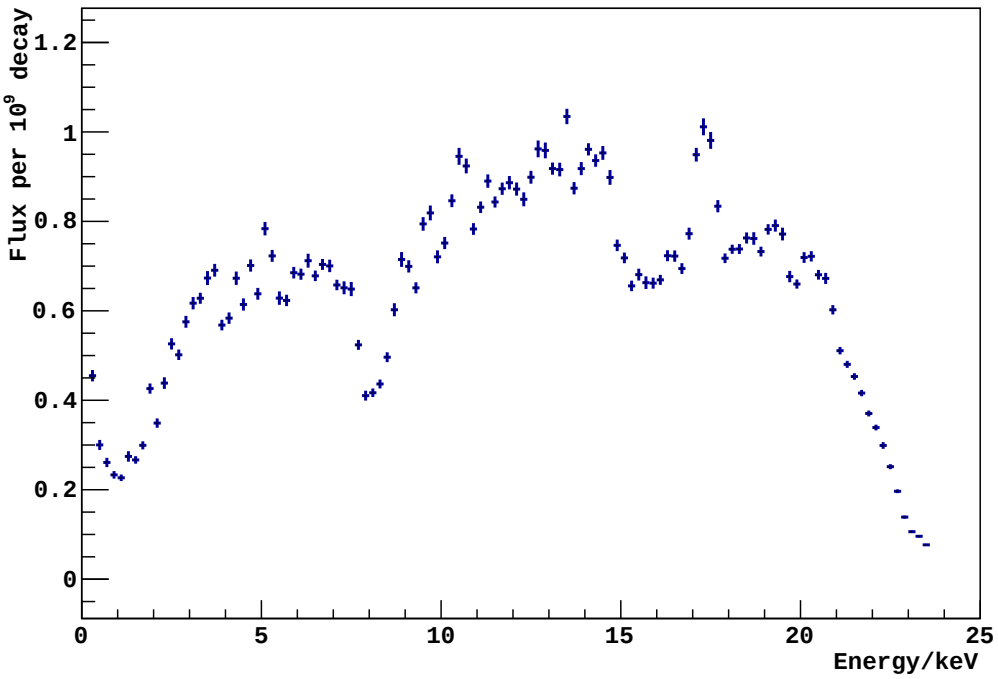

Figure 5.10: The neutron flux going through the CCD, where y-axis is the flux in units of neutrons per 10^9 decays of ^{124}Sb and x-axis the energy in units of keV.

5.4 Nuclear Recoil Spectrum

In the previous section, we obtain the flux spectrum of neutrons that go through the CCD in the simulations. A neutron with kinetic energy $E_{\rm n}$ interacts with a silicon nucleus elastically. Conservation of energy and momentum dictates the nuclear recoil energy to be

$$E_{\rm nr} = \frac{4E_{\rm in}}{(1+\frac{m_{\rm nr}}{m_{\rm in}})(1+\frac{m_{\rm in}}{m_{\rm nr}})} \times \cos^2(\theta), \tag{5.5}$$

where $E_{\rm nr}$ is the nuclear recoil energy of Si, $E_{\rm in}$ the incident neutron kinetic energy, and θ the incident angle in the lab frame. The neutron elastic scattering cross-section in natural silicon from Larson's measurement is shown in Fig 5.11 [42]. For energy from 0 to 24 keV,

the cross-section is around 2 mbarn. By applying the nuclear recoil spectrum and neutron elastic scattering cross-section to the flux spectrum of neutrons that go through the CCD, we obtain the nuclear recoil spectrum in the CCD, shown in Figure 5.12.

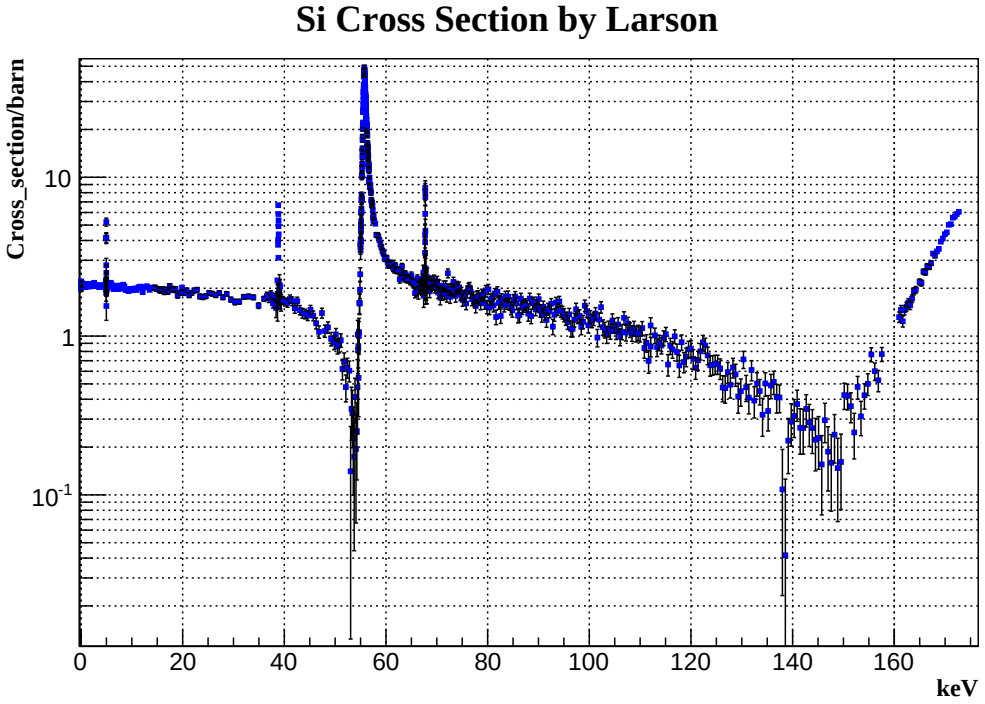

Figure 5.11: The neutron elastic scattering cross-section in natural silicon from Larson's measurement.

5.5 Ionization Efficiency

5.5.1 Data

We took data from January 2015 to June 2015. We have five sets of data with five different geometries of Sb and BeO, shown in Figure 5.13. Top left is Sb with all the BeO pieces ("Full BeO data set"); top center is Sb with an outer cylinder of BeO ("Outer BeO data set"); top right is Sb with an inner cylinder of BeO wrapped in polyethylene("Poly data set"); bottom left is Sb with an inner cylinder and a cap of BeO("Inner BeO data set"); and the bottom center is Sb with an outer cylinder of BeO and an inner cylinder Al_2O_3 ("Outer BeO Inner Al_2O_3 data set"). Noise and dark current of the setup during the period of data taking are shown in Figures 5.15 and 5.16, indicating that noise is roughly stable at $2e^-$ and

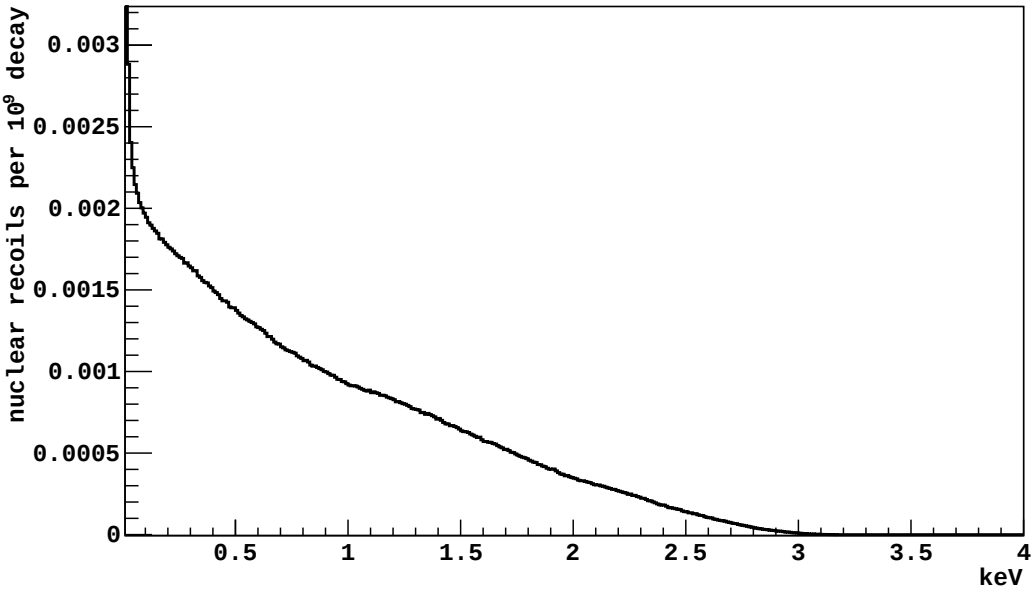

Figure 5.12: Nuclear recoil spectrum of silicon from simulations.

dark current is around $2e^-$. The vertical lines separate different source configurations. A ^{55}Fe source was used to calibrate the CCD, and the spectrum is shown in Figure 5.14. ^{55}Fe has a K-α X-ray line at 5.9 keV and a K-β line at 6.1 keV. Figure 5.17 shows the stability of the gain. The calibration lasted for 27 days, exhibiting 0.1% fluctuations in energy scale and 1% fluctuations in resolution.

We use the likelihood clustering method (discussed in Chapter 3) to search for low energy events in the images. Figure 5.18 shows the comparison between data taken with the BeO target and those with the Al target. The plot shows that there is no difference between the two spectra when the energy is over 1 keV_{ee} whereas some excess of events clearly exists in the sub-keV energy range. Figure 5.19 zooms in on the sub-keV range, where the red line shows data taken with a SbBe source while the black line shows data with SbAl (background).

The background data (taken with SbAl) are subtracted from SbBe data to obtain the real electron recoil spectrum. Through Compton scattering γ ray can generate a low energy background in the CCD, shown in Figure 5.20. The recoil spectrum is given by the Klein-Nishina formula when the target electron is free. However, for a bound electron in a silicon

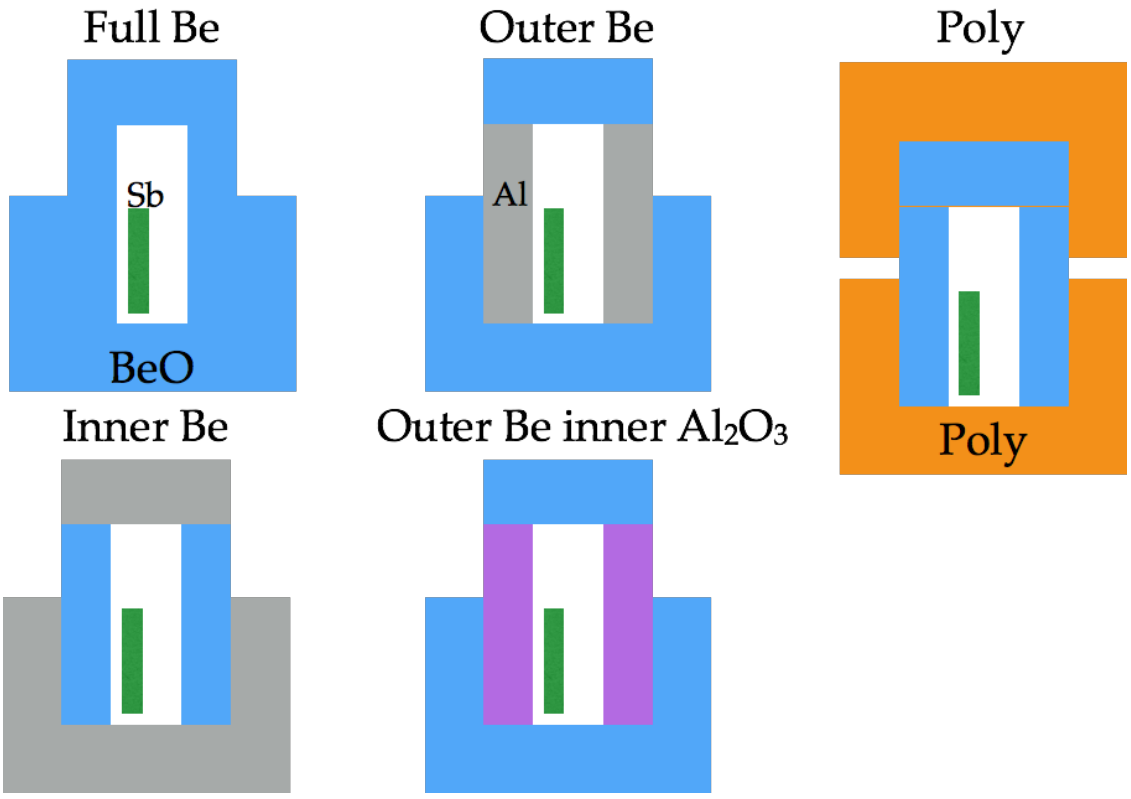

Figure 5.13: Different source geometries, including "Full BeO", "Outer BeO", "Inner BeO", "Outer BeO Inner Al_2O_3", and "Poly".

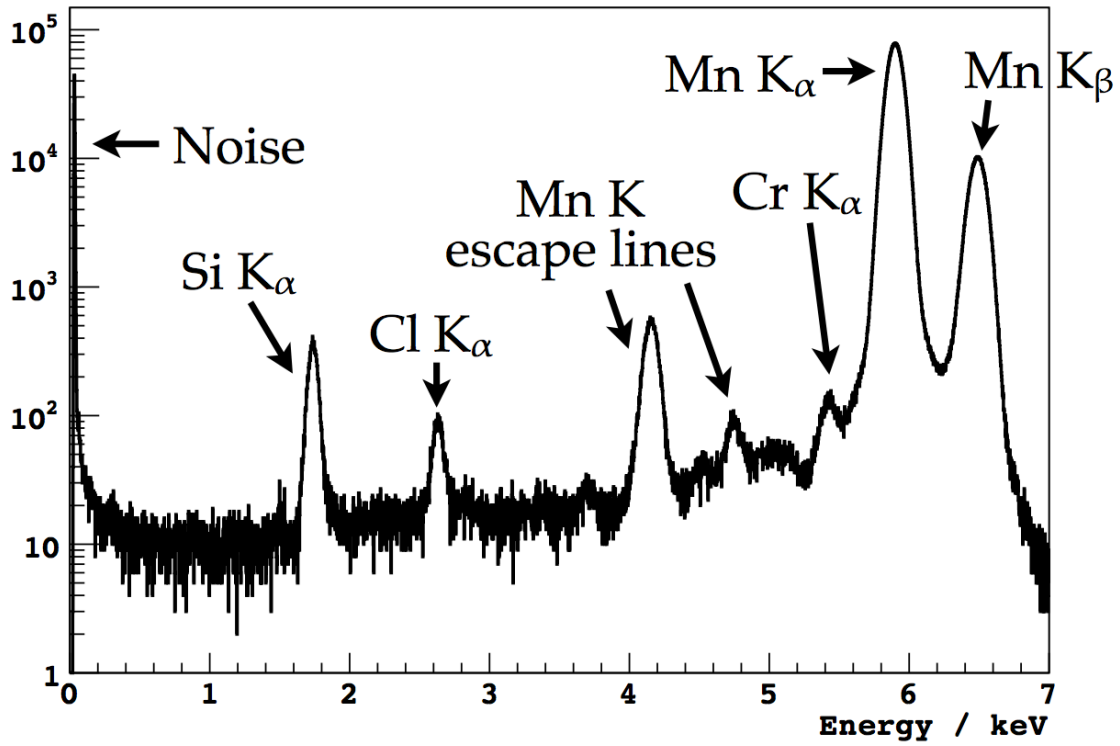

Figure 5.14: Data spectrum with the ^{55}Fe source. ^{55}Fe has a K-αX-ray line at 5.9 keV and a K-β line at 6.1 keV.

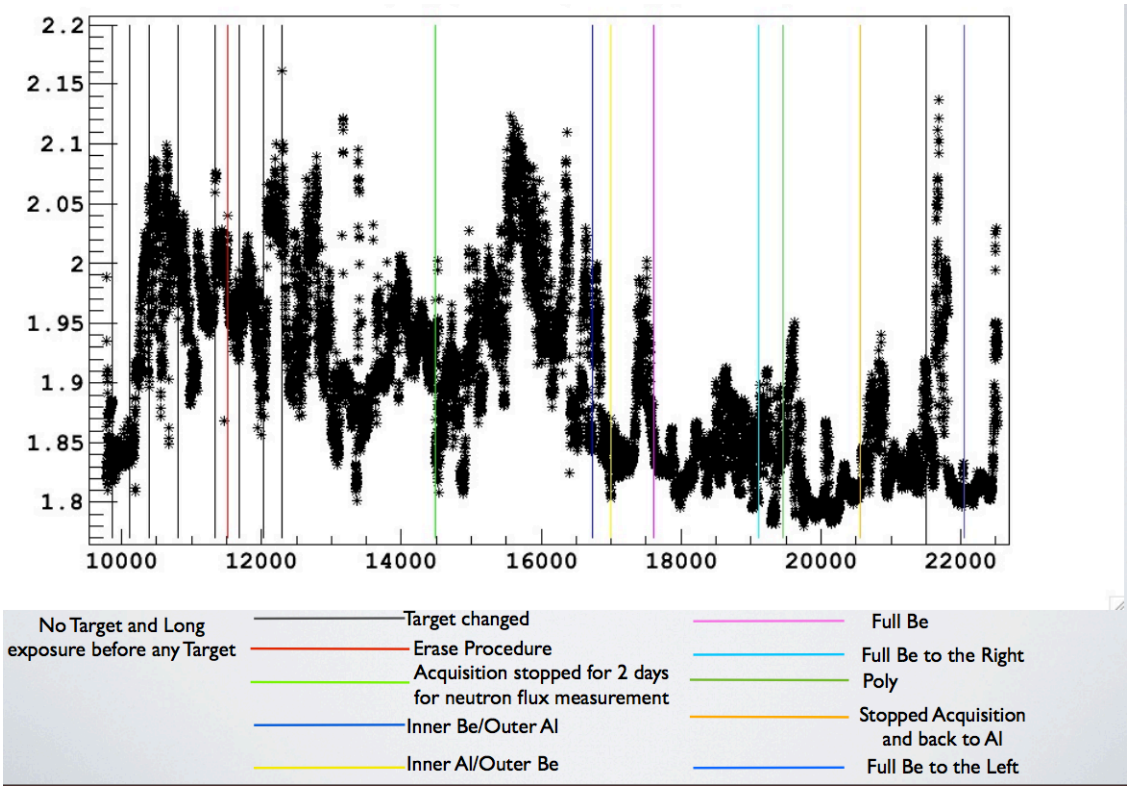

Figure 5.15: Readout noise of the setup during the period of data taking. Y-axis is the readout noise in e^- and x-axis the runid number. Different lines show different configurations of data taking. Readout noise was quite stable during the period of data taking.

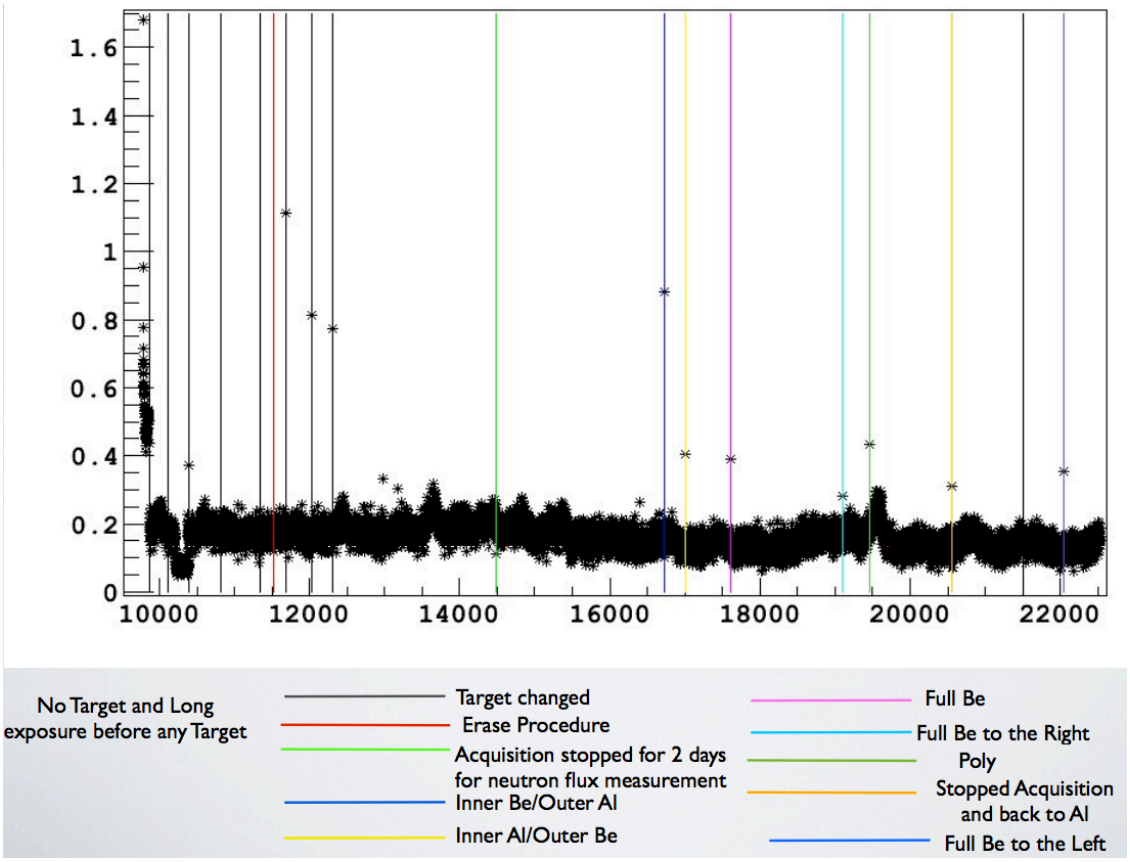

Figure 5.16: Dark current of the setup during the period of data taking. Y-axis is the readout noise in e^- and x-axis the runid number. Different lines show different configurations of data taking. Dark current was quite stable during the period of data taking.

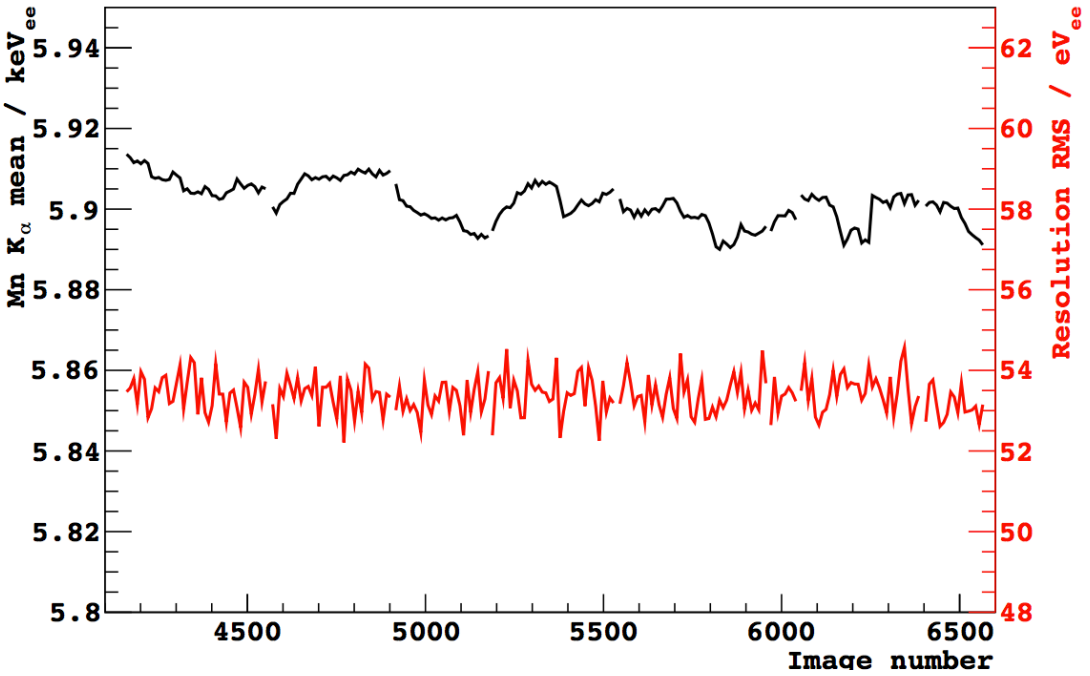

Figure 5.17: Stability of ^{55}Fe measurement over 27 days. The y-axis on the right is the peak position of the K-α line in keV and the y-axis on the left is the resolution of the K-α peak. The calibration lasted for 27 days, exhibiting 0.1% fluctuations in energy scale and 1% fluctuations in resolution.

atom, the Klein-Nishina formula is modified as

$$\frac{d^2\sigma}{d\omega' d\Omega'_{KN}} = \frac{r_0^2 m\omega'}{2|\vec{k}-\vec{k}'|\omega}\bar{X}_{\rm KN}J(p_z), \tag{5.6}$$

$$\bar{X}_{\rm KN} = \frac{\omega}{\omega'} + \frac{\omega'}{\omega} - \sin^2(\theta), \tag{5.7}$$

$$p_z = \frac{\omega\omega'(1-\cos(\theta) - m(\omega-\omega')]}{|\vec{k}-\vec{k}'|}, \tag{5.8}$$

where $J(p_z)$ for different electron shells can be obtained from tables in Bigg's 1975 [43]. With this theory, the recoil spectrum in the low energy range from a 500 keV γ ray is shown in Figure 5.21. The steps in the spectrum are due to different binding energies of electrons bound in different shells. Thus if we fit the SbAl data with the spectrum of an effective γ ray of 135 keV as the source, we can describe the shape in the low energy of the SbAl spectrum very well, as shown in Figure 5.22. The step at 2 keV and the drop at 10 keV are both well described by the theory.

The four sets of recoil spectra from neutrons (background subtracted) are shown in Figure

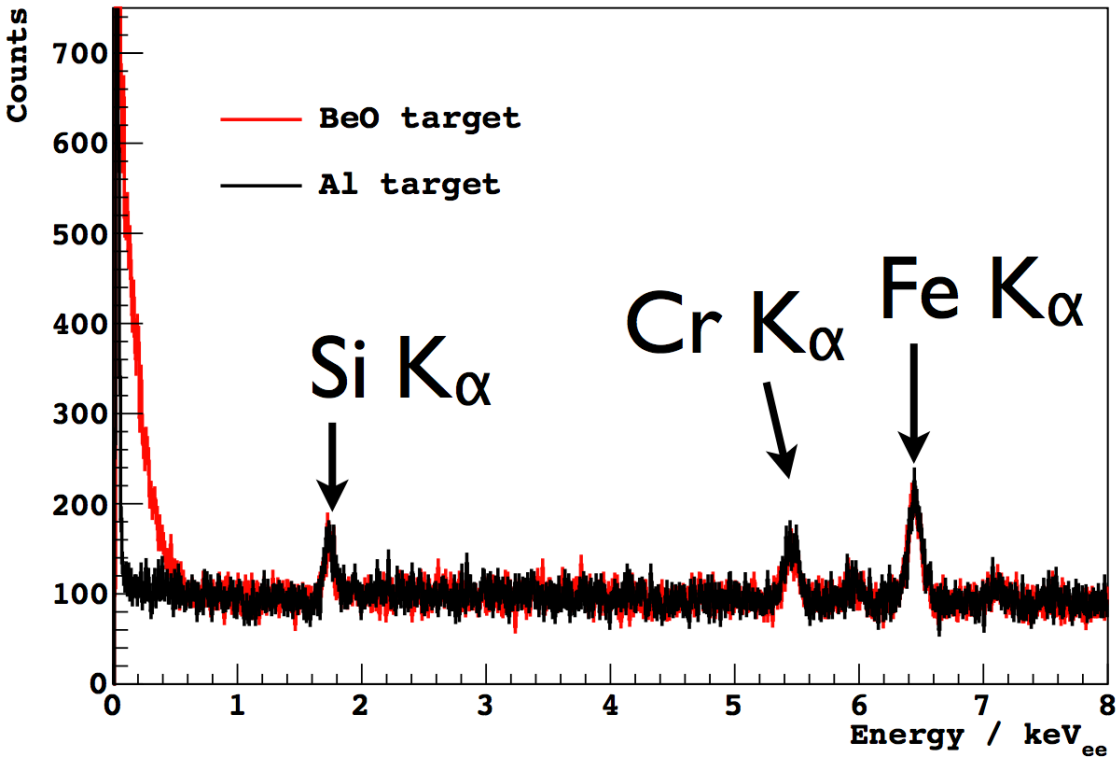

Figure 5.18: Comparison of data taken with a BeO target and with an Al target. The spectra show that there is no difference when the energy is greater than 1 keV$_{ee}$ whereas some excess clearly exists in the sub-keV energy range.

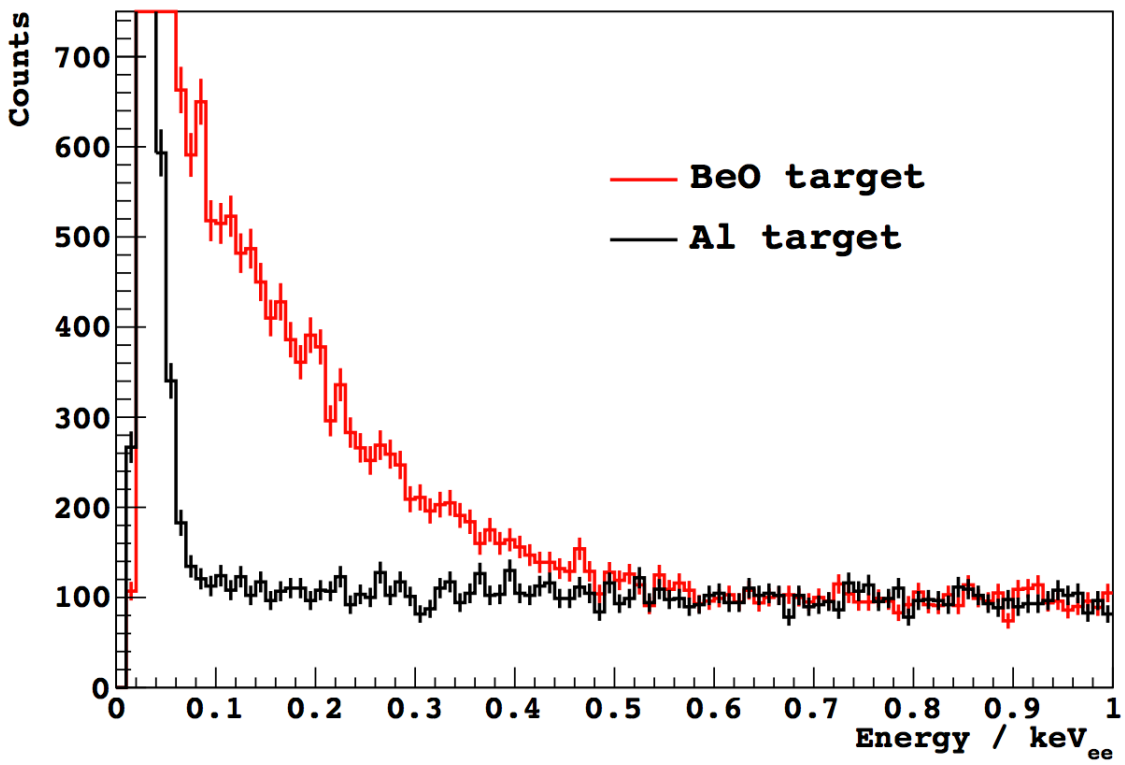

Figure 5.19: Comparison of data taken with a BeO target and with an Al target, zooming in on the sub-keV range.

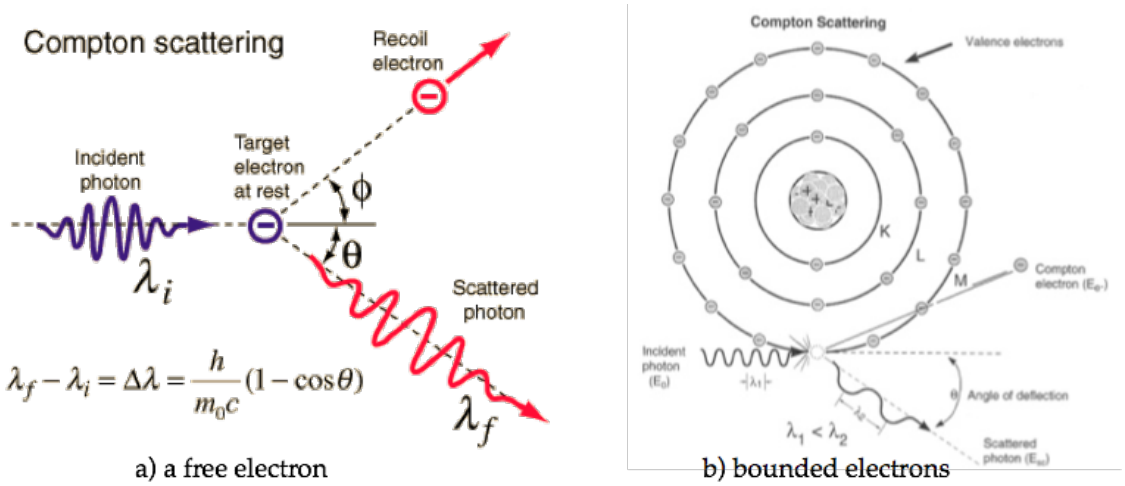

Figure 5.20: Compton Scattering in two situations: a) free electrons b) bound electrons.

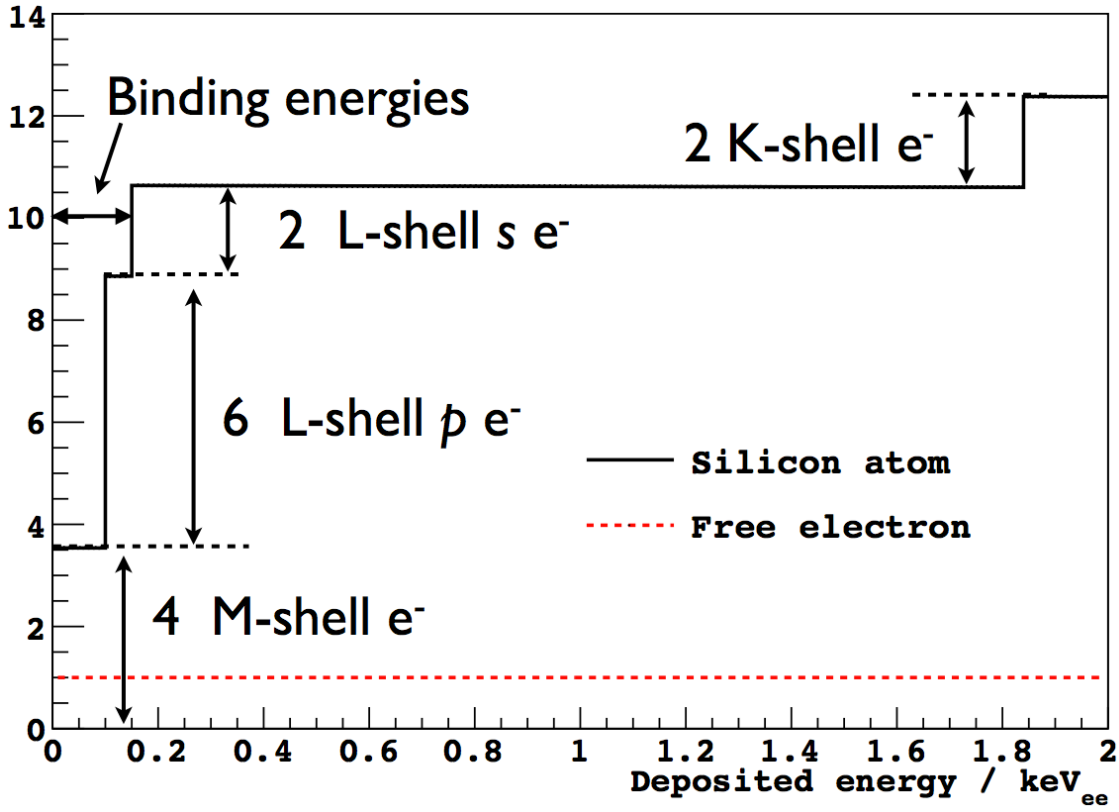

Figure 5.21: Recoil spectrum from a 500 keV γ ray in the low energy range with the modified Klein-Nishina formula.

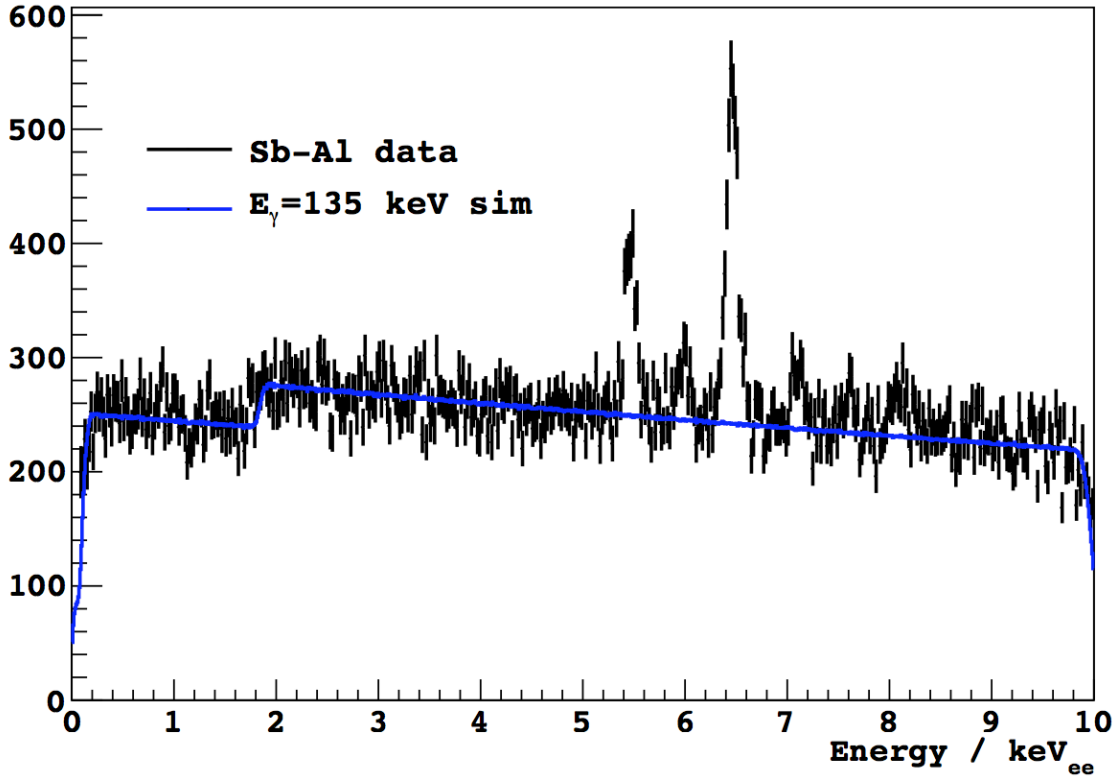

Figure 5.22: Fit result of the SbAl background data with Compton scattering from a γ ray with an effective energy of 135 keV.

5.23 . Y-axis is already scaled to counts per 10^9 decays of the ^{124}Sb source.

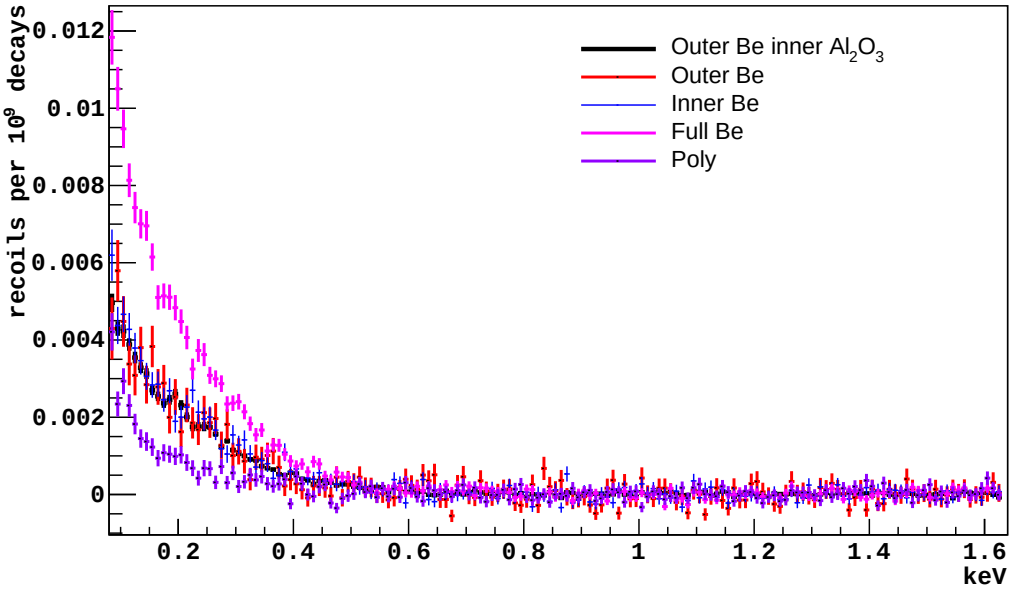

Figure 5.23: Electron recoil spectra from five source geometries.

5.5.2 Spectral Fit

We extract ionization efficiency by mapping from E_{ee} (Figure 5.12) to E_{nr} (Figure 5.23) with a few reasonable assumptions of ionization efficiency: a) no electron recoil energy will be recorded if there is no nuclear recoil energy, as f(0) = 0; b) more nuclear recoil energy produces more electron recoil energy, i.e. $f'(E_{\rm ee}) > 0$; c) ionization efficiency is always less than 1 due to conservation of energy.

We consider the resolution model applied to the simulated nuclear recoil spectrum in Figure 5.24 with the fano factor = 0.15.

Based on the four assumptions, we build a fitting function using the simulated nuclear recoil spectrum (Figure 5.12), a cubic spline function with five free parameters (Figure 5.25), and the resolution model, and then fit it to the electron recoil spectrum, minimizing χ^2 between the fitting function and the electron recoil spectrum. Spline functions are piecewise polynomials of degree n. The connections between polynomials are called knots and fulfill continuity conditions for the function and its first n-1 derivatives. Spline functions have found great use in mathematics and numerical analysis [44]. The spline function we use is

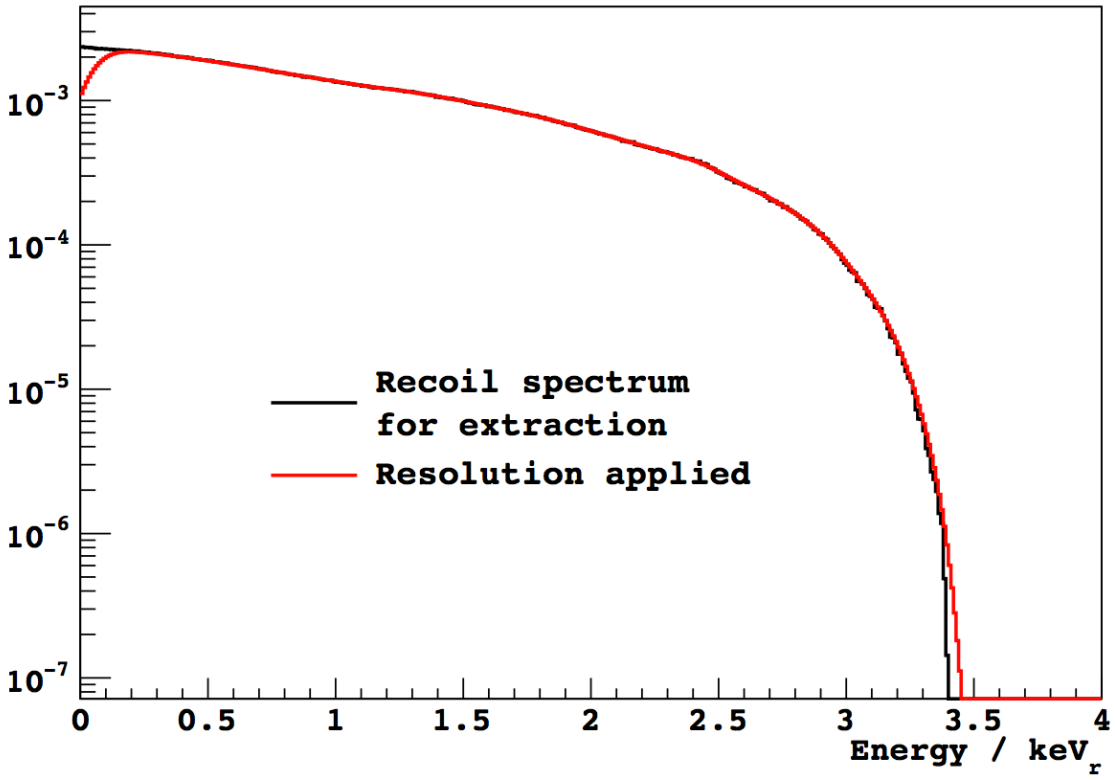

Figure 5.24: Nuclear spectrum after applying the resolution model.

defined by four knots and five free parameters one for each knot plus an extra one for the end knot as indicated by red arrows in Figure 5.25. We perform the fit on the Full BeO data set and present the result in Figures 5.26 and 5.27.

5.6 Results and Discussions

We extracted ionization efficiency from four data sets as shown in Figure 5.28. We weighted the extractions from different data sets based on its statistics. The uncertainties come from the following aspects: 1) photonuclear interaction cross-section of ^{9}Be from ^{3}He measurements used in the simulations, about 12-15%, 2) ^{124}Sb radioactive intensity measurements, about 5%, 3) statistical uncertainties from data spectra. The primary result shows our measurement is lower than the Lindhard Theory prediction with $k = 0.15$. Ioinzation efficiency of silicon has been measured by different groups in different energy ranges equal or greater than a few keV. This measurement here reaches the lowest energy range (less than 3 keV). The difference between this measurement and Lindhard theory is notable since the Linhard theory is used as a reference in the field. For a fixed nuclear recoil energy, the lower the

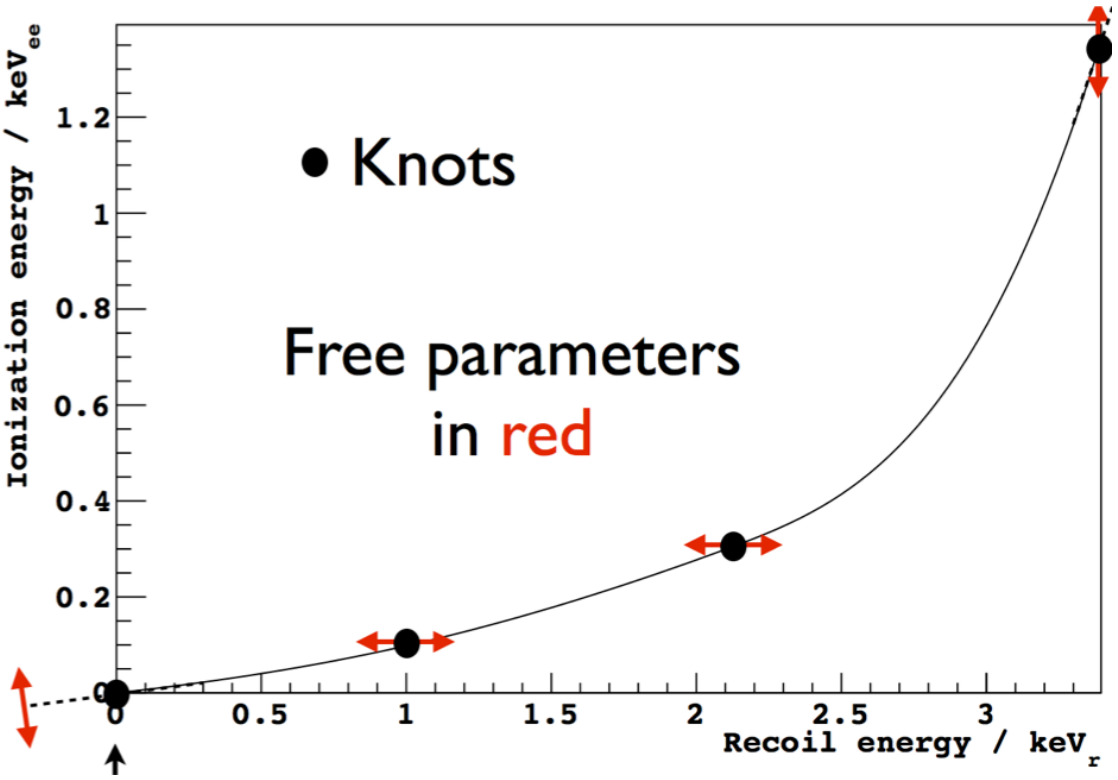

Figure 5.25: A cubic spline function that describes the mapping between the nuclear recoil spectrum and the electron recoil spectrum. It is defined by four knots and five free parameters one for each knot plus an extra one for the end knot as indicated by red arrows.

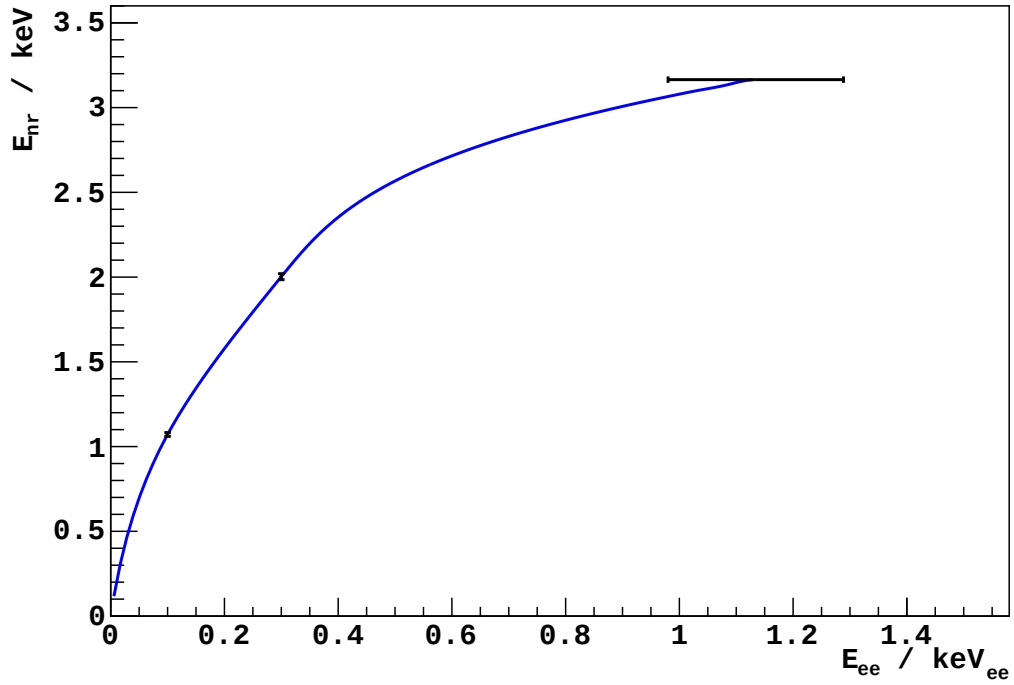

Figure 5.26: Ionization efficiency extracted from the Full BeO data set.

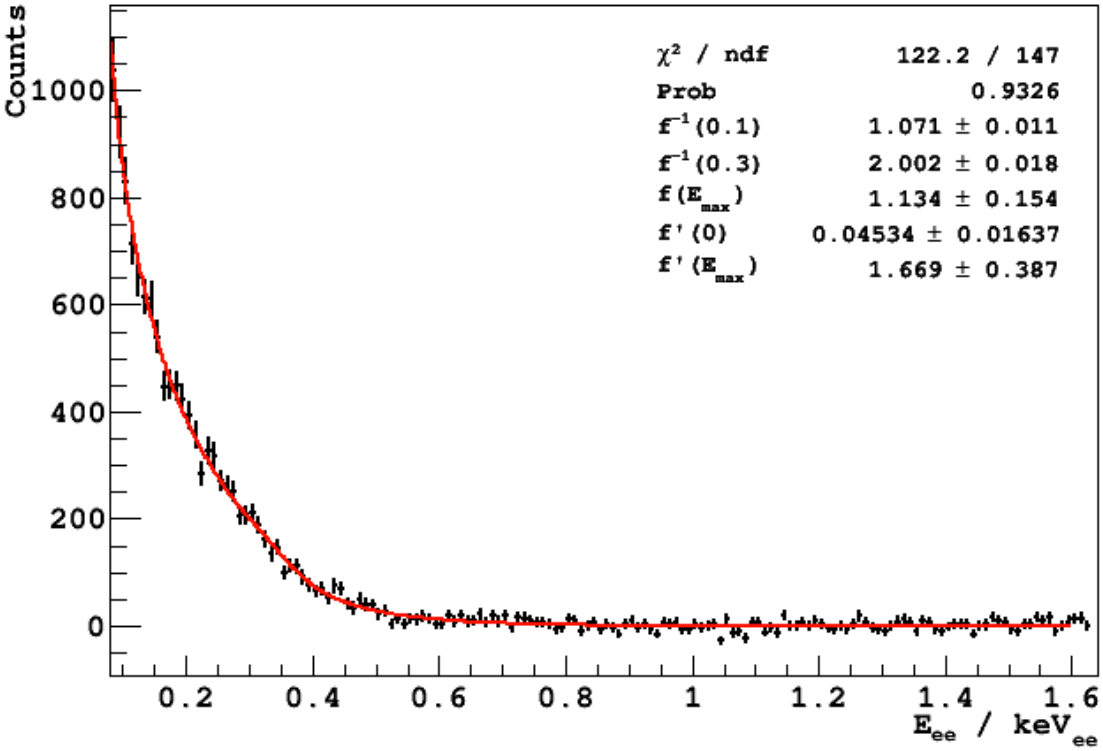

Figure 5.27: Fit to the electron recoil spectrum with the spline function fit into the data.

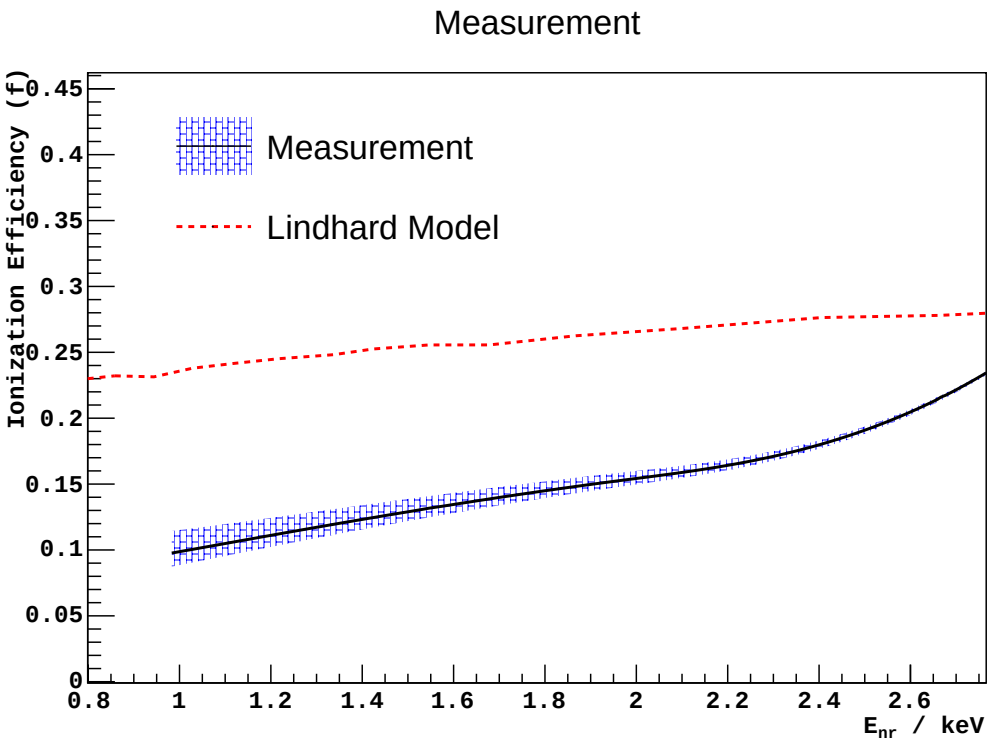

Figure 5.28: Ionization efficiency extracted from four data sets. We weighted the extractions from different data sets based on its statistics. The red dashed line is the Lindhard Theory prediction with $k = 0.15$.

ioinzation efficiency the lower ioinzation energy is, which shows the signifance of improving detection threshold. With our measurement, a 1 keV recoil could produce around 100 eV ioinzation energy which is still much larger than the current DAMIC detection threshold.

CHAPTER 6
CONCLUSION

The DAMIC R&D program, of which the work presented in this thesis has been an integral part, has successfully established the potential of large size, ≈mm-thick CCDs with very low readout noise as dark matter detectors. Several of these detectors are currently installed at SNOLAB, taking data with remarkable stability, low noise and low background.

We have developed a data analysis and simulation package which is widely used to characterize the CCDs and to estimate background levels.

We have presented novel analysis methods to measure radioactive contamination in the high-resistivity silicon CCDs of the DAMIC experiment. We exploited the unique signatures of α particles in CCDs to perform α spectroscopy and search for nuclides of the uranium and thorium chains. Also, we searched for ^{32}Si and ^{210}Pb in the bulk silicon of the CCD by identifying pairs of spatially correlated β tracks compatible with ^{32}Si–^{32}P and ^{210}Pb–^{210}Bi decay sequences. We placed stringent 95% CL upper limits on the presence of radioactive contaminants in the silicon bulk. The ^{238}U and ^{232}Th decay rates were found to be $<5\,\mathrm{kg^{-1}\,d^{-1}}$ and $<15\,\mathrm{kg^{-1}\,d^{-1}}$, respectively. Also, we established an upper limit of $\sim 35\,\mathrm{kg^{-1}\,d^{-1}}$ (95% CL) on the ^{210}Pb decay rate, obtained independently by α spectroscopy and the β decay sequence search. In addition, we have measured the decay rate of ^{32}Si in the silicon bulk to be 80^{+110}_{-65} kg^{-1} d^{-1} (95% CI). Since we detect single nuclear decays with high efficiency, our analysis methods have near-optimal sensitivity to radioactive contamination for a given exposure. In particular, the capability to identify ^{32}Si–^{32}P and ^{210}Pb–^{210}Bi decay sequences, unique among particle detectors, allows us to measure these contaminations at levels that are orders of magnitude lower than would be possible with any other screening technique. These levels of radioactive contamination are already low enough for the successful operation of DAMIC100, currently being installed in SNOLAB. In addition, material screening and handling procedures implemented for DAMIC100 should result in a tenfold reduction of the present background level, allowing for even more stringent limits on the radioactive contamination. Confirming the measurement, currently statistically limited, of ^{32}Si in high-resistivity silicon will be particularly relevant. In fact, the presence of the low energy β decay

of this cosmogenic isotope may impose additional constraints on the next generation WIMP searches with high-purity silicon detectors, including the use of an underground source of silicon to fabricate the detector and the requirement of ^{32}Si–^{32}P single-event identification for background suppression.

We also presented a measurement of the nuclear ionization efficiency in silicon, namely the ratio of the energy released in ionization by a recoiling nucleus to the nucleus kinetic energy. Since only a fraction of the kinetic energy is released in the form of ionization, the experimental determination of the nuclear ionization efficiency is required for any consistent interpretation of a search for dark matter particles. We have performed a measurement of the nuclear ionization efficiency by detecting nuclear recoils induced in a DAMIC CCD by a fairly monochromatic beam of neutrons from a ^{124}Sb-Be source. The measurement was performed in a variety of source configurations to control systematic uncertainties. It is the first measurement in the literature for kinetic energies of the recoiling silicon nucleus below 3 keV, in an energy range crucial for the search of recoils from low mass WIMPs. We find that the measured nuclear ionization efficiency is consistently lower than the prediction of the Lindhard theory in silicon, a notable results since the Lindhard theory is used as a reference in the field.

DAMIC is now at the end of its R&D phase and DAMIC100 is under construction. Soon it will have the chance of explaining the mystery of dark matter. Whatever the outcome, the path surely is one that will be filled with interesting questions, rewarding challenges, and unexpected discoveries that ultimately broaden our understanding of the universe.

REFERENCES

[1] C. Aalseth, P. Barbeau, J. Colaresi, J. Collar, J. D. Leon, J. Fast, N. Fields, T. Hossbach, A. Knecht, M. Kos, et al., *Cogent: A search for low-mass dark matter using p-type point contact germanium detectors*, *Physical Review D* **88** (2013), no. 1 012002.

[2] E. Aprile, M. Alfonsi, K. Arisaka, F. Arneodo, C. Balan, L. Baudis, B. Bauermeister, A. Behrens, P. Beltrame, K. Bokeloh, et al., *Dark matter results from 225 live days of xenon100 data*, *Physical review letters* **109** (2012), no. 18 181301.

[3] G. Angloher, M. Bauer, I. Bavykina, A. Bento, C. Bucci, C. Ciemniak, G. Deuter, F. von Feilitzsch, D. Hauff, P. Huff, et al., *Results from 730 kg days of the cresst-ii dark matter search*, *The European Physical Journal C* **72** (2012), no. 4 1–22.

[4] W. Zhao, Q. Yue, K.-J. Kang, J. Cheng, Y. Li, S. Lin, Y. Bai, Y. Bi, J. Chang, N. Chen, et al., *First results on low-mass wimps from the cdex-1 experiment at the china jinping underground laboratory*, *Physical Review D* **88** (2013), no. 5 052004.

[5] P. Collaboration, P. A. R. Ade, N. Aghanim, M. I. R. Alves, C. Armitage-Caplan, M. Arnaud, M. Ashdown, F. Atrio-Barandela, J. Aumont, H. Aussel, C. Baccigalupi, A. J. Banday, R. B. Barreiro, R. Barrena, M. Bartelmann, J. G. Bartlett, N. Bartolo, S. Basak, E. Battaner, R. Battye, K. Benabed, A. Benoît, A. Benoit-Lévy, J.-P. Bernard, M. Bersanelli, B. Bertincourt, M. Bethermin, P. Bielewicz, I. Bikmaev, A. Blanchard, J. Bobin, J. J. Bock, H. Böhringer, A. Bonaldi, L. Bonavera, J. R. Bond, J. Borrill, F. R. Bouchet, F. Boulanger, H. Bourdin, J. W. Bowyer, M. Bridges, M. L. Brown, M. Bucher, R. Burenin, C. Burigana, R. C. Butler, E. Calabrese, B. Cappellini, J.-F. Cardoso, R. Carr, P. Carvalho, M. Casale, G. Castex, A. Catalano, A. Challinor, A. Chamballu, R.-R. Chary, X. Chen, and et al. (342 additional authors not shown) `arXiv:1303.5062`.

[6] E. Corbelli and P. Salucci, *The extended rotation curve and the dark matter halo of m33*, *Monthly Notices of the Royal Astronomical Society* **311** (2000), no. 2 441–447.

[7] A. A. Penzias and R. W. Wilson, *A measurement of excess antenna temperature at 4080 mc/s.*, *The Astrophysical Journal* **142** (1965) 419–421.

[8] S. Faber and R. E. Jackson, *Velocity dispersions and mass-to-light ratios for elliptical galaxies*, *The Astrophysical Journal* **204** (1976) 668–683.

[9] M. Kamionkowski `hep-ph/9710467`.

[10] J. E. Kim" *Physical Review Letters* **43** (1979), no. 2 103–107.

[11] J. Lewin and P. Smith, *Review of mathematics, numerical factors, and corrections for dark matter experiments based on elastic nuclear recoil*, *Astroparticle Physics* **6** (1996), no. 1 87–112.

[12] R. Bernabei, P. Belli, F. Cappella, R. Cerulli, C. Dai, A. d'Angelo, H. He, A. Incicchitti, H. Kuang, J. Ma, et al., *First results from dama/libra and the combined results with dama/nai*, *The European Physical Journal C* **56** (2008), no. 3 333–355.

[13] M. Boulay, D. Collaboration, et al., *Deap-3600 dark matter search at snolab*, in *Journal of Physics: Conference Series*, vol. 375, p. 012027, IOP Publishing, 2012.

[14] Z. Ahmed, D. Akerib, S. Arrenberg, C. Bailey, D. Balakishiyeva, L. Baudis, D. Bauer, P. Brink, T. Bruch, R. Bunker, et al., *Dark matter search results from the cdms ii experiment.*, *Science (New York, NY)* **327** (2010), no. 5973 1619–1621.

[15] P. Agnes, T. Alexander, A. Alton, K. Arisaka, H. Back, B. Baldin, K. Biery, G. Bonfini, M. Bossa, A. Brigatti, et al., *First results from the darkside-50 dark matter experiment at laboratori nazionali del gran sasso*, *Physics Letters B* **743** (2015) 456–466.

[16] E. Aprile, K. Arisaka, F. Arneodo, A. Askin, L. Baudis, A. Behrens, E. Brown, J. Cardoso, B. Choi, D. Cline, et al., *The xenon100 dark matter experiment*, *Astroparticle Physics* **35** (2012), no. 9 573–590.

[17] E. Ramberg, C. Collaboration, et al., *Developing a 60kg bubble chamber for dark matter detection*, *Nuclear Instruments and Methods in Physics Research Section A: Accelerators, Spectrometers, Detectors and Associated Equipment* **623** (2010), no. 1 454–456.

[18] J. R. Janesick, *Scientific charge-coupled devices*, vol. 117. SPIE press Bellingham, 2001.

[19] F. Livet, F. Bley, J. Mainville, R. Caudron, S. Mochrie, E. Geissler, G. Dolino, D. Abernathy, G. Grübel, and M. Sutton, *Using direct illumination ccds as high-resolution area detectors for x-ray scattering*, *Nuclear Instruments and Methods in Physics Research Section A: Accelerators, Spectrometers, Detectors and Associated Equipment* **451** (2000), no. 3 596–609.

[20] C. Bebek, R. Coles, P. Denes, F. Dion, J. Emes, R. Frost, D. Groom, R. Groulx, S. Haque, S. Holland, et al., *Ccd research and development at lawrence berkeley national laboratory*, in *SPIE Astronomical Telescopes+ Instrumentation*, pp. 845305–845305, International Society for Optics and Photonics, 2012.

[21] D. E. S. Collaboration `astro-ph/0510346`.

[22] R. Agnese, A. Anderson, M. Asai, D. Balakishiyeva, R. B. Thakur, D. Bauer, J. Billard, A. Borgland, M. Bowles, D. Brandt, P. Brink, R. Bunker, B. Cabrera, D. Caldwell, D. Cerdeno, H. Chagani, J. Cooley, B. Cornell, C. Crewdson,

P. Cushman, M. Daal, P. D. Stefano, T. Doughty, L. Esteban, S. Fallows, E. Figueroa-Feliciano, G. Godfrey, S. Golwala, J. Hall, H. Harris, S. Hertel, T. Hofer, D. Holmgren, L. Hsu, M. Huber, A. Jastram, O. Kamaev, B. Kara, M. Kelsey, A. Kennedy, M. Kiveni, K. Koch, B. Loer, E. L. Asamar, R. Mahapatra, V. Mandic, C. Martinez, K. McCarthy, N. Mirabolfathi, R. Moffatt, D. Moore, P. Nadeau, R. Nelson, K. Page, R. Partridge, M. Pepin, A. Phipps, K. Prasad, M. Pyle, H. Qiu, W. Rau, P. Redl, A. Reisetter, Y. Ricci, T. Saab, B. Sadoulet, and et al. (14 additional authors not shown) `arXiv:1309.3259`.

[23] N. C. Buchholz and P. N. Daly, *The monsoon generic pixel server software design*, in *Astronomical Telescopes and Instrumentation*, pp. 364–372, International Society for Optics and Photonics, 2004.

[24] S. E. Holland, W. F. Kolbe, and C. J. Bebek, *Device design for a 12.3-megapixel, fully depleted, back-illuminated, high-voltage compatible charge-coupled device*, *Electron Devices, IEEE Transactions on* **56** (2009), no. 11 2612–2622.

[25] J. Ponz, R. Thompson, and J. Munoz, *The fits image extension*, *Astronomy and Astrophysics Supplement Series* **105** (1994) 53–55.

[26] X. MCNP, *Monte carlo team, mcnp–a general purpose monte carlo n-particle transport code, version 5*, tech. rep., LA-UR-03-1987, Los Alamos National Laboratory, April 2003. The MCNP5 code can be obtained from the Radiation Safety Information Computational Center (RSICC), PO Box 2008, Oak Ridge, TN, 37831-6362, 5.

[27] V. McLane, *Endf-102 data formats and procedures for the evaluated nuclear data file endf-6*, tech. rep., Brookhaven National Lab., Upton, NY (United States). Funding organisation: DOE/SC (United States), 2001.

[28] A. Karcher, C. J. Bebek, W. F. Kolbe, D. Maurath, V. Prasad, M. Uslenghi, and M. Wagner, *Measurement of lateral charge diffusion in thick, fully depleted, back-illuminated ccds*, in *Nuclear Science Symposium Conference Record, 2003 IEEE*, vol. 3, pp. 1513–1517, IEEE, 2003.

[29] A. Chavarria, J. Tiffenberg, A. Aguilar-Arevalo, D. Amidei, X. Bertou, G. Cancelo, J. C. D'Olivo, J. Estrada, G. F. Moroni, F. Izraelevitch, B. Kilminster, Y. Langisetty, J. Liao, J. Molina, P. Privitera, C. Salazar, Y. Sarkis, V. Scarpine, T. Schwarz, M. S. Haro, F. Trillaud, and J. Zhou `arXiv:1407.0347`.

[30] A. E. Chavarria, *Study on pep and CNO solar neutrino interaction rates in Borexino.* PhD thesis, Princeton University, 2012.

[31] V. Hoffmann, M. Kasik, P. K. Robinson, and C. Venzago, *Glow discharge mass spectrometry*, *Analytical and bioanalytical chemistry* **381** (2005), no. 1 173–188.

[32] B. Mohanty, P. Balouria, M. Garg, T. Nandi, V. Mittal, and I. Govil, *Comparison of experimental and theoretical efficiency of hpge x-ray detector*, *Nuclear Instruments and Methods in Physics Research Section A: Accelerators, Spectrometers, Detectors and Associated Equipment* **584** (2008), no. 1 186–190.

[33] W. von Ammon and H. Herzer, *The production and availability of high resistivity silicon for detector application*, *Nucl. Instrum. Meth. Phys. Res.* **A 226** (1984), no. 1 94–102.

[34] S. Holland, D. Groom, N. Palaio, R. Stover, and M. Wei, *Fully depleted, back-illuminated charge-coupled devices fabricated on high-resistivity silicon*, *IEEE Trans. Electron Devices* **50** (2003), no. 1 225–238.

[35] J. Estrada, J. Molina, J. J. Blostein, and G. Fernandez, *Plasma effect in silicon charge coupled devices (CCDs)*, *Nucl. Instrum. Meth. Phys. Res.* **A 665** (2011) 90–93, [arXiv:1105.3229].

[36] D. Groom, *Cosmic rays and other nonsense in astronomical CCD imagers*, *Exp. Astron.* **14** (2002), no. 1 45–55.

[37] D. O. Caldwell et al., *Searching for the cosmion by scattering in Si detectors*, *Phys. Rev. Lett.* **65** (1990) 1305–1308.

[38] X-5 MONTE CARLO TEAM, *MCNP – A General Monte Carlo N-Particle Transport Code, Version 5*, Tech. Rep. LA-UR-03-1987, Los Alamos National Laboratory, Feb., 2008.

[39] G. J. Feldman and R. D. Cousins, *A Unified approach to the classical statistical analysis of small signals*, *Phys. Rev.* **D57** (1998) 3873–3889, [physics/9711021].

[40] G. Iafrate and J. Ziegler, *Numerical evaluation of lindhard's theory of stopping power for a charged particle in a free-electron gas*, *Journal of Applied Physics* **50** (1979), no. 9 5579–5581.

[41] P. Sorensen, *Atomic limits in the search for galactic dark matter*, *Physical Review D* **91** (2015), no. 8 083509.

[42] D. Larson, C. Johnson, J. Harvey, and N. Hill, *Measurement of the neutron total cross section of silicon from 5 ev to 730 kev*, tech. rep., Oak Ridge National Lab., Tenn.(USA), 1976.

[43] F. Biggs, L. Mendelsohn, and J. Mann, *Hartree-fock compton profiles for the elements*, *Atomic data and nuclear data tables* **16** (1975), no. 3 201–309.

[44] S. Wold, *Spline functions in data analysis*, *Technometrics* **16** (1974), no. 1 1–11.